



University of Liège  
Department of mechanical and aerospace engineering  
Academic year 2015-2016

---

# Improvement of the aerodynamic behaviour of a blended wing body unmanned aerial vehicle: numerical and experimental investigations

---

Submitted by Martin MASEREEL to the Department of aerospace and mechanical engineering of the University of Liège in partial fulfilment of the requirements for the degree of master in aerospace engineering

**Thesis supervisors**  
**Members of the jury**

T. Andrianne and Prof. V. Terrapon  
Didier Breyne  
Prof. L. Noels  
Pierre-André Vigano

## **Abstract**

This master thesis will present the aerodynamic analysis of a blended wing unmanned aerial vehicle developed by the company Aircraft Traders Belgium s.a. Different methods of analysis will first be validated and then used to determine the performances of the baseline geometry. Then, a parametric model of the aircraft will be used to perform a sensitivity analysis to improve the baseline design. This will be done by varying the taper ratio and the sweep angle of the wing as well as the taper ratio, sweep angle and height of the winglet. According to the sensitivity analysis, a new geometry will be proposed and compared to the baseline design. Finally, a Reynolds sensitivity analysis will be performed in order to determine if a reduced size model could be studied in the wind tunnel of the University of Liège.

# Contents

<b>I</b>	<b>Introduction</b>	<b>1</b>
1	Background and context	2
2	Objectives	5
3	State-of-the-art	6
3.1	Definition of a blended wing body . . . . .	6
3.2	Definition of an unmanned aerial vehicle . . . . .	7
3.3	History of blended wing bodies . . . . .	7
3.4	Existing research on BWB . . . . .	9
<b>II</b>	<b>Aerodynamic tools</b>	<b>12</b>
4	Experimental results	14
5	Low fidelity aerodynamic tool	16
5.1	Choice of software . . . . .	16
5.2	PanAir implementation . . . . .	16
5.3	Convergence analysis of the mesh . . . . .	20
5.4	Validation of PanAir . . . . .	22
6	High fidelity aerodynamic tool	29
6.1	Introduction on SU <sup>2</sup> . . . . .	29
6.2	Meshing using ANSYS ICEM . . . . .	31
6.3	Convergence analysis on the size of cells and domain . . . . .	34
6.4	Validation of SU <sup>2</sup> . . . . .	35
6.5	Summary . . . . .	37
7	Aerodynamic properties of the baseline geometry	39
7.1	Geometry discretization for the baseline Guardian Eye model . . . . .	39
7.2	Lift coefficient versus angle of attack . . . . .	40
7.3	Drag coefficient versus angle of attack . . . . .	41
7.4	Pitching moment versus angle of attack . . . . .	42
7.5	Lift to drag ratio versus angle of attack . . . . .	43
7.6	Influence of sideslip . . . . .	44
7.7	Influence of the control surfaces . . . . .	46
7.8	Influence of the propulsion . . . . .	46

<b>III</b>	<b>Aerodynamic study</b>	<b>50</b>
<b>8</b>	<b>Choice of parameters</b>	<b>52</b>
<b>9</b>	<b>Parametric study</b>	<b>54</b>
9.1	Taper ratio of the wing $\lambda_w$ . . . . .	54
9.2	Sweep angle of the wing $\Lambda_w$ . . . . .	55
9.3	Height of the winglet $h_{wt}$ . . . . .	56
9.4	Taper ratio of the winglet $\lambda_{wt}$ . . . . .	57
9.5	Sweep angle of the winglet $\Lambda_{wt}$ . . . . .	58
9.6	Summary of the parametric study . . . . .	58
<b>10</b>	<b>GE<sup>+</sup> geometry</b>	<b>62</b>
<b>11</b>	<b>Detailed analysis of the GE<sup>+</sup></b>	<b>64</b>
11.1	Lift coefficient versus angle of attack . . . . .	64
11.2	Drag coefficient versus angle of attack . . . . .	64
11.3	Pitching moment versus angle of attack . . . . .	64
11.4	Lift to drag ratio versus angle of attack . . . . .	65
11.5	Influence of sideslip . . . . .	66
11.6	Influence of control surfaces . . . . .	66
11.7	Influence of the propulsion . . . . .	67
11.8	Summary . . . . .	67
<b>12</b>	<b>Reynolds effect on GE<sup>+</sup></b>	<b>70</b>
<b>Appendices</b>		



# List of Figures

1.1	Picture of the GE1 in flight . . . . .	3
1.2	Schematic representation of the main geometry parameters of the baseline design, GE1 . . . . .	4
3.1	Comparison of different aircraft configurations . . . . .	6
3.2	Multiple pictures of early or recent attempts to flying wing and blended wing body designs . . . . .	8
3.3	Comparison of performances between the A380-700 and the resulting design of the BWB-450 . . . . .	10
5.1	Evolution of the induced drag coefficient $C_{D_i}$ in function of the number of spanwise panels with a number of chordwise panels set to 60 for a NACA 0018 of aspect ratio equal to 6 at an AOA of $6^\circ$ . . . . .	21
5.2	Evolution of the induced drag coefficient $C_{D_i}$ in function of the number of chordwise panels with the number of spanwise panels set to 32 for a NACA 0018 of aspect ratio equal to 6 at an AOA of $6^\circ$ . . . . .	22
5.3	Pressure distribution along a section of the wing at $y = 1.59$ when the number of chordwise panels is equal to 140 for a NACA 0018 of aspect ratio equal to 6 at an AOA of $6^\circ$ . The pressure coefficient $C_p$ is plotted in function of the chordwise coordinates $x/c$ . . . . .	23
5.4	Geometry discretization for a NACA 0018 wing of aspect ratio 6 . . . . .	23
5.5	Lift coefficient $C_L$ in function of the angle of attack $\alpha$ for different theories: the Prandtl lifting line theory, the PanAir program, the two dimensional thin airfoil theory and the eperimental results of the NACA report by Goett [12] for a NACA0018 wing of aspect ratio 6 . . . . .	24
5.6	Drag coefficient $C_D$ in function of the angle of attack $\alpha$ for different theories: the Prandtl lifting line theory, the PanAir program and the experimental results of the NACA report for a NACA0012 wing of aspect ratio 6 [12] . . . . .	25
5.7	Schematic represenation of the different components of the drag (illustration from Gur [13]) . . . . .	25
5.8	Drag coefficient $C_D$ in function of the angle of attack after correction of the drag to take friction and form drag into account. Errorbars represent the error with the experimental results . . . . .	27
5.9	Schematic representation of a split flap and a plain flap with deflection $\delta_f$ as investigated in the report on NACA airfoils, Ames [3] . . . . .	27

5.10	Evolution of the lift coefficient $C_L$ in function of the angle of attack $\alpha$ for a NACA23015 at zero angle of attack and $Re = 609000$ . Comparison of the results coming from PanAir and the experimental results by Ames [3] for different angles of flap deflection $\delta_f$ . . . . .	28
6.1	Hybrid mesh around the GE1 . . . . .	32
6.2	Schematic representation of the computational domain of a half GE1 where the dotted edges belong to faces on which a far field condition is imposed and the face whose edges are plain lines is a face on which a symmetry condition is imposed. The UAV is represented by the gray body. The side of the cube is equal to $n$ time the largest chord $c$ of the body . . . . .	33
6.3	Drag coefficient $C_D$ in function of the number cells in the computational domain. The dashed line represents the exact value of drag obtained by experimentation in Goett [12] . . . . .	34
6.4	Drag coefficient $C_D$ in function of the computational cube's size, here varying from five to 140 times the chord at half span, the multiplication factor is noted $n$ . The dashed line represents the exact value of drag obtained by experimentation in Goett [12] . . . . .	35
6.5	Lift coefficient $C_L$ in function of the angle of attack $\alpha$ for a NACA 0018 wing of aspect ratio equal to six . . . . .	36
6.6	Drag coefficient $C_D$ in function of the angle of attack $\alpha$ for a NACA 0018 wing of aspect ratio equal to six . . . . .	37
6.7	Illustration of stairstepping of the prism layer at the trailing edge . .	37
6.8	Evolution of the lift coefficient $C_L$ in function of the angle of attack $\alpha$ for a NACA23015 at zero angle of attack and $Re = 609000$ . Comparison of the results coming from SU <sup>2</sup> and the experimental results by Ames [3] for different angles of flap deflection $\delta_f$ . . . . .	38
7.1	Induced drag $C_{D_i}$ in function of the number of spanwise panels for the baseline GE1 configuration at a freestream velocity of 18 m/s and an angle of attack of 2° . . . . .	40
7.2	Schematical representation of the chosen discretization for the GE1 .	41
7.3	Lift coefficient $C_L$ in function of the angle of attack $\alpha$ for the GE1 BWB UAV for different analysis methods . . . . .	42
7.4	Drag coefficient $C_L$ in function of the angle of attack $\alpha$ for the GE1 BWB UAV for different analysis methods . . . . .	43
7.5	Pitching moment coefficient $C_m$ in function of the angle of attack $\alpha$ for the GE1 BWB UAV for different analysis methods . . . . .	44
7.6	Lift to drag ratio $L/D$ in function of the angle of attack $\alpha$ for the GE1 BWB UAV for different analysis methods . . . . .	45
7.7	Lift coefficient $C_L$ in function of the sideslip angle $\beta$ for the GE1 when $U_\infty = 18$ m/s and the $AOA = 2^\circ$ . . . . .	46
7.8	Schematic representation of the shape and size of the control surface on the GE1 . . . . .	47
7.9	Evolution of the lift coefficient $C_L$ in function of the angle of attack $\alpha$ for the GE1 for different angles of flap deflection $\delta_f$ . . . . .	48
7.10	Lift coefficient $C_L$ in function of the angle of attack $\alpha$ for both engine modes (zero and full thrust) for the GE1 . . . . .	49

7.11	Drag coefficient $C_D$ in function of the angle of attack $\alpha$ for both engine modes (zero and full thrust) for the GE1 . . . . .	49
8.1	Ratio of the lift coefficient over the lift-induced drag $C_L/C_{D_i}$ in function of the length of the fuselage $l$ . . . . .	53
9.1	Lift to drag ratio $L/D$ in function of the wing's taper ratio $\lambda_w$ (every other parameter is set to default) . . . . .	55
9.2	Lift coefficient $C_L$ in function of the wing's taper ratio $\lambda_w$ (every other parameter is set to default). The black dotted line represents the minimum lift required to maintain flight . . . . .	56
9.3	Convention for the measure of sweep angle of the wing $\Lambda_w$ . . . . .	57
9.4	Lift to drag ratio $L/D$ in function of the sweep angle of the wing $\Lambda_w$ (every other parameter is set to default) . . . . .	58
9.5	Friction drag $C_{D_f}$ and induced drag $C_{D_i}$ in function of the winglet height $h_{wt}$ (every other parameter is set to default) . . . . .	59
9.6	Lift to drag ratio $L/D$ in function of the winglet's taper ratio $h_{wt}$ (every other parameter is set to default) . . . . .	60
9.7	Convention for the measure of the winglet's sweep angle $\Lambda_{wt}$ . . . . .	61
9.8	Lift to drag ratio $L/D$ in function of the winglet's sweep angle $\Lambda_{wt}$ (every other parameter is set to default) . . . . .	61
10.1	Schematic representation of the differences in main parameters for the wing of both the GE1 and GE+ . . . . .	63
10.2	Schematic representation of the differences in main parameters for the winglets of both the GE1 and GE+ . . . . .	63
11.1	Lift coefficient $C_L$ in function of the angle of attack $\alpha$ for the GE1 and GE+ geometry . . . . .	65
11.2	Drag coefficient $C_D$ in function of the angle of attack $\alpha$ for the GE1 and GE+ geometry . . . . .	66
11.3	Pitching moment $C_m$ in function of the angle of attack $\alpha$ for the GE1 and GE+ geometry . . . . .	67
11.4	Lift to drag ratio $L/D$ in function of the angle of attack $\alpha$ for the GE1 and GE+ geometry . . . . .	68
11.5	Lift coefficient $C_L$ in function of the sideslip angle $\beta$ for the GE1 and GE+ when $U_\infty = 18 \text{ m/s}$ and the $AOA = 2^\circ$ . . . . .	68
11.6	Drag coefficient $C_D$ in function of the angle of attack $\alpha$ for both engine modes (zero and full thrust) for the GE+ . . . . .	69
12.1	Lift coefficient $C_L$ in function of the free stream airspeed for different angles of attack and when no thrust is supplied . . . . .	71
12.2	Drag coefficient $C_D$ in function of the free stream airspeed for different angles of attack and when full thrust is supplied . . . . .	71

# List of Tables

1.1	Summary of the technical specifications of the GE1 . . . . .	3
4.1	Values of parameters that were investigated during the wind tunnel test campaign . . . . .	14
5.1	Summarization of the different geometry discretizations, their respec- tive number of panels in each direction, the percentage of error with respect to the converged value of induced drag and the computation time in seconds for a NACA0018 wing of aspect ratio 6 . . . . .	22
9.1	Summary of the parameters and their range of values for the para- metric study. Green cells represent the default values of the baseline geometry. . . . .	59
10.1	Adapted parameters for the new UAV geometry GE <sup>o</sup> . . . . .	62

# Part I

## Introduction

# Chapter 1

## Background and context

This master thesis is carried out in collaboration with the company Aircraft Traders Belgium s.a. which is developing a blended wing body UAV, *unmanned aerial vehicle*. The UAV's main purpose would be long distance aerial surveillance. For this matter, the UAV embarks a video camera surveillance module as well as an infra-red sensor. They can be deployed during the mission.

Surveillance drones have raised a lot of interest for various type of applications. Surveillance drones capture imagery or telemetry to use them in real-time or after their return to base. Applications vary from monitoring of large gatherings or protests, monitoring of a specific individual to surveillance of maritime traffic, monitoring of tsunamis, etc. They present many advantages compared to manned vehicles. The most obvious one, of course, being that a human operator can perform a task without risking his life. Helicopters or aircraft are sometimes not suited for specific missions because of the high noise emissions of their engines and/or blades. Drones are often equipped with electrical engines whose noise emissions are much lower. Because the payload they have to carry is usually much smaller, they are also much lighter and, hence, their operational cost is greatly reduced.

The embedded imagery hardware can vary from a simple camera to infra-red cameras allowing the drone to perform its missions not only during the day but also during the night. The data transfer in real time combined with image processing softwares further extend the potential of surveillance drone. Face recognition and live tracking of objects or individuals become possible.

The growth of drone usage is relatively new. Therefore, to this point, the lack of regulation has enabled the use of drones by all types of users and for any application. Awareness has been raised among users by the legislative powers of different countries to regulate the use of drones. Users now have to register their drones and to obey to certain rules when flying.

The first prototype is already built by Aircraft Traders and is called GE1, *Guardian Eye 1* (see Figure 1.1). It is used by the company to perform preliminary flight tests. In parallel, another prototype is being developed. This new prototype, GE2, is 50 % larger than the GE1. Simultaneously to the flight tests of GE1 and the development of GE2, Aircraft Traders would like to design an improved geometry

of the UAV. This upgraded prototype would then be called the GE<sup>+</sup>.

The GE1 is a 2.2 m span UAV that can be either piston engine or electrical engine driven. The GE1 is a pusher engine configuration. It can communicate with its base station either by 433 MHz radio communication or via 3G/4G mobile telecommunication technology. Take-off methods for the drone include normal take-offs from runways and catapult launches. A summary of the specifications of GE1 can be found in Table 1.1.



Figure 1.1: Picture of the GE1 in flight

<b>GE1</b>	<b>Electrical version</b>	<b>Piston engine version</b>
Wingspan	2.2 <i>m</i>	2.2 <i>m</i>
MTOW	6.5 kg	10.5 kg
Endurance	3 to 4 hours	8 to 10 hours
Cruise speed	25 knots/ 12.8 m/s	35 knots/ 18 m/s
Ceiling	5000 ft MSL	15000 ft MSL
Material	Fiberglass and carbon fiber	Fiberglass and carbon fiber
Maximum payload	4 kg	6 kg

Table 1.1: Summary of the technical specifications of the GE1

A set of CAD files of the GE1 has been made available by the company. Those were obtained by scanning the UAV with three dimensional scanners. This was performed by the company Argon Measuring Solutions. Those files will serve as baseline geometry. The main geometry parameters of the baseline design are represented in Figure 1.2.

Furthermore, a test campaign in the wind tunnel of the University of Liège has already been performed in November 2014. Those results will serve as reference data for comparison with numerical results.

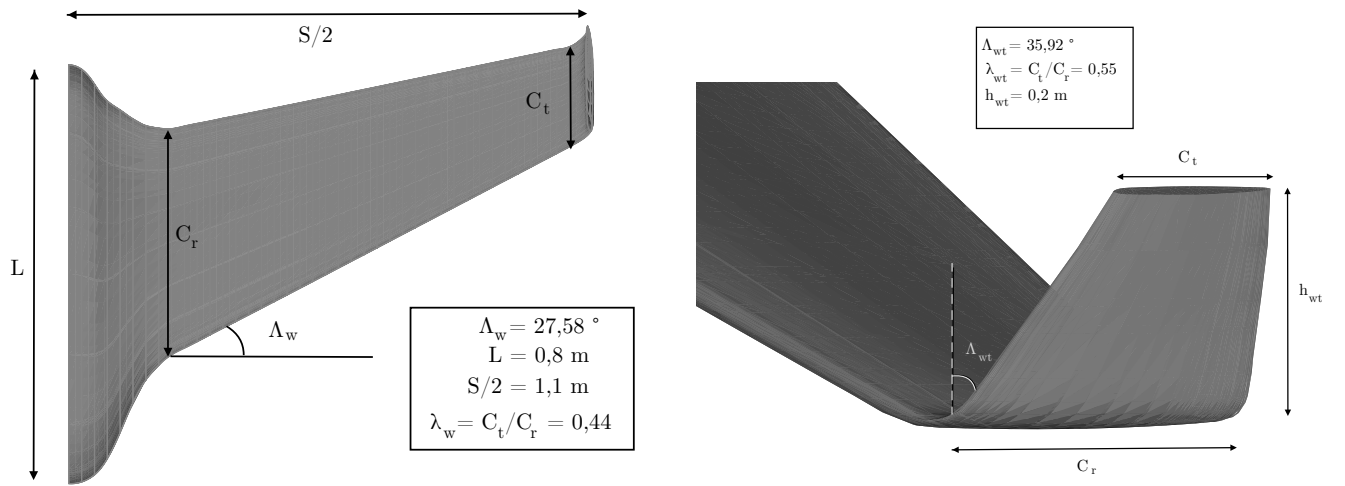


Figure 1.2: Schematic representation of the main geometry parameters of the baseline design, GE1



# Chapter 2

## Objectives

As already mentioned, the goal of this master thesis is, first of all, to assess the aerodynamic performances of the GE1, and in a second phase, to propose an aerodynamically enhanced geometry GE<sup>+</sup>.

The optimisation phase of an aircraft is of key importance. The superiority of aerodynamic performance acts as a competitive advantage on the market. As an example, the aerodynamic performance of any aircraft is vital as it could lower the energy consumption and hence increase the range of operations. The aerodynamic performance is obviously not the only aspect where optimization is possible. Structural analysis could potentially reduce the weight of the aircraft. The flight dynamic behaviour could also be studied and improved (further works will be discussed at the end of the work). Because all those disciplines work together and are linked to each other, it becomes complex to perform a fully multi-disciplinary design optimization. This work focusses on the aerodynamic performances of the aircraft.

In the first part of the work, lower and higher fidelity aerodynamic tools will be used to assess the aerodynamic performances of the BWB. A comparison of the different tools will be performed in order to quantify their relative error with respect to experimental results.

In the second part of the work, a sensitivity analysis of different geometry parameters (taper ratio, sweep angle, geometry of the winglets, etc.) will be performed. The performances of the different combinations of parameters will be used to maximize an objective function. This will lead to an improved geometry of the GE1, called the GE<sup>+</sup>. The respective performances of both design will then be compared.

The company Aircraft Traders s.a. has committed to print a reduced sized three dimensional model of the improved geometry, GE<sup>+</sup>mini, for verification of the predicted performances in a subsequent wind tunnel test campaign. Preliminarily to this wind tunnel test campaign, a sensitivity analysis on the Reynolds number will be performed to ensure that the reduced sized model will accurately represents the physics of the full size model.

# Chapter 3

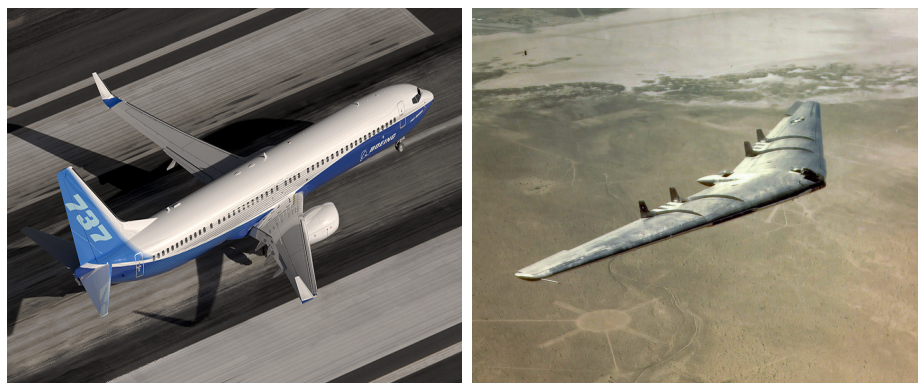
## State-of-the-art

Blended wing body configurations have been widely investigated over the last few years. In a nutshell, the main advantages of this type of unconventional configuration are an increased fuel efficiency, a reduced noise emission and similar or better payload capacities than conventional airliners.

UAV's, on their side, are receiving a lot of attention for military applications as well as recreational purposes and experience an increased adoption around the world. In 2013, the United States Department of Transportation published a report predicting that by 2035, the number of unmanned aircraft operations could surpass manned aircraft operations in the United States of America [19].

### 3.1 Definition of a blended wing body

A blended wing body can be defined as a fixed-wing aircraft that blends the characteristics of a conventional fixed-wing configuration (distinct fuselage and wing) and a flying wing in a way that the transition between fuselage and wing is smooth. A representation of a conventional airliner and a flying wing is presented in Figure 3.1.



Conventional airliner, here a Boeing 737 [9]

Picture of a flying wing, here a Northrop YB-49, USAF Archive [10]

Figure 3.1: Comparison of different aircraft configurations

A blended wing body enables the aircraft to have a higher lifting surface as the fuselage also participates in the lift generation. It also reduces the interference at the fuselage-wing interface.

## 3.2 Definition of an unmanned aerial vehicle

An unmanned aerial vehicle can be defined as any type of aerial vehicle without a human pilot on board. UAV's can be of various types including rotor wing aircraft, fixed wing aircraft, etc. In this thesis, aerial unmanned vehicles refer to fixed-wing aerial vehicles.

UAV's are controlled by human pilots from a remote distance or can be fully autonomous. In this case, the autopiloting software is integrated in on-board computers. The flightpath for a specific mission can be pre-programmed into the memory of the on-board computer.

## 3.3 History of blended wing bodies

The history of blended wing bodies is closely related to the history of flying wings. This history review is not an exhaustive list of all attempts to blended wing configurations. However, some of the most forward-thinking models will be presented.

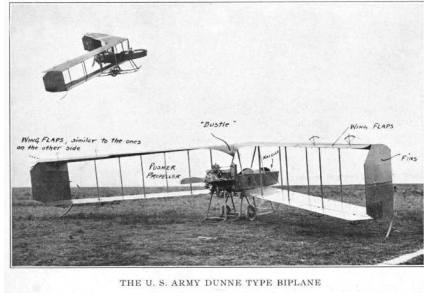
The search for the most adequate geometry dates back to the roots of flying. As early as in 1910, Lieutenant John William Dunne, a British soldier who was also an aeronautical engineer, designed and successfully flew what can be called the first flying wing of the history of flight.

J.W. Dunne had been studying the performance of his flying wing designs on smaller scale models, comparing it with the studies of others. He finally came up with the design of the Dunne D.5, see Figure 3.2a. He successfully flew the biplane for two and a quarter of a mile. As he expected, the stability of the aircraft was outstanding. He would later successfully fly across the English channel. The performances of the flying wing brought interest and an incentive for further studies.

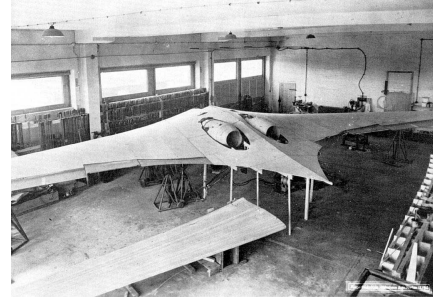
The editors of the issue of Flight Magazine of June 18, 1910 wrote:

*"There is no doubt that this flight marks an important period in the development of the aeroplane, and although the outcome of it can only be vaguely surmised, this in no way detracts from its present importance, and should increase, rather than otherwise, the amount of interest in the machine itself."* (Flight, June 18, 1910)

From then on, throughout the twentieth century, companies, academic institutions have been investigating flying wing and blended wing configurations. Numerous aircraft can be linked to those configurations. However, two manufacturers have played a major role in the development of flying wings and blended wing bodies. Northrop aircraft and the Horten brothers.



(a) Dunne D.5 ready to take-off in 1917, Flight Magazine [22]



(b) Horten Ho. 229 under construction, Nurflügels [6]



(c) Northrop N-1M, Smithsonian National Air and Space Museum [2]



(d) Northrop B2 Spirit, National Museum of the US Air Force [18]

Figure 3.2: Multiple pictures of early or recent attempts to flying wing and blended wing body designs

Walter and Reimar Horten, also called the Horten brothers, were German pilots who from a young age were involved in numerous flying clubs. They would become the experts of flying wings by experimenting flying wing configurations on scale model gliders. In the 1930's, they built numerous full-scale models, with successive enhanced designs.

During the Second World War, Walter and Reimar got assigned to the Luftwaffe, but somehow continued their researches. They ended up building the first jet powered flying wing, the Horten Ho. 229 (see Figure 3.2b).

Northrop aircraft is the second manufacturer that played a keyrole in the development of flying wings and blended wing bodies. Northrop Aircraft started studying flying wings in 1928, with an experimental model, the X-216H. This experimental aircraft later evolved to the operational N-1M. The N-1M, see Figure 3.2c, was a flying wing with two pusher engines, the cockpit was located in the center of the airframe on the extrados. Its flying performances were marginal but it paved the way for more succesfull and advanced designs. Among those more succesfull designs, one can cite the Northrop YB-49, see Figure 3.1. A jet-powered heavy bomber intended for the United States Air Force developed shortly after the Second World War. The YB-49 would then in turn be of valuable knowledge for the well-know and still in

service Northrop B-2 Spirit stealth bomber, see Figure 3.2d.

Parallel to the works of the Horten Brothers and Northrop Aircraft, which were all flying wing configurations, smaller initiatives emerged during the Second World War.

More recently the NASA, National Aeronautics and Space Administration, began developing an experimental blended wing body in collaboration with the Stanford University, the BWB-17 concept. A two meter span model of the BWB-17 successfully flew on October 10, 1995. Another important project initially funded by NASA is the Boeing X-48 concept which was jointly developed by Boeing, NASA and Cranfield Aerospace. The project is managed by aerodynamicist Robert H. Liebeck.

### 3.4 Existing research on BWB

Many articles have been published in recent years focusing on the potential advantages of BWB for large commercial aircrafts.

In 2004, R. H. Liebeck studied the feasibility and potential performances of a 400 and 800 BWB passenger commercial aircraft, Liebeck [15]. The aircraft was intended for a 7000 nautical mile range at a Mach number equal to 0.85. He based his approach on an expected 2010 entry into service, hence fixing the engine and structural technology available at that time. Liebeck demonstrated that a streamlined BWB model could lead to a reduction of 33% of the total wetted area for a given volume, that is, considering all control surface and engines. Knowing that the lift to drag ratio,  $L/D$ , is linked to the wetted area aspect ratio,  $b^2/S_{wet}$  (Raymer [24]), by formula,

$$\left(\frac{L}{D}\right) = \frac{1}{2} \sqrt{\frac{\pi \epsilon}{C_{f_e}} \frac{b^2}{S_{wet}}}, \quad (3.1)$$

where  $\epsilon$  is the span efficiency factor typically between 0.7 and 0.85,  $C_{f_e}$  is the equivalent skin friction coefficient, the potential increase in aerodynamic efficiency is substantial.

The reduced wetted area is not the only factor enabling a higher lift to drag ratio. For example, the absence of fin eliminates its drag penalty in friction and induced drag.

After a three year initial feasibility and performance study, Liebeck deemed the 800 passenger BWB inappropriate for further study mainly because the forecast for the improvement of the technology did not allow for the construction of an aircraft of that size. Also, there was a lack of aircraft transporting the same amount of passengers to compare with.

Refocusing his work on the 450 passenger BWB concept, the resulting model could be compared to in-service transport aircraft as the B747, A340 and the A380. The aircraft wing span had to be limited to 80 m due to airport requirements. The

BWB 450 model was optimized using a Boeing proprietary code, WingMOD. WingMOD is a program combining a vortex-lattice code and a monocoque beam analysis.

The final design has been compared to the A380-700 which has approximately the same payload capacity and range. The results of this comparison are shown in the Figure 3.3.

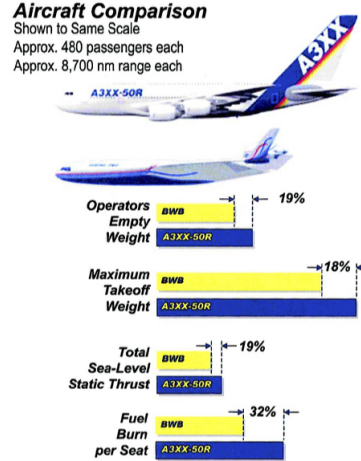


Figure 3.3: Comparison of performances between the A380-700 and the resulting design of the BWB-450

Those results illustrate the potential performance gains for such unconventional configurations. A reduction of the fuel burn per seat has been estimated to 32%. This reduction could have an important economical impact for airlines. Besides the 18% reduction in operating empty weight, the 19% reduction in total sea-level static necessary for good operation of the aircraft is striking. This allows the suppression of one engine unit compared to the A380, which has four.

The noise emissions of BWB configurations have been expected to reduced too. This is an effect of the lower required thrust and the fact that the engines are often placed on top of the BWB. The body of the aircraft then acts as a shield for radiated noise with respect to the ground. In 2010 the NASA Langley Research Center published a paper quantifying this noise reduction, Thomas [27]. The baseline blended wing body was assessed at 22 dB below the FAA Stage 4 certification level. This is a regulation imposed by the FAA, the Federal Aviation Administration, that imposes aircraft and engine manufacturers to build aircraft and engines meeting specific decibels levels. Besides the baseline concept, seven other configurations were tested where near term technology advancements were implemented to study the potential noise reduction. The best noise reduction with short term technology was assessed to 40 dB below the Stage 4 requirements.

Recent studies have thus shown that a significant gain in efficiency could be achieved with BWB. There are, however, some issues concerning large commercial aircraft that needs adressng such as passenger safety and emergency exits. The shape being radically different than conventional aircraft, the structural behaviour of such

BWB's were extensively studied in [5, 15, 17, 16, 17]. However, these issues are specific for large commercial aircraft. In this master thesis the emphasis is put on UAV's, making these issues less or even not relevant at all.

Some research concerning the aerodynamics of BWB UAV has already been done. In 2009, W. Wisnoe published the results of wind tunnel experiments and CFD analysis, Wisnoe [29]. Different aerodynamic coefficients were computed at Mach numbers of 0.1 and 0.3. The CFD analysis was performed using the proprietary ANSYS Fluent software. In 2011, a team of eight student at the Florida Institute of Technology worked on the design and construction of a 5 m wingspan BWB UAV and successfully built a composite prototype, Thompson [28].

Using high-fidelity tools such as a RANS computation is often very time-consuming. Hence, when varying the geometry and studying the influence of geometrical parameters, a full CFD analysis is often required to validate the results from low-fidelity aerodynamic analysis tools. With this in mind, K. Lehmkuehler [14] investigated a BWB UAV with a low-fidelity aerodynamic analysis tool, PanAir [7]. The software PanAir is a fully three dimensional panel method for solving potential flows around arbitrary s. PanAir will be discussed in more details in Section 5.1 and 5.2.

Lastly, a typical example of geometry optimization was performed by Qin et al. in [23]. They performed an inverse twist design by imposing an ideal spanwise lift distribution. The ideal lift distribution is supposed to minimize the induced drag. The different local airfoil sections were then twisted separately with respect to the baseline configuration to meet the local required lift coefficient. A new twist distribution resulted from the angles of twist of the local sections. The geometry was then studied by a panel method as a whole. When considering the geometry as a whole, the imposed two dimensional lift distribution is not met per se. The differences or discrepancies between the three dimensional results and the ideal imposed lift distribution are then used to incrementally adjust the twist distribution to match the ideal lift distribution.

# Part II

## Aerodynamic tools



As earlier mentioned, the aerodynamic performances of the UAV will be analysed using different tools. In Part II, the choice of the different tools will be discussed and their results will be validated with respect to reference sets of data. The different tools are, a low fidelity software, typically a three dimensional panel method, a high fidelity one, typically a complete computational fluid dynamics RANS simulation, and finally a set of experimental data.

The different methods that will be used have to best represent the actual physics phenomenon of the real model flow. For this matter, it is important to highlight some of the features of the flow. The idea being that, when the different methods will be introduced, one should then be able to tell if the described method is true to the real phenomenons.

The flow is, of course, viscous. The flow can be considered steady as the properties of the GE1 will be assessed for steady configurations. Flows can be laminar, turbulent or both and are then called transitional flows. The Reynolds number of the GE1 at a free-stream velocity of 18 m/s is equal to,

$$Re_{GE1} = \frac{U_{\infty} MAC}{\nu} = 1096023, \quad (3.2)$$

where  $U_{\infty}$  is the free stream velocity,  $MAC$  the mean aerodynamic chord of the GE1 and  $\nu$  the kinematic viscosity. The flow is thus turbulent. The CFD model will thus have to model the turbulence.

Compressibility effects can be important in a simulation or less relevant depending on the Mach number. Here, the Mach number is very low and hence the flow may be considered as incompressible.

# Chapter 4

## Experimental results

The Guardian Eye 1 has been tested in the wind tunnel of the University of Liège in November 2014. The extended report and characteristics of the wind tunnel can be found in Andrianne [4].

The forces and moments were measured using a six component sensor located on the floor of the wind tunnel. The sensor was linked to the UAV by a 70 cm long aluminium beam attached at the location of the rear landing gear.

The parameters that varied during the tests were the airspeed, the angle of attack and the value of thrust. For each stabilised airspeed, the angle of attack was changed as well as the values of thrust. A summary of the parameters is shown in Table 4.1.

Airspeeds [ $m/s$ ]	$\alpha$ [ $^\circ$ ]	Thrust/Maximum thrust
7	0	0
11	5	
15	10	1
19	15	

Table 4.1: Values of parameters that were investigated during the wind tunnel test campaign

During the tests, the effect of the Reynolds number on the lift and drag coefficient has been investigated. The airspeed in the wind tunnel was varied from 7 to 20 m/s and the angle of attack was changed from  $0^\circ$  to  $15^\circ$  with increments of  $5^\circ$ . The case where the thrust was at zero and full power has been studied. The conclusion of the Reynolds sensitivity analysis were that the lift coefficient was rather constant for airspeeds above 10 m/s, this for all angles of attack and for both engine modes (maximum and zero power). The drag was also independent of the airspeed in the case where no thrust was supplied. However, this was not the case when full thrust was provided. In that particular case, a dependency of the drag coefficient with the airspeed could be observed. This is due to the slipstream of the propeller disturbing the flow on the aircraft. A speed equal to 15 m/s was chosen to perform the rest of the tests.

Secondly, the variations of the aerodynamic coefficients in function of different angles

of attack were studied for both engine modes. It was shown that the drag coefficient was negative at an angle of attack of  $0^\circ$  when the thrust was maximum. However, the lift coefficient was shown to be almost independent of the supplied thrust.

Results were then compared to other BWB aircraft. After comparison, it was proposed to increase the drag coefficient measured during the wind tunnel test by a constant offset of  $\Delta C_D = 0.0035$ . It was considered by the author that this correction was safe at that stage of the analysis.

Finally, the lift to drag ratio was plotted and an estimate of the required propulsive power to counteract the drag force was given.

# Chapter 5

## Low fidelity aerodynamic tool

### 5.1 Choice of software

Firstly the choice of low fidelity tool has to be discussed. In the works of Lehmkuehler [14], the preliminary design was performed using the Athena Vortex Lattice program. This is a program for the aerodynamic analysis of aircraft of arbitrary configurations. It uses a vortex lattice method for the lifting surfaces and a slender body model for the fuselage. It can also analyse the flight dynamics properties of the aircraft. It is very useful for testing various geometries and obtain all the stability derivatives and aerodynamic coefficients of a model. It is, however, not as flexible as other programs when defining a geometry. It is, for example, more complex to define a lifting surface for which the airfoil profile does change in the spanwise direction.

An alternative to quick but yet satisfactory results is a three dimensional panel method. A panel method numerically solves a linearised set of equations by dividing the geometry into panels, each having a certain singularity strength. The method will be described in the following section. Few softwares using such method are available.

PANUKL is a low order panel method package developed by the Aircraft Design Department of the Warsaw University of Technology. It is particularly good at post-processing the data and has a built in graphical user interface module to plot the different aerodynamic coefficients on the geometry such as pressure coefficients.

The other principal panel method software is PanAir. PanAir has been developed by Boeing Company and was contracted by NASA. It implements a higher order panel method, allowing better final results. The higher order code and the use of PanAir in a couple of scientific papers ([14, 23]) makes it the first choice compared to PANUKL.

### 5.2 PanAir implementation

In this section, the implementation of the three-dimensional panel method of PanAir will be explained. This allows for a better comprehension of the different boundary conditions that have to be imposed, but also allows to highlight the hypotheses

and limitations behind such a software.

Hypothesizing that the flow is inviscid and that there are no heat sources or heat diffusion, the conservation laws can be put under the form of the Euler equations. Furthermore, if the total derivative notation is introduced, the Euler equations write,

$$\left. \begin{aligned} \frac{D\rho}{Dt} + \rho \operatorname{div} \vec{V} &= 0 \\ \rho \frac{D\vec{V}}{Dt} + \vec{\nabla} p &= 0 \\ \rho \frac{D}{Dt} \left( e + \frac{1}{2} V^2 \right) + \operatorname{div}(p \vec{V}) &= 0 \end{aligned} \right\} \quad \text{Euler equations,} \quad (5.1)$$

where  $\rho$  is the density of the fluid,  $\vec{V}$  is the velocity vector,  $p$  is the pressure and  $e$  is the internal energy.

These equations are valid for an unsteady, compressible, inviscid, adiabatic and three dimensional flow.<sup>1</sup>

With the additionnal assumptions that the flow is steady, incompressible and irrotational, a velocity potential can be defined as,

$$\vec{\nabla} \Phi = \vec{V} \quad (5.2)$$

The Euler equations then become,

$$\Delta \Phi = 0 \quad (5.3)$$

$$(\vec{V} \cdot \nabla) \vec{V} + \frac{1}{\rho} \vec{\nabla} p = 0, \quad (5.4)$$

where the Equation 5.3 represents the Laplace equation and the Equation 5.4 represents the Bernoulli equation.

Flow conditions where all the above mentioned hypotheses have been made is called a potential flow. The steps for solving a potential flow are as follows,

- Solve the velocity potential (in this particular case achieved by using a panel method)
- Enforce boundary conditions on non-disturbance of far field and the impermeability of the body surface (either by a Neumann or Dirichlet boundary condition).
- Retrieve the velocity from the potential by the Equation 5.2
- Compute the pressure from the Bernoulli equation (Equation 5.4)

---

<sup>1</sup>To be fully complete, two additional state equations are required,  $e = c_V T$  and  $p = \rho R T$

The Laplace equation being a linear equation, the solution of the velocity potential can be constructed by a superposition of different (more simple) solutions. Hence, if  $\Phi_1$  and  $\Phi_2$  are solutions of the Laplace equation, then,

$$\Phi_3 = \Phi_1 + \Phi_2, \quad (5.5)$$

is also a solution of the Laplace equation.

A solution of the flow can thus be decomposed into the solution of the uniform flow and the flow induced by the geometry as,

$$\Phi = \Phi_\infty + \Phi_{GEOM} \quad (5.6)$$

If the hypothesis of incompressibility is not made, and hence the flow is compressible, the equations for a potential flow can be corrected for the compressibility effects as,

$$(1 - M_\infty)\Phi_{xx} + \Phi_{yy} + \Phi_{zz} = 0 \quad (5.7)$$

$$\frac{1}{2}V^2 + \frac{\gamma}{\gamma - 1} + \frac{p}{\rho} = cst, \quad (5.8)$$

where Equation 5.7 is the Prandtl-Glauert equation with  $M_\infty$  is the free stream Mach number and Equation 5.8 is the compressible Bernoulli equation.

To solve a potential flow, a recurrent technique is the panel method. The three dimensional panel method is based on the discretization of the geometry using quadrilateral panels on which a certain distribution of singularities is imposed. This distribution of the singularities' strength can be constant, linear or even quadratic. The velocity potential can then be calculated at each point of the flow.

In the implementation of PanAir, a higher-order method is used. That is, imposing a quadratic distribution of doublets on the panels. The quadratic distribution was introduced because of numerical stability challenges in supersonic conditions if a panel was too inclined with respect to the uniform flow direction. With a lower order panel method, the constant strength value on each panel did not allow a continuous distribution on the entire geometry. The solution to increase the numerical stability was to impose a doublet distribution that was continuous on the entirety of the geometry. A review of the different panel methods and their implementation can be found in Erickson [11].

The following formulas for the computation of velocity potentials come from Erickson, notations and conventions may vary between different technical reports.

The velocity potential at point  $P$  due to the influencing panel  $Q$  (i.e. the potential that is only due to the geometry,  $\Phi_{GEOM}$ ) is equal to,

$$\Phi_P = \int \int_S [\sigma \frac{1}{4\pi} \Phi_P^S(\vec{X}_Q) + \mu \frac{1}{4\pi} \Phi_P^D(\vec{X}_Q)] dS_Q, \quad (5.9)$$

where  $\sigma$  is the source strength,  $\mu$  is the doublet strength,  $S_Q$  is the surface of panel  $Q$  and  $\Phi_P^S$  and  $\Phi_P^D$  are respectively the unit point sources and doublets influence of  $Q$  on  $P$ . They are given by,

$$\Phi_P^S(\vec{X}_Q) = \frac{-1}{R(\vec{X}_P, \vec{X}_Q)} \quad (5.10)$$

$$\Phi_P^D(\vec{X}_Q) = \hat{\mathbf{n}} \frac{-\vec{R}(\vec{X}_P, \vec{X}_Q)}{R^3}, \quad (5.11)$$

where  $\vec{R}$  is a vector from point  $P$  to  $Q$ ,  $\hat{\mathbf{n}}$  is the unit normal vector on panel  $Q$  and  $R$  is the hyperbolic distance and is given by,

$$R = \sqrt{(X_Q - X_P)^2 + (1 - M_\infty^2)^2 [(Y_Q - Y_P)^2 + (Z_Q - Z_P)^2]} \quad (5.12)$$

Knowing the potential  $\Phi_P$ , the induced velocities can be calculated with Equation 5.2. The velocity at a point  $i$  due to all  $N$  panels writes,

$$\vec{V}_i = \vec{V}_\infty + \sum_{j=1}^N \vec{v}_{ij}, \quad (5.13)$$

where  $\vec{v}_{ij}$  is the induced velocity at point  $i$  due to the source-doublet distribution at panel  $j$ .

At this stage, the singularities' strengths are still unknown. By applying a set of boundary conditions, sources and doublets strengths will be obtained resolving a system of linear equations.

If the panel is impermeable, the normal component of the velocity is zero, hence,

$$\vec{V}_i \cdot \hat{\mathbf{n}}_i = \left( \vec{V}_\infty + \sum_{j=1}^N \vec{v}_{ij} \right) \cdot \hat{\mathbf{n}}_i = 0 \quad (5.14)$$

or,

$$\sum_{j=1}^N \vec{v}_{ij} \cdot \hat{\mathbf{n}}_i = -\vec{V}_\infty \cdot \hat{\mathbf{n}}_i \quad (5.15)$$

Previous equation can be rewritten as,

$$\sum_{j=1}^N VIC_{ij} \lambda_j = b_i \quad (5.16)$$

where  $VIC_{ij}$  are called the velocity influence coefficients,  $b_i = \vec{V}_\infty \cdot \hat{\mathbf{n}}_i$  and  $\lambda_j$  are the source and doublet singularity parameters.

If the operation is repeated for the  $N$  panels, a system of equations,

$$[AIC] \{\lambda\} = \{b\}, \quad (5.17)$$

where  $[AIC]$  is the matrix of aerodynamic influence coefficients and  $\{\lambda\}$  the vector of unknown singularity parameters.

Another very important boundary condition to impose is the Kutta condition. For uniqueness of the flow, the Kutta condition is imposed by adding wake panels starting from the trailing edge of the lifting surface. Wake panels are usually horizontal panels stretching from the trailing edge of the lifting surface to a specific distance downstream of the flow.

### 5.3 Convergence analysis of the mesh

As the geometry is divided into a finite number of rectangular panels. A question that needs to be addressed is the number of panels necessary to obtain an accurate set of aerodynamic coefficients.

The PanAir program requires the entry of parameters such as the number of panels spanwise and the number of panels chordwise. To study their influences, the evolution of a couple of aerodynamic coefficients will be monitored. Tests will be performed on a NACA 0018 wing of aspect ratio equal to six.

The methodology will be as follows. In the first instance, the number of chordwise panels will be fixed at 60, while the number of spanwise panels will be varied from 4 to 36. Then, the number of spanwise panels will be fixed to 32 and the chordwise number of panels will be varied from 20 to 140. Tests are performed at an angle of attack equal to  $6^\circ$ .

In panel methods forces and moments are obtained by integrating the pressure distribution on the nonwake surfaces. As defined in the PanAir userguide [25], they can be calculated as,

$$F = -\frac{1}{S_{ref}} \int_S C_p \bar{n} dA \quad (5.18)$$

$$M = -\frac{1}{S_{ref} L_T} \int_S C_p (\bar{P} - \bar{R}_0) \times \bar{n} dA, \quad (5.19)$$

where  $F$  is a three dimensional force,  $S_{ref}$  is the full airplane reference area,  $\bar{n}$  the unit normal vector to the panel,  $dA$  the surface of the panel,  $C_p$  the second-order pressure coefficient,  $M$  is a three dimensional moment,  $L_T$  a reference length,  $\bar{P}$  the point of integration on the panel and  $\bar{R}_0$  is the moment reference location.

Note that as the viscosity effects are not taken into account, the drag computed by PanAir will not include the friction drag part. It will be seen that a correction can be applied to get a more representative value of the total drag.

The Figure 5.1 represents the evolution of the induced drag coefficient when the number of spanwise panels is increased while the number of chordwise panels is fixed to 60. It can be observed that the value of induced drag converges to a finite value. When the number of panels is equal to 28, the induced drag has already converged to its ideal value.



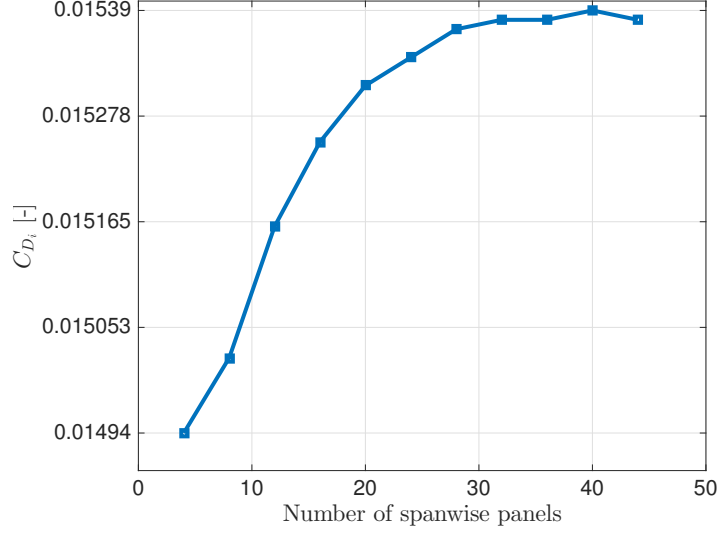


Figure 5.1: Evolution of the induced drag coefficient  $C_{D_i}$  in function of the number of spanwise panels with a number of chordwise panels set to 60 for a NACA 0018 of aspect ratio equal to 6 at an AOA of  $6^\circ$

The same methodology can be applied with increasing the number of chordwise panels with a fixed number of spanwise panels. Once again, the induced drag converges rapidly to a specific value. The error between the induced drag when having a number of chordwise panels of 60 and the asymptotic value is in the order of  $10^{-4}$ .

As mentioned in Erickson [11], increasing the number of panels too much can introduce numerical instabilities. Hence, the geometry discretization will be a trade-off between a high number of panels as to represent the aerodynamic properties of the geometry as accurately as possible and a limited number of panels to avoid instabilities.

A good way to see if instabilities have been introduced into the model is to plot the pressure distribution along a section of the wing. Small oscillations appearing in the pressure distribution are a sign of instabilities. This has been done in Figure 5.3. It can be observed that there are no oscillations, hence the results seem free of instabilities.

To conclude on the geometry discretization, one can define three geometry discretizations based on the target accuracy and target computational time. A geometry discretization that is coarse will be defined by 12 panels spanwise and 60 panels chordwise, a medium one will be defined by 30 panels spanwise and 80 panels chordwise and a fine one will be defined by 40 panels spanwise and 120 panels chordwise. The three-dimensional geometry discretizations are represented in Figure 5.4.

A summary of characteristics of the different discretizations is represented in Table 5.1. It can be noted that the computation time drastically increases from the coarse discretization to the fine one. Even if it is the most accurate representation, it makes

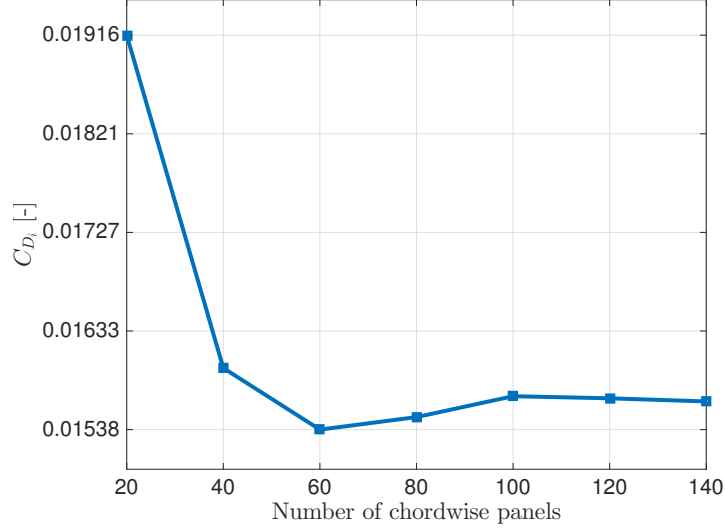


Figure 5.2: Evolution of the induced drag coefficient  $C_{D_i}$  in function of the number of chordwise panels with the number of spanwise panels set to 32 for a NACA 0018 of aspect ratio equal to 6 at an AOA of  $6^\circ$

	Coarse discretization	Medium discretization	Fine discretization
$N_{panels}$ spanwise	12	30	40
$N_{panels}$ chordwise	60	80	120
Percentage of error of $C_{D_i}$	2.0946 %	0.3879 %	0 %
Computation time [s]	0.894	7.769	37.605

Table 5.1: Summarization of the different geometry discretizations, their respective number of panels in each direction, the percentage of error with respect to the converged value of induced drag and the computation time in seconds for a NACA0018 wing of aspect ratio 6

sense to define a medium discretization to combine a relatively quick computation time as well as a relatively accurate result. For the validation of PanAir (in Chapter 5.4), the medium discretization will be used.

## 5.4 Validation of PanAir

The results of the panel method implemented in PanAir will be compared to results coming from different theories or experimental results in order to validate their accuracy. This section will thus try to assess if the three-dimensional panel method is a viable technique to study the performances of the BWB UAV.

For now the number of panels or the degree of discretization has been discussed. It

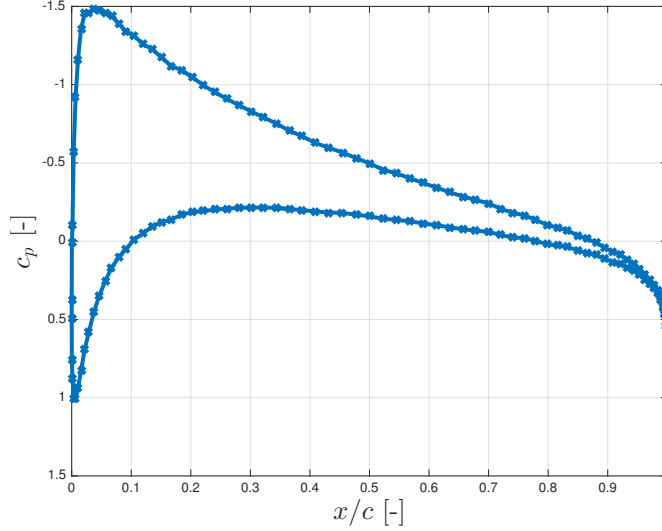


Figure 5.3: Pressure distribution along a section of the wing at  $y = 1.59$  when the number of chordwise panels is equal to 140 for a NACA 0018 of aspect ratio equal to 6 at an AOA of  $6^\circ$ . The pressure coefficient  $C_p$  is plotted in function of the chordwise coordinates  $x/c$

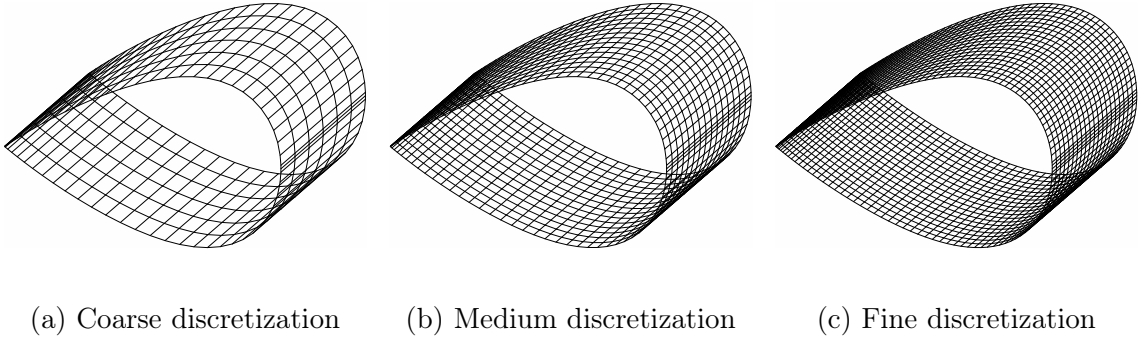


Figure 5.4: Geometry discretization for a NACA 0018 wing of aspect ratio 6

still needs to be proved that those results are in accordance with the results that would be obtained in the same conditions with other techniques.

The tests will be performed on a wing composed of NACA 0018 airfoil profiles. Results from an investigation performed by the NACA, the National Advisory Committee for Aeronautics, in their full-scale wind tunnel to study the aerodynamic performances of the NACA 0009, 0012 and 0018 will be used as reference data (Goett, [12]). A code implementing the Prandtl lifting line theory has been developed and will be used as a secondary point of reference.

The aspect ratio of the wing is equal to six while the free stream velocity will be set to achieve a Reynolds number of  $3.4 \times 10^6$  to be concordant with the tests performed by the NACA. For the PanAir simulation, a medium geometry discretization will be used.

In Figure 5.5, the lift coefficient for different theories has been plotted in function of the angle of attack. The two dimensional thin airfoil theory predicts that the slope of the lift coefficient is equal to  $2\pi$ . Due to three dimensional effects, we expect the slope for data that has been obtained for finite wings to be smaller than this value. This was confirmed by the tests. The lift coefficients obtained via the Prandtl lifting line theory are very similar to the ones of PanAir. The slope of the curve of experimental results is, similarly, smaller than the one of PanAir. This decrease of the slope can be attributed to the presence of viscosity. The viscosity changes the pressure distribution over the wing and as a result alters the lift coefficient. Note that the results coming from all the different theories go through the origin ( $C_L = 0$  and  $\alpha = 0$ ) as one should expect with symmetrical airfoils.

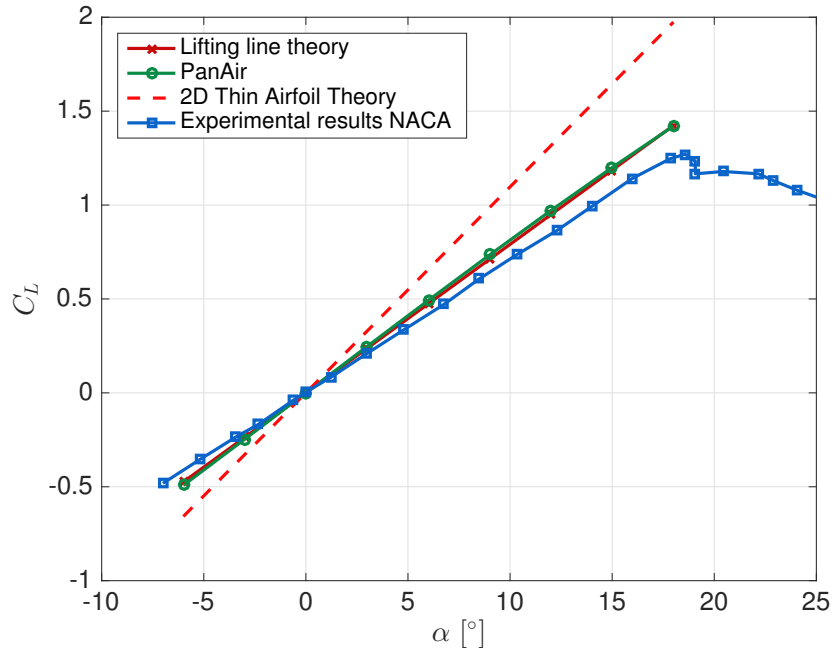


Figure 5.5: Lift coefficient  $C_L$  in function of the angle of attack  $\alpha$  for different theories: the Prandtl lifting line theory, the PanAir program, the two dimensional thin airfoil theory and the experimental results of the NACA report by Goett [12] for a NACA0018 wing of aspect ratio 6

A similar comparison can be made about the drag coefficient. This has been done in Figure 5.6. A very important distinction has to be made between the PanAir results, the Prandtl lifting line theory and the experimental results concerning the drag. The experimental results is the only listed method where the measured drag is the total one. This means that the drag measured experimentally comprises all the components of the drag, i.e. the parasite and the induced drag. Whereas, PanAir and the lifting line theory only represent the induced drag. The drag coefficients for PanAir and the lifting line theory are very similar and represent the same quantity ( $C_{Di}$ ). The drag coefficient of the experimental results is non zero for an angle of attack of zero. This is due to the additional friction and form drag. The offset of drag

coefficient at zero angle of attack is equal to 0.008. This offset does not, however, remain constant when the angle of attack varies. As the angles of attack increase the experimental results intersect the PanAir results curve. At this stage ( $\alpha = 9^\circ$ ), the PanAir results become an overestimation of the drag coefficients. A summary of the different components of the drag is shown in Figure 5.7, this schematic representation will be used to highlight the components of the drag that are neglected or the ones that need to be added to the model (schematic representation from Gur [13]).

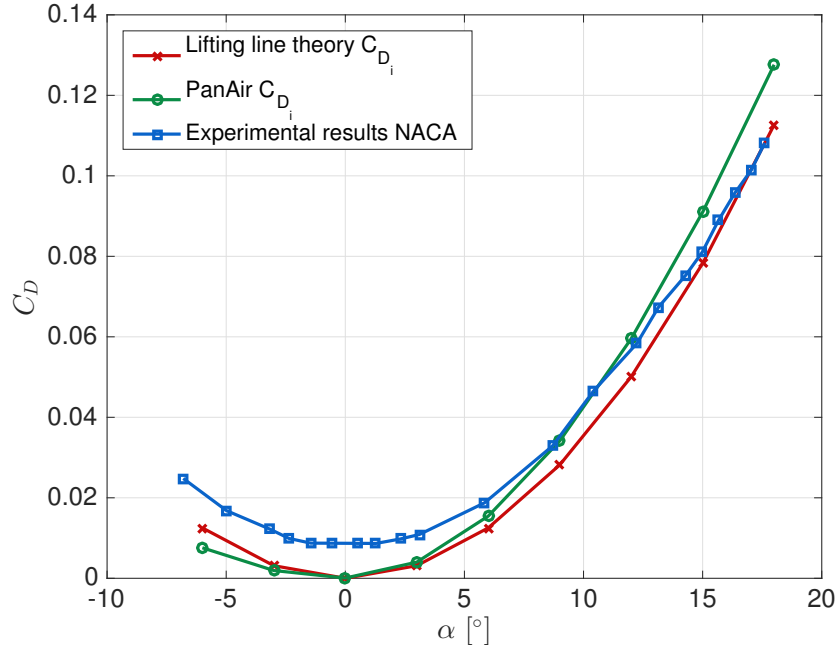


Figure 5.6: Drag coefficient  $C_D$  in function of the angle of attack  $\alpha$  for different theories: the Prandtl lifting line theory, the PanAir program and the experimental results of the NACA report for a NACA0012 wing of aspect ratio 6 [12]

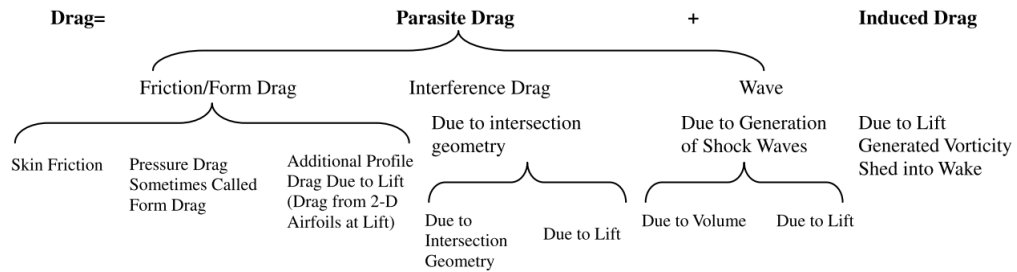


Figure 5.7: Schematic representation of the different components of the drag (illustration from Gur [13])

An interesting point is to see if it is possible to model the parasite drag. Should it be possible, a correction of the induced drag could be introduced to match the total drag or at least get a better approximation of it. In the case of a BWB, the

interference drag is small. This is due to the smooth blending of fuselage and wing. Hence, the modelling of the interference drag will be neglected. Wave drag occurs in the presence of shock waves. The flight conditions of the GE1 do not involve shock waves as the Mach number is very low. The most important part of the parasite drag will thus be the friction and form drag.

An empirical formula can be used to estimate the friction and pressure drag. This drag coefficient is given by,

$$C_{D_f} = C_F FF \frac{S_{wet}}{S_{ref}}, \quad (5.20)$$

where  $C_F$  is a flat-plate skin friction coefficient,  $FF$  is the form factor of the studied component/body,  $S_{wet}$  is the wetted surface and  $S_{ref}$  is the reference surface.

Many formulas exist for the calculation of the flat-plate skin friction coefficient. The comparison of the different models is out of scope of this work, but it has been shown that the differences remain small (Paterson [21]). Hence, the most well-known and used empirical formulas will be used.

For the flat-plate skin friction coefficient, the Schlichting equation is used,

$$C_f = [2 \log_{10}(Re) - 0.65]^{-2.3}, \quad (5.21)$$

which is valid if  $Re < 10^9$ .

For the form factor of the wing the Torrenbeek equation is used and is given by,

$$FF = 1 + 2,7 \left( \frac{t}{c} \right) + 100 \left( \frac{t}{c} \right)^4, \quad (5.22)$$

where  $\frac{t}{c}$  is the thickness to chord ratio.

Note that for more complex geometries, the form factor equation can be computed for slices of the wing and fuselage and then summed up to obtain the total friction/-form drag.

The described estimation of the drag has been implemented and added to the induced drag obtained by PanAir. The correction has been plotted in the form of an error bar plot. One can see that the offset becomes non-existent when the angle of attack is equal to zero. As the angle of attack reaches higher values, the drag prediction becomes less accurate.

During the test campaign performed by the NACA on different airfoils, the presence of flaps has also been investigated. The type of flaps investigated are split flaps. Split flaps are surfaces on the lower side of the airfoil that hinge downwards while the rest of the airfoil remains immobile. A schematic representation of a split flap is shown in Figure 5.9. The configuration in which they tested these flaps was on a NACA 0018 wing of aspect ratio equal to six. Split flaps are difficult to implement in PanAir and the correctness of results for this kind of configuration is not guaranteed. Hence, another report published by the NACA was used as comparison, Ames

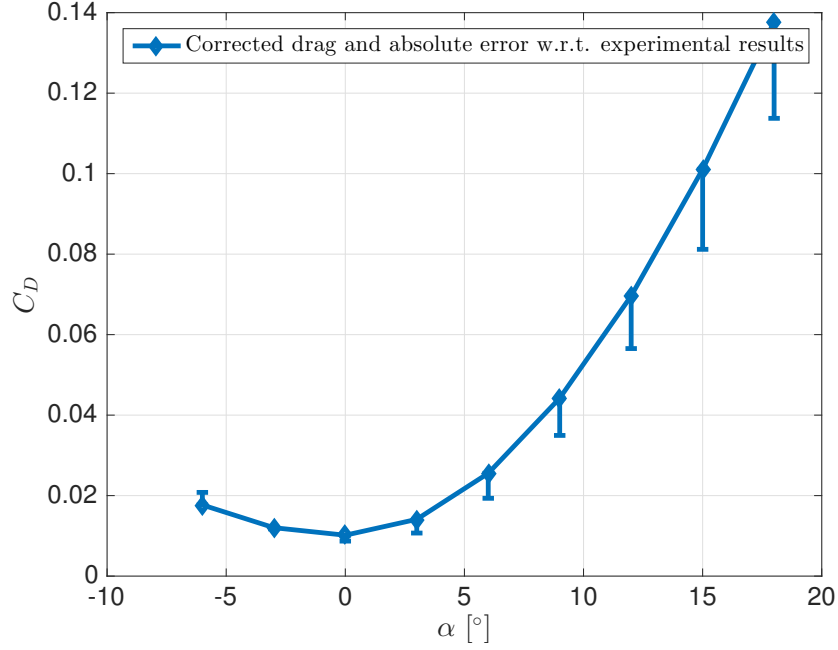


Figure 5.8: Drag coefficient  $C_D$  in function of the angle of attack after correction of the drag to take friction and form drag into account. Errorbars represent the error with the experimental results

[3]. In this report, the influence of both Gwinn and plain flaps is studied in the wind tunnel on a NACA23015. The flaps covered the entirety of the span. The flaps were placed at 25 percent of the chord. The average Reynolds number was equal to 609000. The plain flap configuration was discretized in PanAir according to the previously described medium discretization. The tested deflections were:  $\delta_f = 0^\circ$ ,  $\delta_f = -2^\circ$ ,  $\delta_f = -5^\circ$  and  $\delta_f = -10^\circ$ . The tests were conducted at zero angle of attack.

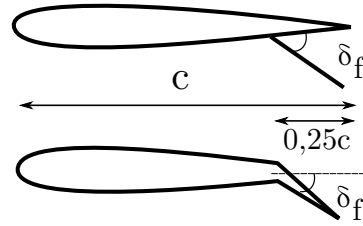


Figure 5.9: Schematic representation of a split flap and a plain flap with deflection  $\delta_f$  as investigated in the report on NACA airfoils, Ames [3]

The results of the comparison for the lift coefficient are shown in Figure 5.10. In this Figure, a zoom has been performed between angles of attack of zero and five. As it has already been showed with the NACA0018, the results when the deflection is equal to zero are very conclusive. For small deflections of the flap ( $\delta_f = -2^\circ$ ), the difference between both methods is still negligible. However, as the deflection of the

flap increases, an offset between both methods is introduced. PanAir overestimates the lift coefficient. At  $\delta_f = -10^\circ$ , the offset is equal to 0.12 and represents a percentage of error of 25 %. To conclude, when introducing flaps in a model, results coming from PanAir should be interpreted carefully and should only be considered for small deflection angles. The study of the flap is a good opportunity to highlight limitations of lower fidelity aerodynamic tools. Their reduced computation time comes at a price.

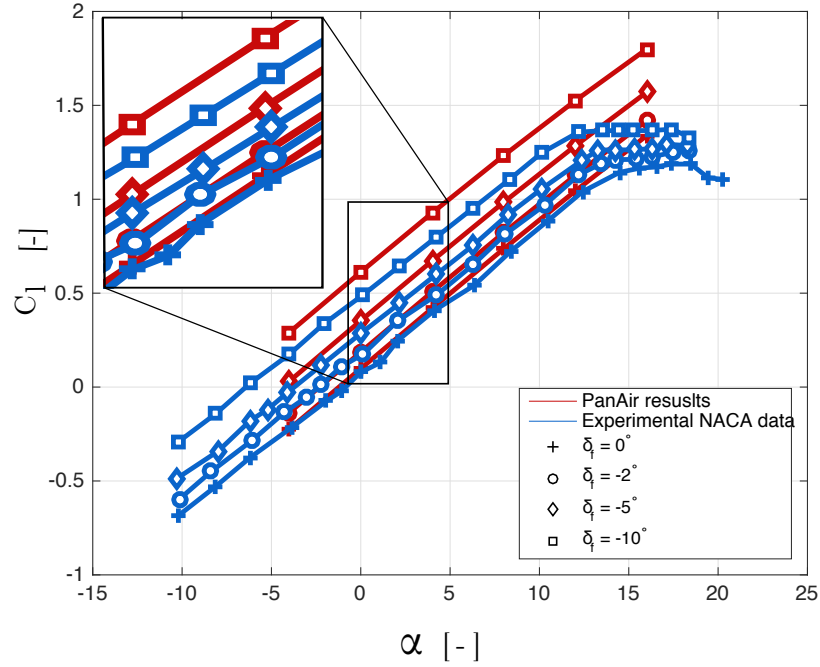


Figure 5.10: Evolution of the lift coefficient  $C_L$  in function of the angle of attack  $\alpha$  for a NACA23015 at zero angle of attack and  $Re = 609000$ . Comparison of the results coming from PanAir and the experimental results by Ames [3] for different angles of flap deflection  $\delta_f$



# Chapter 6

## High fidelity aerodynamic tool

### 6.1 Introduction on SU<sup>2</sup>

The other tool that will be used for analysis of the BWB UAV is a higher fidelity tool. In this case, a full computational fluid dynamics simulation will be performed. The software that will be used, is the Stanford University Unstructured tool suite (SU<sup>2</sup>) [20]. SU<sup>2</sup> is an open-source suite intended for the high-fidelity analysis of partial differential equations systems. The SU<sup>2</sup> suite is composed of multiple modules and handles parallel computing. The majority of simulations will hence be performed on the cluster of the *Consortium des Equipements de Calcul Intensif*, a high-performance computing center involving various universities in Belgium [1].

The objective with the CFD (computational fluid dynamics) simulations of the Guardian Eye 1, is to be as close as possible to the wind tunnel test campaign that was performed at the University of Liège (see Chapter 4). Hence, the choice of model to represent the flow conditions is very important. The assumptions that will be made are that the flow is viscid, incompressible, steady and turbulent.

What follows is a summary of the detailed description of the different SU<sup>2</sup> modules in Palacios [20]. Here, only the relevant modules necessary for the simulation of the GE1 are explained and used to highlight the choices of numerical schemes that have been made.

The equations characterizing the fluid flow, i.e. the continuity equation, the momentum equations and the energy equation can be written under the common form,

$$\partial_t U + \nabla \cdot \vec{F}^c + \nabla \cdot \vec{F}^v = Q, \quad (6.1)$$

in a domain  $\Omega \subset \mathbb{R}^3$  and for  $t > 0$  where  $U$  is the vector of states variable,  $\vec{F}^c(U)$  and  $\vec{F}^v(U)$  are respectively the convective and viscous fluxes and  $Q(U)$  is a source term.

As mentioned earlier, the assumption of incompressibility was made. The numerical method for solving incompressible flows is the one of Alexandre Chorin [8]. His theory, called the artificial compressibility, is based on the introduction of an artificial compressibility  $\delta$  in the equations in such a manner that the final results will not depend on that artificial compressibility. Based on these results, an expression for

the viscous and convective fluxes of the baseline PDE in Equation 6.1 are given by,

$$\vec{F}_i^c(U) = \begin{pmatrix} \beta^2 v_i \\ \rho v_i v_1 + P \delta_{i1} \\ \rho v_i v_2 + P \delta_{i2} \\ \rho v_i v_3 + P \delta_{i3} \end{pmatrix}, \quad \vec{F}_i^v(U) = \mu \begin{pmatrix} \cdot \\ \partial_i v_1 \\ \partial_i v_2 \\ \partial_i v_3 \end{pmatrix}, \quad Q = \begin{pmatrix} \cdot \\ \cdot \\ \cdot \\ -\frac{\rho}{Fr^2} \end{pmatrix}, \quad (6.2)$$

where  $U = (P, \rho v_1, \rho v_2, \rho v_3)$  is the vector containing the states variables,  $\beta^2$  the artificial compressibility,  $Fr$  the Froude number,  $\mu$  the viscosity and  $\delta_{ij}$  the Kronecker symbol. In this case, those are the pressure  $P$  and  $\vec{v} = (v_1, v_2, v_3) \in \mathbb{R}^3$  is the flow velocity in Cartesian coordinates.

The turbulence will be modelled according to the Boussinesq assumption stating that turbulence can be accounted by an increase in viscosity. The viscosity is then decomposed in a part called laminar viscosity  $\mu_{dyn}$  and another called the turbulent viscosity  $\mu_{tur}$ . Note that in Equation 6.2, the viscosity is equal to the total viscosity, that is  $\mu_{tot} = \mu_{dyn} + \mu_{tur}$ . The laminar viscosity is a function of the temperature. The turbulent viscosity is obtained through the chosen turbulence model.

Here, the Spalart-Allmaras (SA) turbulence model was used. In such case, the turbulence or eddy viscosity is given by,

$$\mu_{tur} = \rho \hat{\nu} f_{v1}, \quad (6.3)$$

where  $f_{v1} = \frac{\chi^3}{\chi^3 + c_{v1}^3}$ ,  $\chi = \frac{\hat{\nu}}{\nu}$  and  $\nu = \frac{\mu_{dyn}}{\rho}$ .

The additional variable  $\hat{\nu}$  is obtained through the solution of a transport equation similar to Equation 6.1. For the exact mathematical expressions of the different terms of the transport equation as well as the values of constants in the equation, the reader may consult Spalart [26] at page 21. The boundary conditions for the turbulence transport equation are that  $\hat{\nu}$  is set to zero at walls, representing the absence of turbulent eddies near the surface of the walls, and the imposition of a part of the laminar viscosity (three to five times) to the far field. Hence,

$$\hat{\nu}_{wall} = 0, \quad \hat{\nu}_{far} = 3\nu \text{ or } 5\nu \quad (6.4)$$

For the spatial discretization of the baseline PDE (partial differential equation) in Equation 6.1, a finite volume method is used. The PDE then take the semi-discretized integral form,

$$\int_{\Omega_i} \frac{\partial U}{\partial t} d\Omega + \sum_{j \in \mathcal{N}(i)} (\tilde{F}_{c_{ij}} + \tilde{F}_{v_{ij}}) \Delta S_{ij} - Q | \Omega_i | = \int_{\Omega_i} \frac{\partial U}{\partial t} d\Omega + R_i(U) = 0, \quad (6.5)$$

where  $R_i(U)$  is the residual,  $\tilde{F}_{c_{ij}}$  is the projected numerical approximation of the convective flux,  $\tilde{F}_{v_{ij}}$  is the projected numerical approximation of the viscous flux,  $Q$  is the source term,  $\Delta S_{ij}$  is the area of the face associated with the edge  $ij$ ,  $\Omega_i$  is the volume of the control volume and  $\mathcal{N}(i)$  is the set of neighbouring nodes to node  $i$ .

The convective, viscous fluxes as well as source terms still needs discretization. A Roe numerical scheme is used to discretized the convective fluxes. The Roe numerical scheme computes the convective fluxes based on flow quantities at the interface of the evaluated control volumes. The flow quantities at the interface are reconstructed from the surrounding nodes.

When using a finite volume method, the evaluation of the viscous fluxes requires the knowledge of flow variables and their first derivatives at the cell faces. In SU<sup>2</sup>, the flow variables are averaged at the cell faces. Their gradients can be evaluated either by a Green-Gauss method or a least-squares method at all the grid nodes. They are then averaged to get the gradients at the cell faces. Here, a Green-Gauss method was chosen.

The semi-discretized PDE is evaluated at different steps of the time interval. One can evaluate the residual of the discretized PDE at time  $t^n$  or  $t^{n+1}$  (respectively an explicit and implicit method). Here, the Euler implicit scheme was used. The discretized PDE is approximated by,

$$\int_{\Omega_i} \frac{\partial U}{\partial t} d\Omega + R_i(U) \approx |\Omega_i| \frac{dU_i}{dt} + R_i(U) = 0 \quad (6.6)$$

Implementing the Euler implicit scheme in previous equation, it becomes,

$$\frac{|\Omega_i^n|}{\Delta t_i^n} \Delta U_i^n = -R_i(U^{n+1}), \quad (6.7)$$

where  $\Delta U_i^n = U_i^{n+1} - U_i^n$ .

Of course, the residuals at time  $t^{n+1}$  are unknown. Hence, the residuals  $R(U_i^{n+1})$  are linearized around  $t^n$  through a Taylor expansion. Hence,

$$R_i(U^{n+1}) = R_i(U^n) + \sum_{j \in \mathcal{N}(i)} \frac{\partial R_i(U^n)}{\partial U_j} \Delta U_j^n + \mathcal{O}(\Delta t^2) \quad (6.8)$$

Combining Equations 6.7 and 6.8, the linear system to find the solution update is given by,

$$\left( \frac{|\Omega_i^n|}{\Delta t_i^n} \delta_{ij} + \frac{\partial R_i(U^n)}{\partial U_j} \right) \cdot \Delta U_j^n = -R_i(U^n), \quad (6.9)$$

SU<sup>2</sup> has different linear solvers implementation for solving previous equation. The method that has been used here is the Generalized Minimal Residual method.

## 6.2 Meshing using ANSYS ICEM

Meshing the geometry was done using ANSYS's ICEM meshing tool. The computational domain used for the simulations is a cube. The size of the cube will be studied in a subsequent section. When the angle of sidelsip is zero, the study of the BWB UAV can be done only on a half-span model because of the symmetry. This

will reduce the computation time.

The mesh around the Guardian Eye 1 is an unstructured mesh. To be able to capture the effects of the boundary layer the mesh around the body needs to be extremely fine. The use of an hybrid unstructured mesh is here very appropriate. The mesh will hence consist of a combination of different basic element types.

The elements near the body and situated in the boundary layer will be prisms. They will form a layer around the studied geometry. As the mesh progresses away from the body, the elements used will become tetrahedrons. The use of different types of elements is useful as hexahedrons are more accurate and with less memory requirements than tetrahedron cells. A fully hexahedral mesh is, however, complex to generate, hence the combination with tetrahedrons.

A typical hybrid mesh around an airfoil is represented in Figure 6.1. One can clearly see the layer of prisms supposed to capture the boundary layer profile.

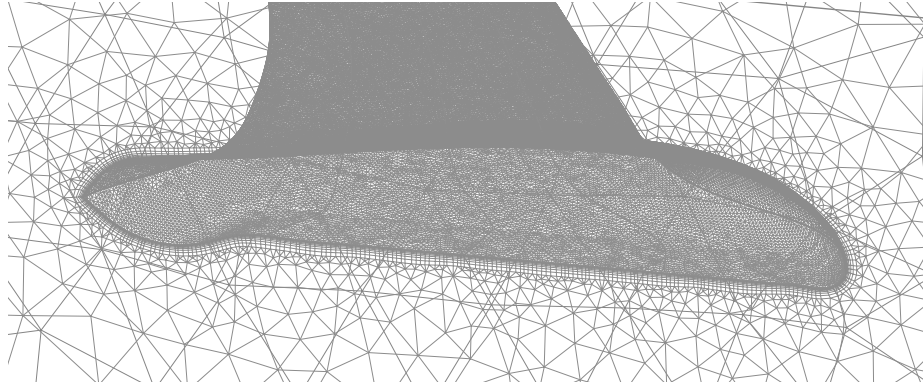


Figure 6.1: Hybrid mesh around the GE1

The height of the first prism layer is of great importance. Indeed, the velocity profile in the boundary layer needs to be determined accurately. This is very important as the gradients in the boundary layer are usually very high. To be able to capture the correct velocity profile in the boundary layer, the height of the first cell needs to be adequate. A first cell's height that is too large will miss the variations of the flow. One way to estimate the correct height is to use the non-dimensional wall distance  $y^+$ . The method relies on the imposition of a  $y^+$  value, a cell height corresponding to that  $y^+$  value is then obtained via formulas. A common practice is to impose a value of  $y^+ = 1$ . To determine the first cell height, firstly, one needs to estimate the skin friction coefficient. Here the Schlichting skin-friction formula is used.

Knowing the skin friction coefficient, the wall shear stress can be computed with,

$$\tau_w = C_f \frac{1}{2} \rho U_\infty^2. \quad (6.10)$$

The friction velocity can then be computed by,

$$u_\star = \sqrt{\frac{\tau_w}{\rho}}, \quad (6.11)$$

and finally, the height of the first cell is obtained by,

$$y = \frac{y^+ \mu}{\rho u_*}, \quad (6.12)$$

where  $y^+$  takes the desired value. This calculation has been done for the Guardian Eye 1 configuration. The size of the first cell is  $1,9 \cdot 10^{-5}$ .

The boundary conditions imposed on the computational domain are the following. For the five faces of the far field, the marker FAR is imposed. If done on the symmetrical part, the symmetry condition can be taken into account by the marker SYM imposed on the face splitting the aircraft at half span. Finally, the no-slip condition on the body is imposed by the marker HEATFLLUX. This condition, called the *constant heat flux wall* represents the no-slip condition by imposing a constant heat flux of  $0 \text{ J/m}^2$  on the body. Two meshes will be constructed, one around a wing composed of NACA 0012 airfoil profiles and one around the GE1 geometry. (Additionally, one full size and one semi-symmetrical mesh of the GE1 will be performed).

A schematic representation of the computational domain is presented in Figure 6.2. Scales are not respected for ease of representation. In reality, as  $n$  often takes values from 50 to 100, the scale of a cube's side is way bigger than the scale of the geometry. Also, the figure only represents one half of the GE1.

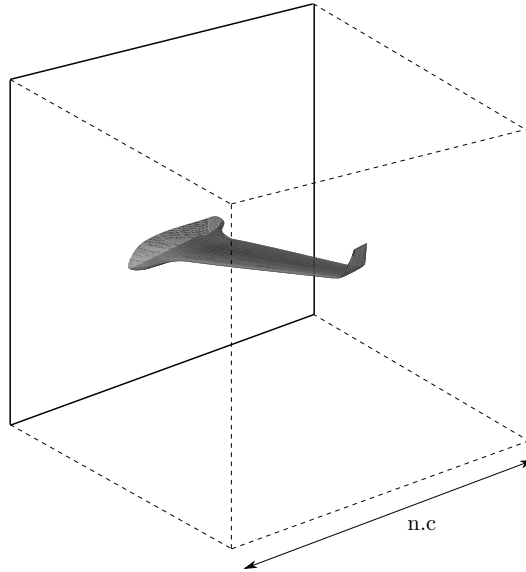


Figure 6.2: Schematic representation of the computational domain of a half GE1 where the dotted edges belong to faces on which a far field condition is imposed and the face whose edges are plain lines is a face on which a symmetry condition is imposed. The UAV is represented by the gray body. The side of the cube is equal to  $n$  time the largest chord  $c$  of the body

### 6.3 Convergence analysis on the size of cells and domain

Similarly to what has been done for the number of panels for the analysis of PanAir, a convergence analysis has to be performed for the mesh that will be used for the CFD analysis. The convergence analysis will be performed on the NACA 0018 wing.

Convergence is first verified for a fixed computational domain size. This cube size is fixed at five times the root chord. The total number of cells will be increased by decreasing the cell size. Tests are performed at zero angle of attack and for a Reynolds number of  $3.4 \times 10^6$ . For the sake of computational time, the convergence is analysed on half a wing. Results for the drag coefficient are shown in Figure 6.3.

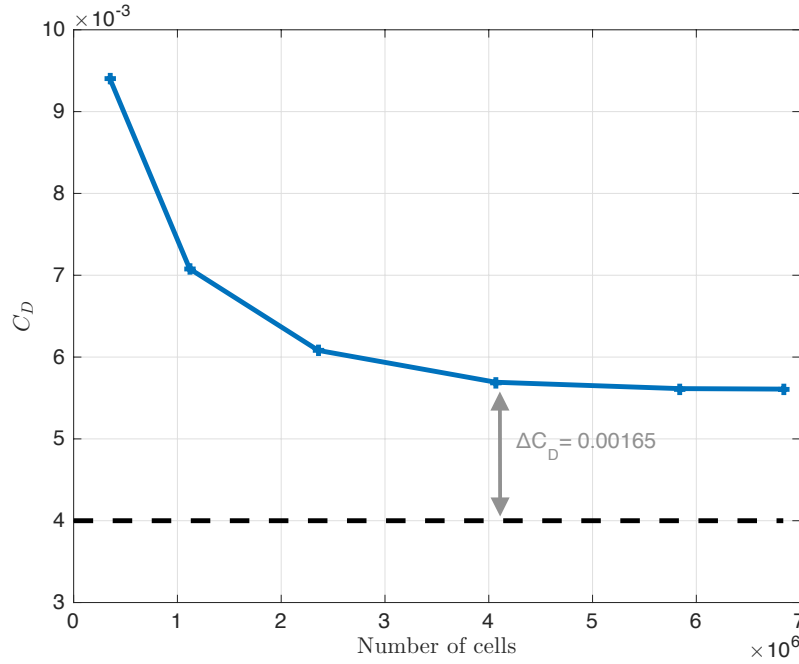


Figure 6.3: Drag coefficient  $C_D$  in function of the number cells in the computational domain. The dashed line represents the exact value of drag obtained by experimentation in Goett [12]

It can be observed that from a number of cells equal to 4 million, the drag has converged to a finite value. The addition of cells does not lead to a significant improvement of the value of the drag. This converged value is compared to the value of drag obtained through wind tunnel testing in the NACA report by Goett [12], that is a  $C_D = 0.004$  for a half-wing. It can be observed that the converged value of the drag obtained through CFD analysis is not equal to the experimental one. This suggest that the size of the domain is not adapted for the simulation. Consequently, the size of the domain will be increased. Further decrease of cell size does not lead to an improvement of the estimated drag. In conclusion, the final size of the cells on the body is equal to 2.5 mm.

Once the size of the cells has been determined, the size of the computational domain has, in turn, to be determined. For this matter, the conditions of the test remain the same as for the convergence of number of cells. The computational cube's size is varied from five to 140 times the chord of the wing. Results are shown in Figure 6.4.

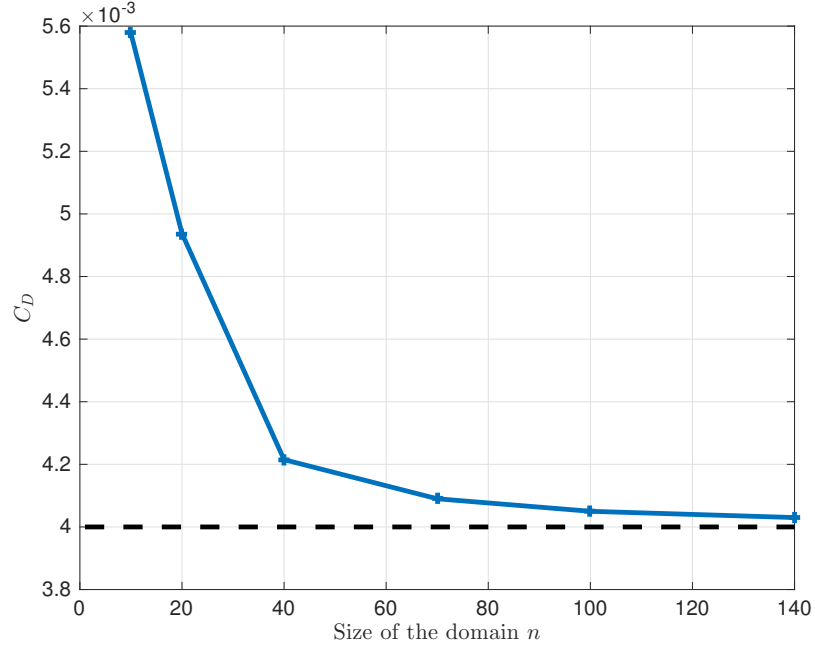


Figure 6.4: Drag coefficient  $C_D$  in function of the computational cube's size, here varying from five to 140 times the chord at half span, the multiplication factor is noted  $n$ . The dashed line represents the exact value of drag obtained by experimentation in Goett [12]

Here too, results converged rapidly. Differences between a cube size of 100 and 140 times the chord at half span are negligible. It can be observed that the converged value of drag obtained through CFD is equal to the one obtained by experiment. The final computational domain size is finally chosen to be a cube whose size is equal to 100 times the chord at half span.

## 6.4 Validation of SU<sup>2</sup>

In order to validate results coming from SU<sup>2</sup>, a similar approach to what has been done for PanAir will be followed. That is, the comparison of results obtained through SU<sup>2</sup> with the experimental ones. The experimental set of results will be the same than the one that was used for the PanAir validation, the study of a wing composed of a NACA 0018 profile of aspect ratio equal to six.

The lift and drag coefficient will be investigated. During the PanAir validation, it has been shown that coefficients obtained through that program for wings with flaps can be trusted to a certain point. At a deflection angle equal to  $\delta_f = -10^\circ$ ,

the results were already off by some margin (offset  $\Delta C_L = 0.2$ ) making them not trustworthy for the analysis of flaps on the geometry. With the CFD analysis, it will be investigated if better results can be obtained with flaps.

The lift coefficient is reported in Figure 6.5 in function of the angle of attack. It can be observed that results coming from SU<sup>2</sup> are very close to the experimental results. With PanAir, the lift curve slope was shown to be larger than the experimental results. Here, the slopes are identical. Small differences, however, can be observed around an angle of attack of 17° where the stall occurs. When the stall occurs, CFD results are slightly underestimated by an amount of 0.1 on average.

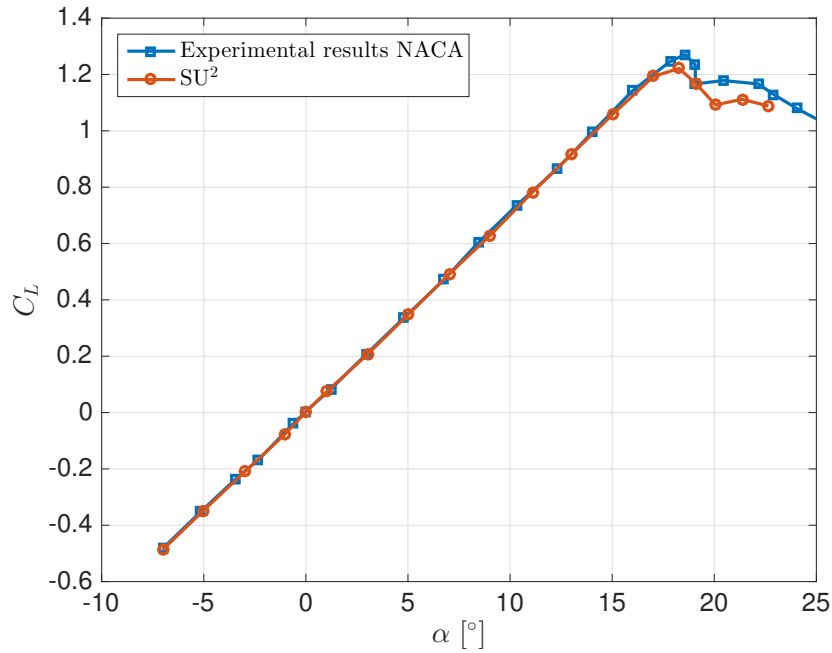


Figure 6.5: Lift coefficient  $C_L$  in function of the angle of attack  $\alpha$  for a NACA 0018 wing of aspect ratio equal to six

The same comparison can be made about the drag coefficient. In Figure 6.6 the drag coefficient  $C_D$  is reported in function of the angle of attack  $\alpha$ . It is further noted that the quality of results from SU<sup>2</sup> are again superior to the ones of PanAir. Of course, here there is no need to correct the value of drag. The relative error with experimental results does not exceed 5%.

Finally, the same flap configuration than one for the PanAir validation has been performed. The acquisition of a good quality mesh was more complicated with the presence of flaps. Indeed, stair stepping of the prism layer appeared (see Figure 6.7). After tweaking of the prism parameters, a good quality prism layer was computed by generating a thick prism layer around the body (composed of only one layer of prism) and then splitting the thick prism layer into smaller ones with the mesh splitting tool. Results for the lift coefficient for the different flap deflection are shown in Figure 6.8. A zoom has been performed for angles of attack between  $-3$  and  $3^\circ$ . SU<sup>2</sup> results are, again, shown to be much more consistent with the experimental.



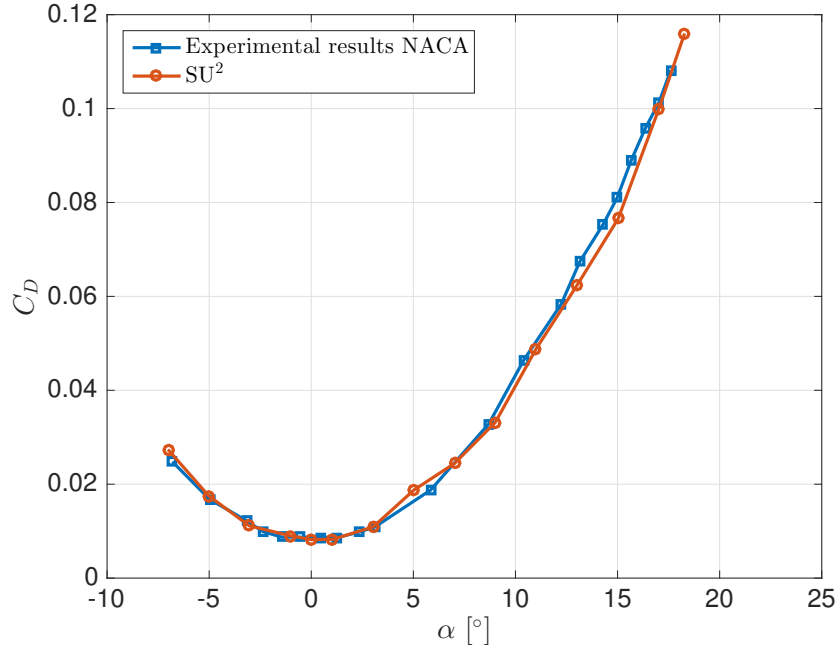


Figure 6.6: Drag coefficient  $C_D$  in function of the angle of attack  $\alpha$  for a NACA 0018 wing of aspect ratio equal to six

Where, the PanAir method predicted a lift coefficient with a relative error of 25% for a deflection angle of  $10^\circ$ ,  $SU^2$  represents it with a relative error that does not exceed 5%.

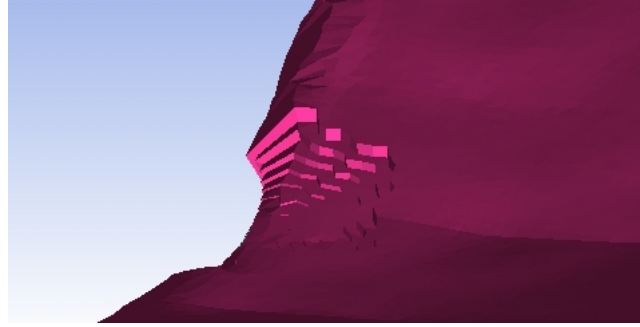


Figure 6.7: Illustration of stairstepping of the prism layer at the trailing edge

## 6.5 Summary

To summarize, PanAir results showed to be accurate to a certain extent. The correction of the induced drag allows to take form and friction drag into consideration even for a potential flow. When the deflection of flaps became too important, PanAir results were not to be trusted anymore and  $SU^2$  should rather be used.

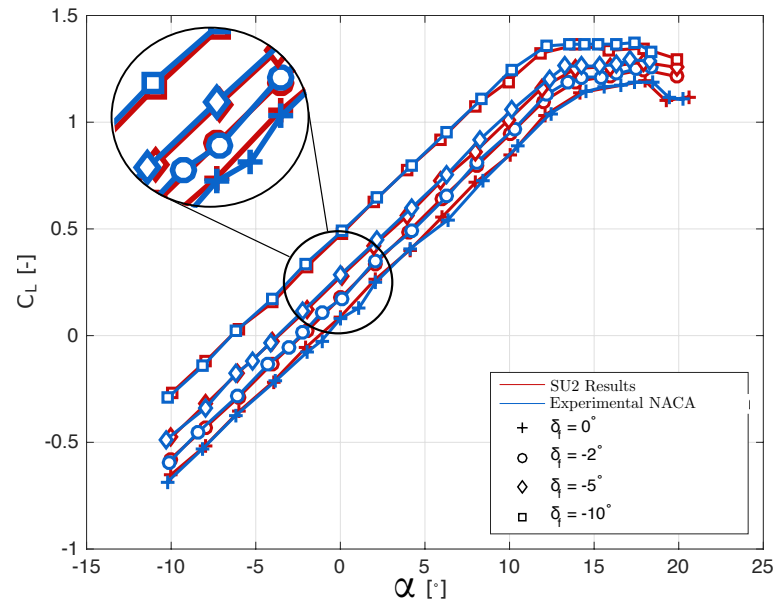


Figure 6.8: Evolution of the lift coefficient  $C_L$  in function of the angle of attack  $\alpha$  for a NACA23015 at zero angle of attack and  $Re = 609000$ . Comparison of the results coming from SU<sup>2</sup> and the experimental results by Ames [3] for different angles of flap deflection  $\delta_f$

# Chapter 7

## Aerodynamic properties of the baseline geometry

In this section, the aerodynamic properties of the baseline geometry will be discussed. For this purpose the simulation results from the low and higher fidelity tools will be studied next to the experimental ones from the previous test campaign performed in the wind tunnel of the University of Liège. Lastly, to ensure that the simulations performed during this master thesis are inline with the works of others, they will be compared the analysis of Lehmkuehler [14]. In 2009, Lehmkuehler studied the aerodynamic performances of a BWB at similar freestream velocity as the GE1 (20 m/s). He performed PanAir tests as well as wind tunnel tests. The geometry of this BWB being slightly different than the GE1, results of the GE1 are not expected to match those from Lehmkuehler exactly. However, it provides a good starting point for the assessment of the aerodynamic performance.

### 7.1 Geometry discretization for the baseline Guardian Eye model

The choice of discretization of the entire UAV geometry will be similar to what has been done for the NACA wing. Namely, a discretization giving a relatively low computation time yet correct results.

The number of chordwise panels will be kept at 80 as in the medium discretization that has been described for the classical (understand NACA) wings. The number of spanwise panels will be determined by analysis of the induced drag as it can be seen in Figure 7.1. It can be observed that a number of spanwise panel of 35 offers a good estimation of the induced drag.

The chosen discretization will thus be 80 panels chordwise and 35 panels spanwise. Computation time for the different discretizations are not represented graphically. However, computation time has been investigated and it appears it grows exponentially when the number of panels is increased. Compared to a number of spanwise panels of 45 or 55, this choice of discretization is a good trade off between a relatively low computation time and accurate results. The representation of this discretization

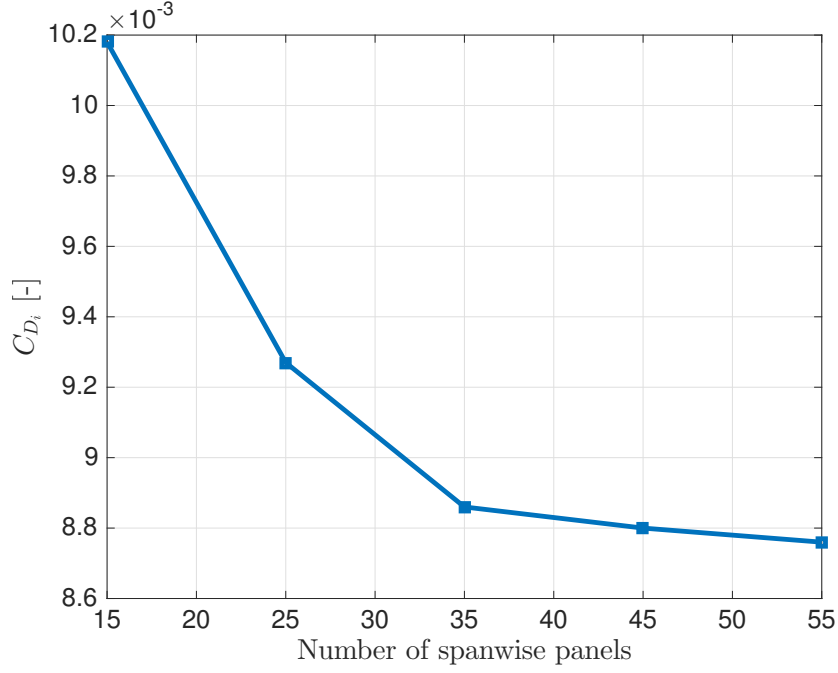


Figure 7.1: Induced drag  $C_{D_i}$  in function of the number of spanwise panels for the baseline GE1 configuration at a freestream velocity of 18 m/s and an angle of attack of  $2^\circ$

is represented schematically in Figure 7.2.

## 7.2 Lift coefficient versus angle of attack

Here, the lift coefficient will be displayed in function of the angle of attack. The results coming from PanAir, the results from the CFD simulation as well as the results from Lehmkuehler will be displayed. They are presented in Figure 7.3.

To be precise, results for cruise speeds of 12.8 and 18 m/s corresponding to both configurations, that is the electrical powered UAV and the one powered by a piston engine, should be displayed. However, the maximum relative error between both cruise speeds is equal to 0.04 %. Hence, from here on, only the results for a freestream velocity equal to 18 m/s will be shown.

In Figure 7.3, it can be observed that the CFD results and PanAir results closely match. The slopes are slightly different however. The lift coefficient slope for PanAir is equal to  $4.0121/rad$  whereas the lift coefficient slope for the CFD analysis is equal to  $3.8093/rad$ . The slightly lower lift coefficient slope has already been observed when studying the NACA wing during the validation of PanAir in Section 5.4.

The results coming from the work of Lehmkuehler are also closely related the ones obtained for the GE1 configuration. The slope of the lift coefficient is, in this case,

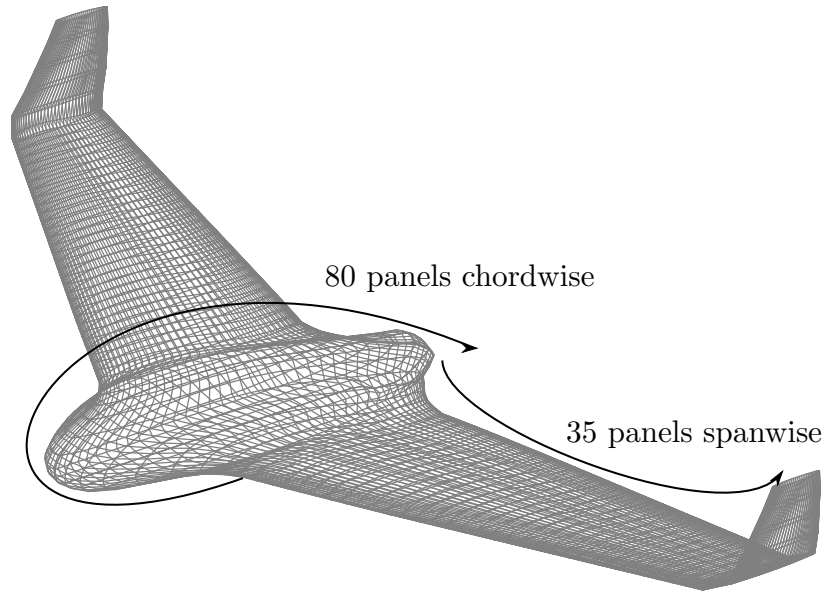


Figure 7.2: Schematic representation of the chosen discretization for the GE1

equal to  $4.15/rad$ . This gives confidence in, both, the results obtained by PanAir and the CFD analysis.

A slight decrease in the lift coefficient for the CFD results at an angle of attack of  $16^\circ$  suggest the stall phenomenon. Note, that this decrease occurs at a slightly smaller angle of attack for the model studied by Lehmkuehler, i.e. at  $14^\circ$ .

A surprising feature is the offset for lift coefficients coming from the wind tunnel test campaign. It appears geometry differences are present between the model tested in the wind tunnel in November 2014 and the one provided in CAD files. After investigation, the model represented in CAD files does not incorporate the camera surveillance module. The underside of the UAV in CAD files is flat whereas the tested model in the wind tunnel had a curved belly. One could assume that the differences in slope between those experimental results and the numerical ones are due to these geometry changes. Future investigations might determine the influence this variation of shape has on the performances and also to what extent does the deployment of the camera influence the performance of the aircraft.

### 7.3 Drag coefficient versus angle of attack

Here, the drag coefficient will be displayed in function of the angle of attack. The results coming from PanAir, the results from the CFD simulation as well as the results from Lehmkuehler will be displayed. They are presented in Figure 7.4.

The results from PanAir have been corrected according to the previously described method to take the friction and form drag into account. This correction enables the results coming from PanAir to match the CFD results reasonably well. There

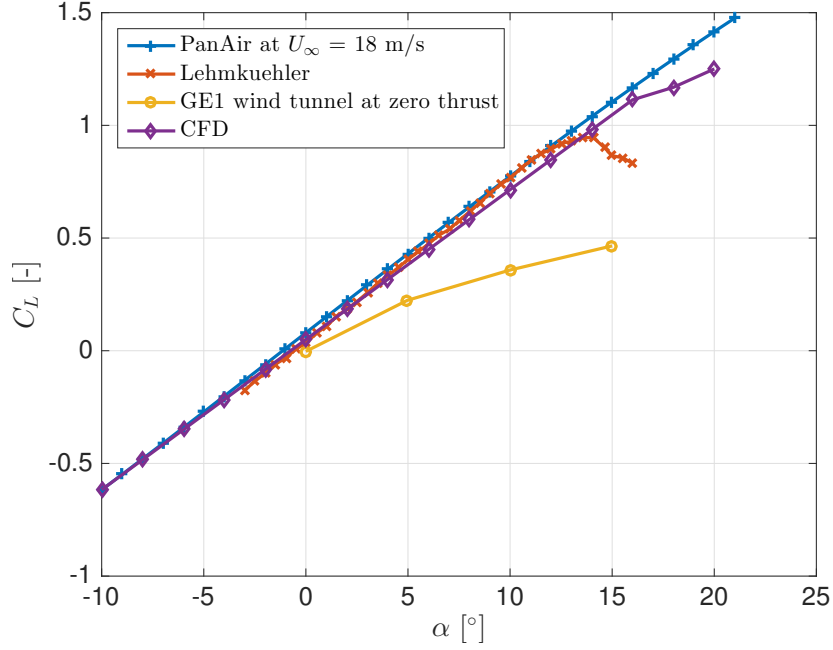


Figure 7.3: Lift coefficient  $C_L$  in function of the angle of attack  $\alpha$  for the GE1 BWB UAV for different analysis methods

subsists a small offset whose average value is equal to 0.007. PanAir results are thus a slight underestimation of the CFD results. The maximum absolute error is 0.02. The minimum drag coefficient according to the CFD analysis is equal to  $C_{D_{min}} = 0.02$  at an angle of attack equal to  $0^\circ$ .

To reinforce confidence in the PanAir and CFD results, they are, once again, compared to results coming from Lehmkuehler. The  $C_{D_{min}}$  is here equal to 0.014.

For similar reasons, namely the geometry changes performed on the prototype between November 2014 and the time of scanning, results from the wind tunnel test campaign are a bit offsetted. The absolute error on the value of drag at zero angle of attack is only of 0.008, however the shape and tendency of the drag curve are significantly different.

## 7.4 Pitching moment versus angle of attack

Here, the pitching moment coefficient will be displayed in function of the angle of attack. The results coming from PanAir, the results from the CFD simulation as well as the results from Lehmkuehler will be displayed. The results are presented in Figure 7.5. The reference point for the measurement of the pitching moment is the nose of the BWB.

When comparing the PanAir and CFD results, an angle of attack interval exists between  $-5^\circ$  and  $5^\circ$  where the relative error is less or equal to 2%. Outside this interval, maximum difference in pitching moment of 0.19 can be reached. Results outside this interval coming from PanAir will thus have to be used carefully. The

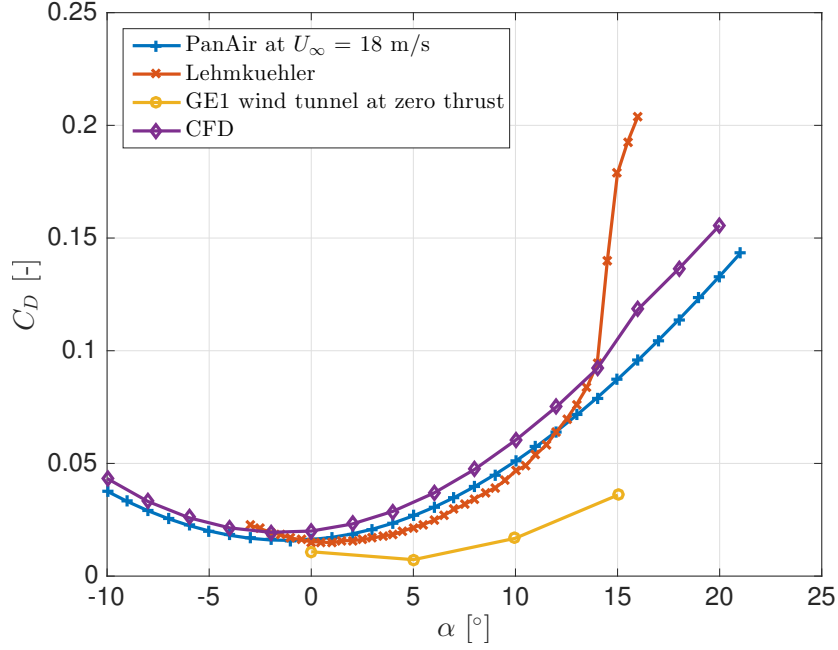


Figure 7.4: Drag coefficient  $C_L$  in function of the angle of attack  $\alpha$  for the GE1 BWB UAV for different analysis methods

tendency of the pitching moment curve whose slope is negative indicates the longitudinal stability of the BWB. Observing if the pitching moment curve's slope is still negative for the improved GE+ geometry will be interesting. It will give a first indicator of the BWB's longitudinal stability.

No comparison with the wind tunnel test campaign has been made for the pitching moment coefficient as this coefficient has not been studied during that test campaign. A future wind tunnel test campaign could incorporate this coefficient.

Note that the influence of the deployment of the camera surveillance module has not been studied in this thesis. Though, the displacement of internal parts and the addition of drag to the camera lens should have a significant influence on the pitching moment.

## 7.5 Lift to drag ratio versus angle of attack

Here, the lift to drag ratio will be displayed in function of the angle of attack. The results coming from PanAir, the ones from the CFD simulation, the ones from Lehmkuehler as well as the lift to drag ratio from the wind tunnel test campaign will be displayed. The results are presented in Figure 7.6.

As mentioned in the introduction on blended wing bodies, the lift to drag ratio is very important when assessing performance of an aircraft. When designing an aircraft, one wants to maximise the lift to drag ratio.

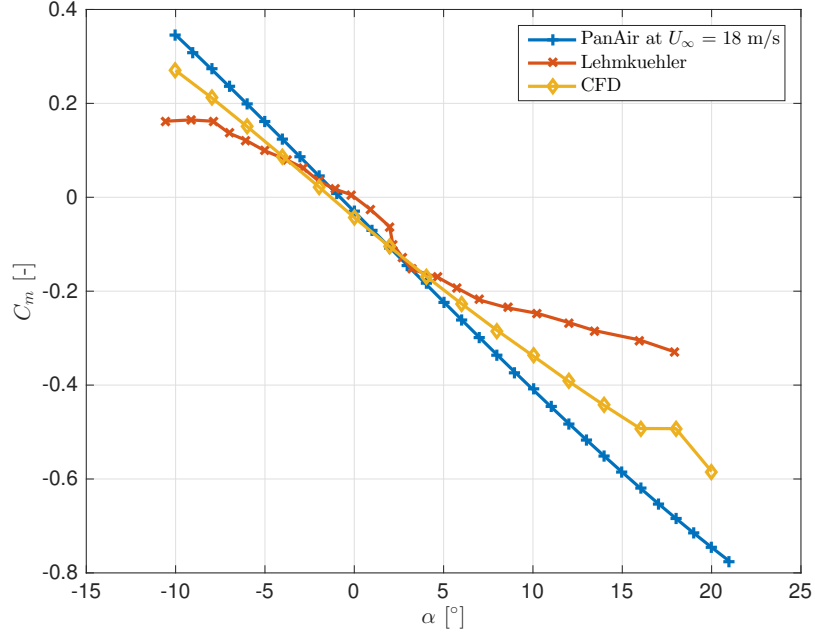


Figure 7.5: Pitching moment coefficient  $C_m$  in function of the angle of attack  $\alpha$  for the GE1 BWB UAV for different analysis methods

In previous sections, small differences in lift and drag coefficients have been highlighted. It is clear that those slight offsets or differences will have an impact on the lift to drag ratio. Here, it can be observed that PanAir overestimates the lift to drag ratio. This could be due to different factors. The first one being an intrinsic error of the panel method theory. Indeed, the lift was a bit overestimated by PanAir while the drag, however, was underestimated. The other one being the fact that the value of drag is based on a correction performed on the value of induced drag. An inaccuracy in the method of estimation of this value could thus lead to erroneous results. Concerning the CFD results, the maximum lift to drag ratio is observed at an angle of attack of six degrees and is equal to 12.94. This defines the optimal flying condition.

Results from Lehmkuehler reach a maximum  $L/D$  at the same angle of attack as the GE1 (i.e.  $AOA = 6^\circ$ ). However, the value of maximum  $L/D$  is equal to 18.

Experimental results were also plotted, however, it was shown that the lift and drag values obtained experimentally showed differences with respect to numerical ones. It is thus logical to observe, here too, that the experimental lift to drag ratio does not match the numerical ones.

## 7.6 Influence of sideslip

During a steady rectilinear flight, the longitudinal axis of the aircraft is usually positioned parallelly to the uniform flow. Yet, this is not the case in various flight conditions, for instance flying with crosswind, turns, etc. It would therefore be use-



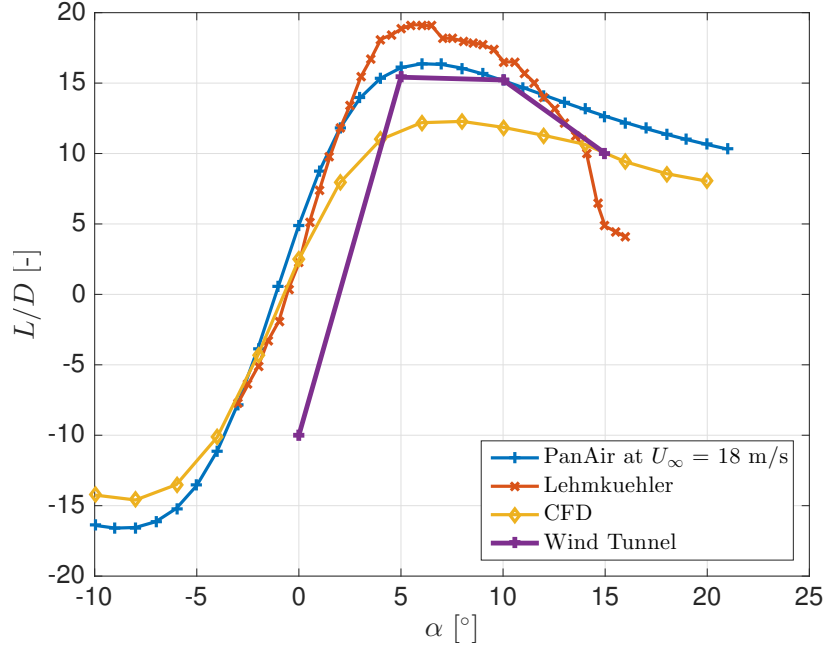


Figure 7.6: Lift to drag ratio  $L/D$  in function of the angle of attack  $\alpha$  for the GE1 BWB UAV for different analysis methods

ful to know how the aerodynamic coefficients evolve with the presence of sideslip angle.

The presence of sideslip angle has been included in both the PanAir and CFD models. Note that the simulations of sideslip have been performed on the full geometry (and not only a half span symmetrical model) for both methods. Fuselages of conventional aircraft are slender bodies whose shapes are usually aerodynamically shaped cylinders. However when flown sideways, those designs of fuselage cause an import interference wake and disturb the flow around the wing. For conventional aircraft, it is thus expected that the lift coefficient will decrease as the sideslip angle grows because of this interference. Simulations have been performed at a free stream velocity of 18  $m/s$  and at an AOA of  $2^\circ$ . The sideslip angle has been varied from  $0^\circ$  to  $12^\circ$  with incremental steps of  $2^\circ$ . Results are shown in Figure 7.7.

Surprisingly, as the sideslip angle increases the lift coefficient slightly increases. This highlight another advantage of BWB. Indeed, the BWB is capable of maintaining the lift generation constant (here slightly increasing) even with the presence of crosswind. The smooth transition between fuselage and wing allow for such a phenomenon. The lift seems, however, to decrease passed an angle of sideslip equal to eight degrees. This graph will be compared to the influence of sideslip angle for the enhanced geometry GE+ to see if this decrease in lift can be delayed to higher values of sideslip angles.

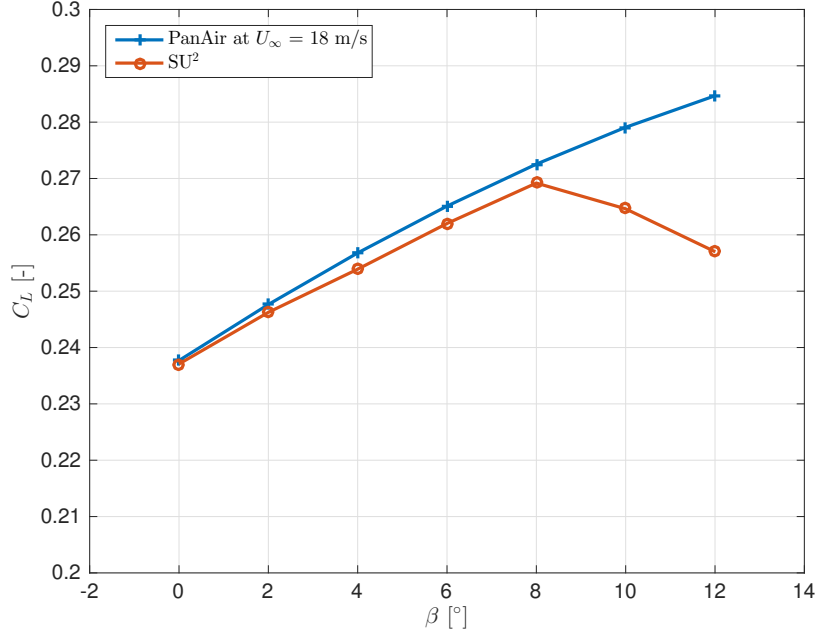


Figure 7.7: Lift coefficient  $C_L$  in function of the sideslip angle  $\beta$  for the GE1 when  $U_\infty = 18$  m/s and the  $AOA = 2^\circ$

## 7.7 Influence of the control surfaces

When it comes to control surfaces, the number of possible combination of deflection angles, antisymmetric deflected flaps, etc. is huge. The analysis of the behaviour of the aircraft when control surfaces are deflected could justify another technical report on its own. Here, the results will only scratch the surface as only the lift coefficient when control surfaces are symmetrically deflected will be studied.

The control surfaces are positioned at a distance of 490 mm from the middle of the BWB in the spanwise direction. Their dimensions and shape are given in the schematical representation of Figure 7.8.

The evolution of the lift coefficient is shown in Figure 7.9. The successive increments  $\Delta C_L$  for deflection angles of  $2^\circ$ ,  $5^\circ$  and  $10^\circ$  are respectively 0.1134, 0.0934 and 0.1973.

## 7.8 Influence of the propulsion

When the propeller operates at full thrust, it will inevitably have an influence on the flow around the GE1. To what extent does the propeller affects the performance of the BWB is a question that needs to be answered. To do that, a usual technique is to add the actuator disk theory to the CFD simulation. The boundary condition *actuator disk* exists and is implemented in SU<sup>2</sup>. For an undetermined reason, simulations immediately diverged when attempts to launch the simulation were performed. Hence, results from CFD were not acquired.

PanAir, however, includes a boundary condition that is able to model a fan face.

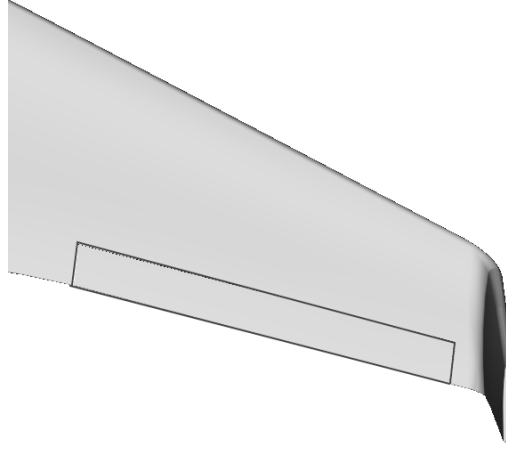


Figure 7.8: Schematic representation of the shape and size of the control surface on the GE1

The user then has to provide as additional input the mass flux at the panel center.

The propeller has been modelled by an seven inches disk (17 cm) placed at the back of the BWB. The determination of the mass flux that had to be imposed on the disk has been determined by application of the integral momentum theorem. The propulsive efficiency of a propeller is given by,

$$\eta_{prop} = \frac{2}{1 + \frac{u_e}{u_0}}, \quad (7.1)$$

where  $u_e$  is the speed of the flow ejected by the propeller and  $u_0$  is the free stream velocity. Furthermore, the thrust is given by,

$$T = \dot{m}(u_e - u_0), \quad (7.2)$$

where  $\dot{m}$  is the mass flux through the propeller. Combining Equations 7.1 and 7.2, it becomes,

$$\eta_{prop} = \frac{2}{2 + \frac{T}{u_0 \dot{m}}} \quad (7.3)$$

In last equation, all variables are known. Indeed, the free stream velocity is known, the required thrust has been estimated in the technical report of the wind tunnel tests. The propulsive efficiency of a typical well designed seven inches propeller is 0.79 (according to APC Propellers' data sheets). The fact that the propeller is placed at the back of the BWB will reduce its efficiency. In fact, the body of the BWB disturbs the flow impinging on the propeller. The reduction of efficiency due to the body is difficult to assess, however it is of common practice to account for a 0.3 reduction of efficiency.

The lift coefficient in function of the angle of attack for both engine modes (zero and full thrust) is reported in Figure 7.10. During the wind tunnel test campaign, it was shown that the lift coefficient was not much affected by the slipstream of the

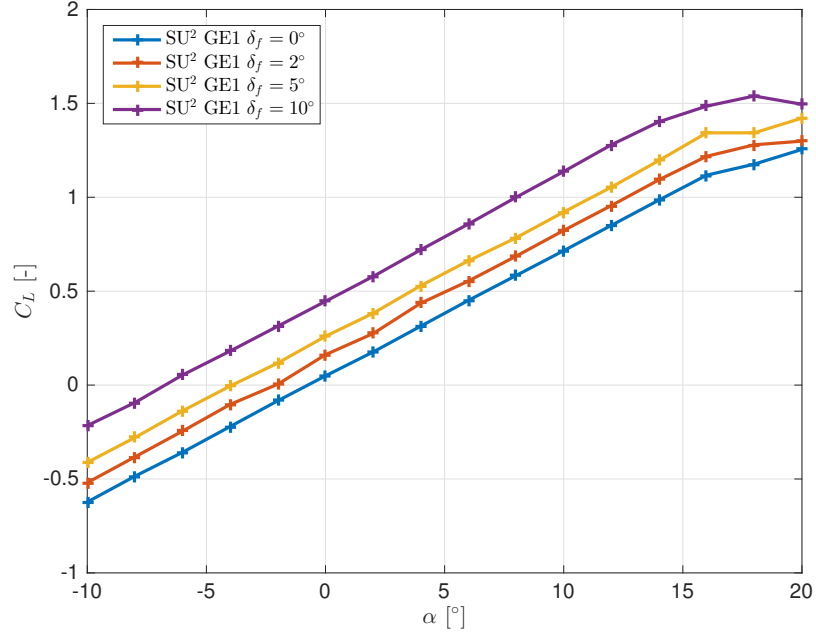


Figure 7.9: Evolution of the lift coefficient  $C_L$  in function of the angle of attack  $\alpha$  for the GE1 for different angles of flap deflection  $\delta_f$

propeller. From the results of PanAir, it is observed that this phenomenon is still observed. Indeed, even if the slope of lift curve is slightly larger when the thrust is at full regime, the maximum relative error that has been observed between both engine modes is less or equal to 6%.

For the drag however, a significant change had been observed during the wind tunnel test campaign. Namely, the drag became negative (which is the sought objective) as it was shifted by a  $\Delta C_D$  of 0.05 downwards. The results for the drag obtained by PanAir are represented in Figure 7.11. Here too, the drag was shifted downwards, this time by a  $\Delta C_D$  of 0.04 on averaged.

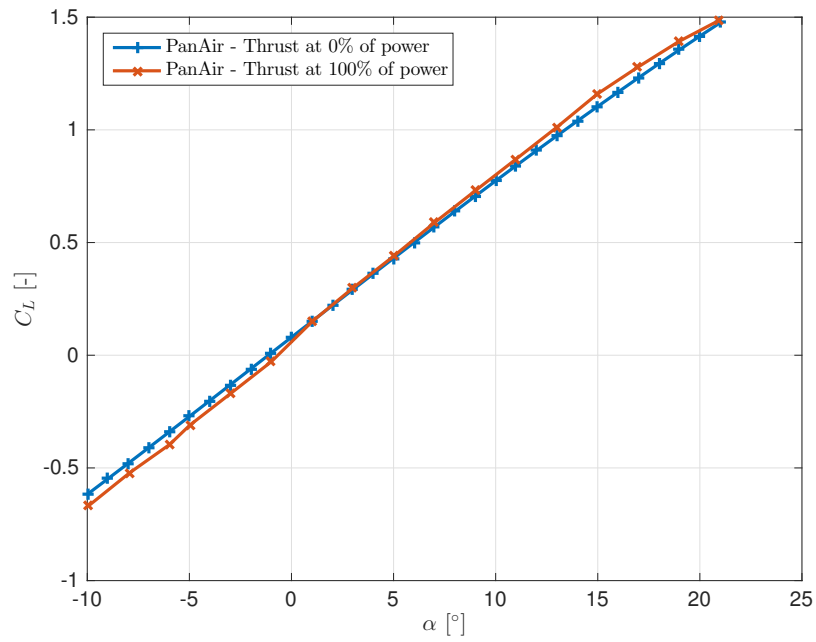


Figure 7.10: Lift coefficient  $C_L$  in function of the angle of attack  $\alpha$  for both engine modes (zero and full thrust) for the GE1

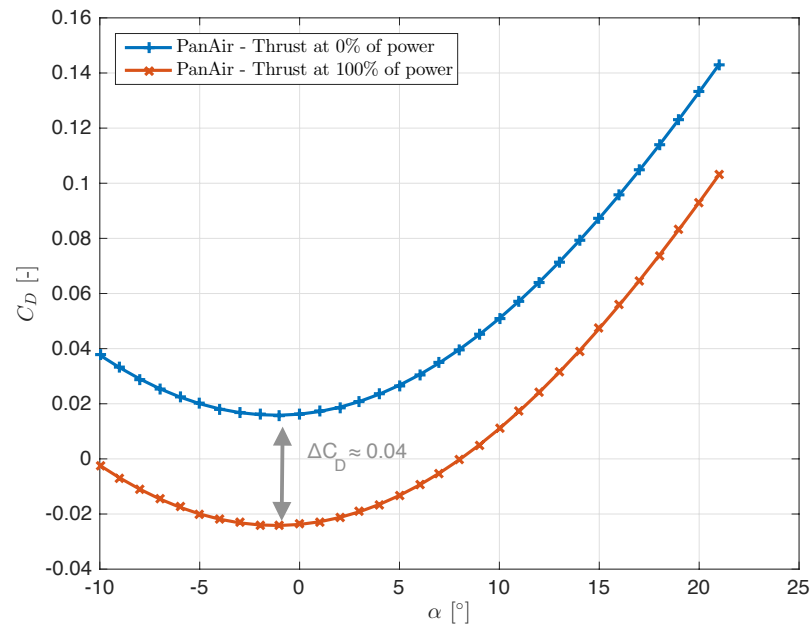


Figure 7.11: Drag coefficient  $C_D$  in function of the angle of attack  $\alpha$  for both engine modes (zero and full thrust) for the GE1

# Part III

## Aerodynamic study

Having studied the aerodynamic properties of the baseline design, this part will examine the potential geometry changes in order to enhance the performance of the BWB UAV.

First, a set of parameters will be proposed. An objective function will then be maximised, the combination of parameters that maximises the objective function will define the new geometry. In an additional step, it will be verified that the new configuration meets the minimum lift requirement.

The objective function will be the lift to drag ratio  $L/D$ . The drag will encompass the induced drag as well as the friction and form drag. The optimization will be done on PanAir, indeed the acquisition of results is faster. As a high number of parameter combinations will be tested, this speed of acquisition is essential. For the estimation of the drag, the method that has been described previously will be used.

# Chapter 8

## Choice of parameters

The number of variable parameters is significant. Hence, a selection of the ones that have an influence on the objective function will be retained.

When discussing the different parameters, a differentiation can be made between the fuselage, the wing and the winglets. For the fuselage, not a lot of variation is possible. Indeed, the fuselage has to carry the payload. The arrangement of the internal components does not leave much for geometry modifications neither. Hence, the thickness of the fuselage will be considered as a manufacturing constraint. The only parameter of the fuselage that will be studied is the length. Therefore, it will be investigated whether the length has an influence on the objective function and hence, whether it should be part of the set of parameters.

In Figure 8.1, the length of the fuselage has been modified. It was increased by respectively, 5, 10, 15 and 20 *cm*. The changes of the ratio between the lift coefficient and the lift-induced drag are plotted in function of these different fuselage lengths. To be exact, the ratio that should be studied is the lift to total drag ratio. However, the increase of fuselage length will inevitably lead to an increase of friction drag making the UAV less performant. The study of the lift to induced drag ratio is here sufficient.

It can be observed that this ratio is kept bounded between values of 43 and 44. Variations are thus small and the assumption that the length of the fuselage does not significantly influence the performances of the UAV will be made. This parameter is therefore eliminated from the set of parameters. As a consequence, the whole fuselage is left unchanged and is considered fixed by the internal arrangement.

For the wing, the different parameters that can be varied are the root chord, the sweep angle and the taper ration. In the same spirit as the constraints arising from payload carriage, it was decided to keep the chord root fixed since the fuselage is considered fixed. The span of the wing will be kept constant.

The winglets are very important in the increase of performance. For finite wings a major source of loss of performance is attributed to the wing tip vortices. By adding winglets, the loss of energy due to these vortices is reduced. In fact, winglets increase the effective aspect ratio of the wing. The wing's characteristics then move



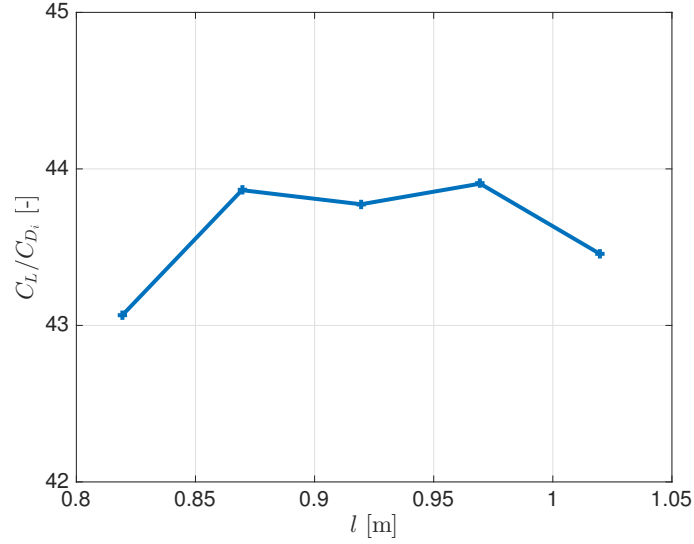


Figure 8.1: Ratio of the lift coefficient over the lift-induced drag  $C_L/C_{D_i}$  in function of the length of the fuselage  $l$

towards the ones from an infinite wing. The lift induced drag then decreases.

One might be tempted to increase the size of winglets significantly. However, this increase comes at a cost. While reducing the lift induced drag, the increase in size of a winglet leads to the increase of parasite drag. Its design is therefore a trade-off and needs to be adequately done.

In the case of the UAV, the geometry parameters of the winglets are the root chord, the sweep angle, the taper ratio and height.

To highlight the importance of winglets, two cases have been launched with PanAir. One geometry comprised of the baseline configuration with winglets and another without winglets. Both cases were launched for an angle of attack of  $2^\circ$  and for a freestream velocity equal to the cruise speed of the electrical version of the UAV. The lift to induced drag ratio went from 43 for the geometry with winglets to 37 for the geometry without winglets.

# Chapter 9

## Parametric study

First, the influence of every parameter on the objective function will be studied and discussed separately. From this study, a range of variation will be proposed for the parameter in question.

### 9.1 Taper ratio of the wing $\lambda_w$

The taper ratio of a wing is given by,

$$\lambda_w = \frac{C_t}{C_r}, \quad (9.1)$$

where  $C_t$  is the chord at the tip and  $C_r$  is the root chord.

Here, the root chord is considered a manufacturing constraint and can thus not be changed. Changing the taper ratio of the wing will thus play a role on the chord at the tip. The taper ratio of the baseline geometry is equal to 0.4416. When varying the taper ratio, one has to verify that the surface of the wing is able to produce the sufficient amount of lift as to maintain flight. In other words, reducing the taper ratio is possible only to a certain point. In Figure 9.1, the lift to drag ratio is represented in function of the taper ratio of the wing. The extreme when  $\lambda_w = 0$  is excluded.

The lift to drag ratio shows a maximum for a taper ratio equal to 0.4416 (the default value). It can be observed that passed a value of 0.8, it becomes smaller than for any other value of the taper ratio. There is thus no interest in having a taper ratio higher than 0.8. The upper bound for this parameter will thus be 0.8.

In Figure 9.2, the lift coefficient is represented in function of the different taper ratios. If the root chord is fixed, a low taper ratio will lead to a small tip chord. This reduces the surfaces of the wing to a certain point where this surface is not able to generate enough lift. In this figure, the black dotted line represents the minimum required lift to maintain flight. Hence, it can be seen that a taper ratio lower than 0.2 gives a wing, not able to generate enough lift. This value will be the lower bound for this parameter.

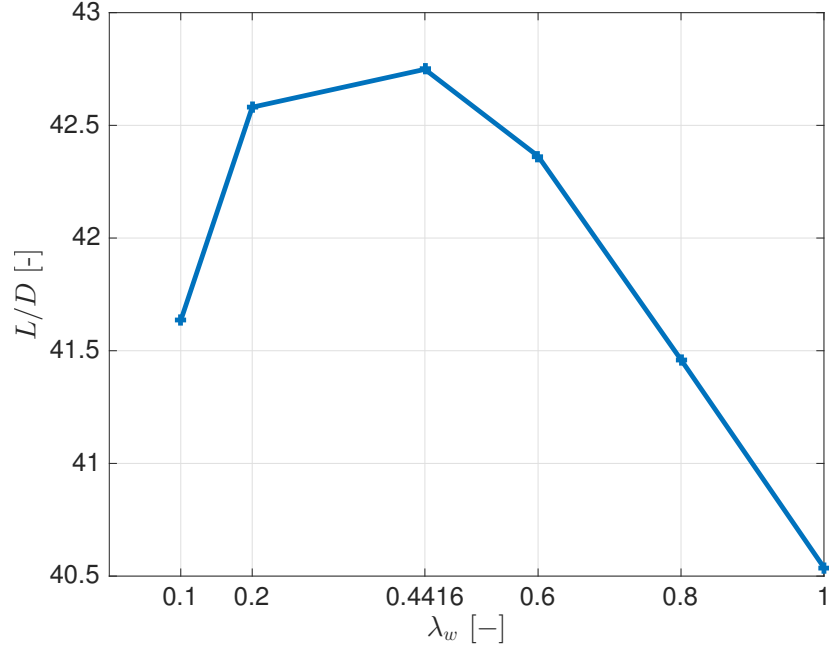


Figure 9.1: Lift to drag ratio  $L/D$  in function of the wing's taper ratio  $\lambda_w$  (every other parameter is set to default)

In summary, the range of variation of the wing's taper ratio is equal to  $\lambda_w = [0.2, 0.4416, 0.6, 0.8]$ .

## 9.2 Sweep angle of the wing $\Lambda_w$

Blended wing UAV's often appear to have backwards swept wings. This is caused by the absence of fin. Indeed, for the control of pitch, ailerons also serve as elevators, they are called elevons<sup>1</sup>. The required magnitude of aerodynamic forces generated by the elevons in order to ensure good flight dynamics can be reduced if the longitudinal lever arm with respect to the center of gravity is large enough. If it is, the size of control surfaces will be greatly reduced. Hence, the backward sweeping of wings on BWB is often mandatory.

Earlier in this thesis, it has been mentioned that the focus of the work is put on the aerodynamic properties of the drone. The variation of the sweep angle of the wing is a typical example where two disciplines collide, i.e. the aerodynamics and the stability. Changing the sweep angle will inevitably have an impact on stability. Major changes in sweep angle will be, for this particular reason, limited to a maximum of  $35^\circ$ . The range of variation of the sweep angle will be comprised between  $15^\circ$  and  $35^\circ$ .

The convention for measuring the sweep angle of the wing  $\Lambda_w$  will be the one shown in Figure 9.3. The sweep angle is measured from the leading edge at a distance from the half-span of  $308\text{ mm}$ . The default sweep angle of the wing is  $27.5879^\circ$ .

---

<sup>1</sup>Ailerons sometimes control the yaw of the aircraft and are then called rudders.

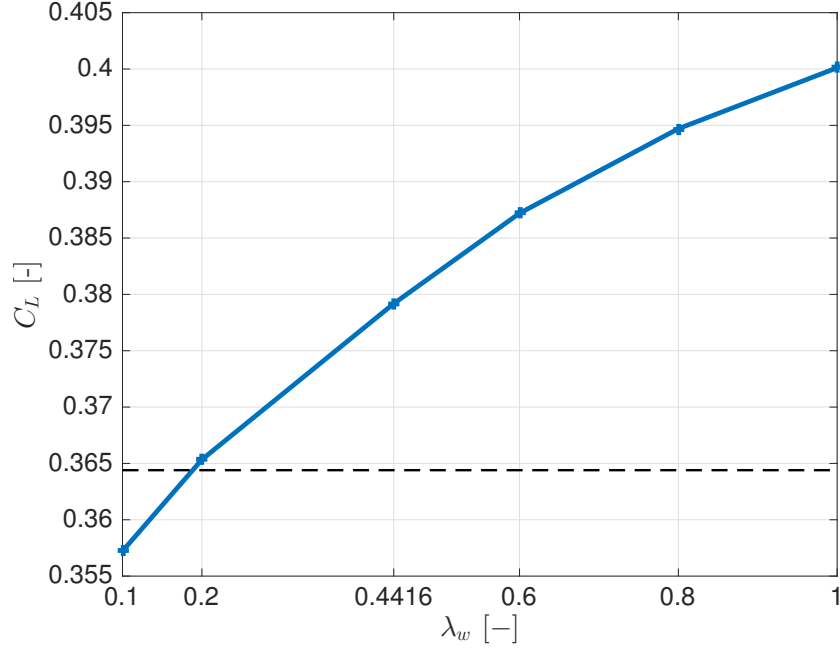


Figure 9.2: Lift coefficient  $C_L$  in function of the wing's taper ratio  $\lambda_w$  (every other parameter is set to default). The black dotted line represents the minimum lift required to maintain flight

In Figure 9.4 the lift to drag ratio is represented in function of the sweep angle of the wing. It can be seen that the lift to drag ratio increases as the angle of sweep becomes larger. An increase of lift to drag ratio is the desired result. It is thus tempting to further increase the angle of sweep. However, one should pay attention to the fact that a swept wing results in the decomposition of the flow over the airfoil in a spanwise and chordwise flow. The effective free stream velocity seen by the wing is reduced by a certain amount given by,

$$V_{eff} = V_{\infty} \cos \Lambda_w. \quad (9.2)$$

At a given angle of attack, the lift coefficient produced by the wing is reduced. At an angle of attack equal to  $2^\circ$ , a sweep angle equal to  $45^\circ$  leads to a value of lift below the minimum required to maintain flight. The chosen interval between  $15^\circ$  and  $35^\circ$  is thus validated.

### 9.3 Height of the winglet $h_{wt}$

The importance of the winglet has already been highlighted during the choice of parameters. It was shown that increasing the height of the winglet and hence the effective aspect ratio leads to a decrease of induced drag but also increases the friction drag. Hence, increasing the height is advantageous up to the point where the induced drag curve meets and becomes smaller than the friction drag curve. This is shown in Figure 9.5.

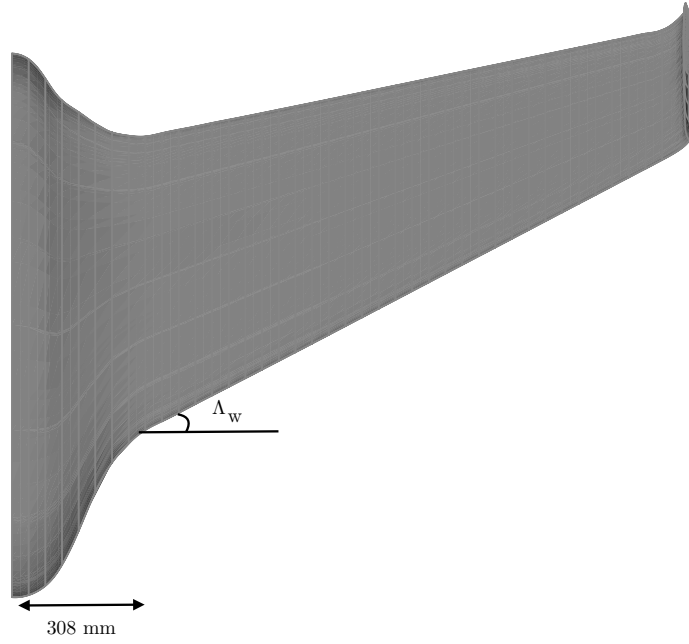


Figure 9.3: Convention for the measure of sweep angle of the wing  $\Lambda_w$

The graph shows the evolution of the induced and friction drag when the height of winglet is changed. The induced drag is shown to decrease when the height of the winglet is increased. This is an expected phenomenon and has already been explained earlier in this section. As the size of the winglet increases the friction drag's prominence increases to a point where it becomes larger than the induced drag. Further increase of the height of the winglet beyond this point is useless. This intersection of the curves occurs for a 0.25 m high winglet. Note that the default winglet's height is 0.198.

The range of variation for the height of the winglet will be comprised between 0 and 0.25 meters. The different values for this parameter will be  $[0, 0.1, 0.198, 0.25]$  m.

## 9.4 Taper ratio of the winglet $\lambda_{wt}$

The taper ratio of the winglet  $\lambda_{wt}$  is defined in the same way that the taper ratio of the wing was defined. Here, the root chord is fixed by the taper ratio of the wing. Changing the taper ratio of the winglet will thus affect the tip chord of the winglet. The default value of  $\lambda_{wt}$  for the baseline geometry is 0.5465.

In Figure 9.6, the lift to drag ratio is represented in function of the taper ratio of the winglet. It shows that the lift to drag ratio increases as the taper ratio gets closer to a value of one. Graphs will not be showed here, but one could plot the lift and drag coefficients in function of the taper of the winglet and observe that the lift coefficient remains approximately constant. The induced drag however does not remain constant but decreases when the taper ratio gets closer to one. This leads to the observed increase in lift to drag ratio in Figure 9.6.

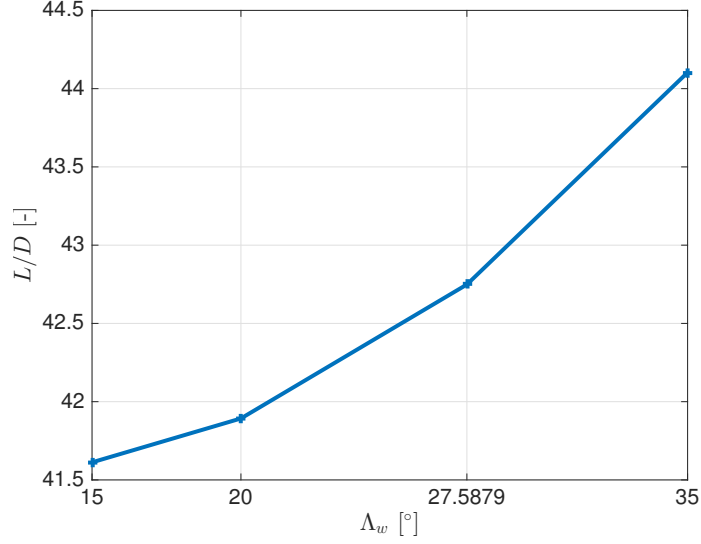


Figure 9.4: Lift to drag ratio  $L/D$  in function of the sweep angle of the wing  $\Lambda_w$  (every other parameter is set to default)

## 9.5 Sweep angle of the winglet $\Lambda_{wt}$

The sweep angle of the winglet's default value is  $35.9245^\circ$ . The convention for the measurement of the sweep angle is the same as the one for the wing, i.e. measured from the leading edge (this is represented in Figure 9.7).

When looking at commercial aircraft, winglets are often swept. The explanation for this, is the same as for swept wings. The flows around the wing for speeds generally observed for those type of aircraft are often transonic or supersonic. Compressibility effects then have to be taken into account. Swept wings and winglets allow for a reduction of the compressibility effects.

For the UAV, the cruise speed is much lower and compressibility effects have less importance. Hence, swept winglets, aside maybe for the aesthetics, have no real purpose. In Figure 9.8, the lift to drag ratio is shown in function of the sweep angle of the winglets. As anticipated, the lift to drag ratio does not change significantly. Indeed, different sweep angles lead to a lift to drag ratio that is bounded between 42.6 and 42.8.

The study of  $\Lambda_{wt}$  has been done while keeping all other parameters as default. For the sake of completeness and because the interaction with other geometry parameters is not known, the sweep angle of the winglet will be varied during the full parametric study. Its value will be  $[0, 15, 25, 35.9245]$ .

## 9.6 Summary of the parametric study

A summary of the parameters and their range of values can be found in Table 9.1. In this table, the green cells represent the default values of the baseline geometry.

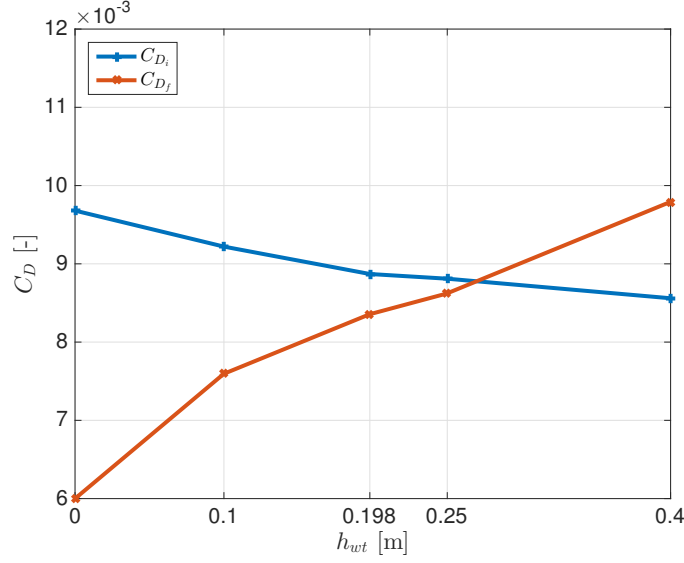


Figure 9.5: Friction drag  $C_{D_f}$  and induced drag  $C_{D_i}$  in function of the winglet height  $h_{wt}$  (every other parameter is set to default)

All parameters will be combined to test each and every configuration. The combination of six parameters with each four different possible values gives a total of 1024 combinations. Even if, strictly speaking, the computation time is relatively low with PanAir, the pre- and post-processing can become consequent. Indeed, PanAir requires a very case-sensitive specifically formatted input file. If not done properly, this may lead to various not easily identifiable errors.

Wing		Winglet		
Taper ratio	Sweep angle	Height	Taper ratio	Sweep angle
$\lambda_w$	$\Lambda_w$	$h_{wt}$	$\lambda_{wt}$	$\Lambda_{wt}$
0.2	15	0	0.3	0
0.4416	20	0.1	0.5465	15
0.6	27.5879	0.1980	0.8	25
0.8	35	0.25	1	35.9245

Table 9.1: Summary of the parameters and their range of values for the parametric study. Green cells represent the default values of the baseline geometry.

When dealing with 1024 possible combinations, the need for automation of the process becomes evident. Actively interacting with a command line program can be tedious. Natively, PanAir does not allow to launch the program with a predefined input file as argument. For automation of the process, a Python script was written allowing the interfacing between PanAir and a terminal. The results were then scanned to find the combination that maximises the objective function and meets the lift requirements. Note that all cases will be performed at an angle of attack of

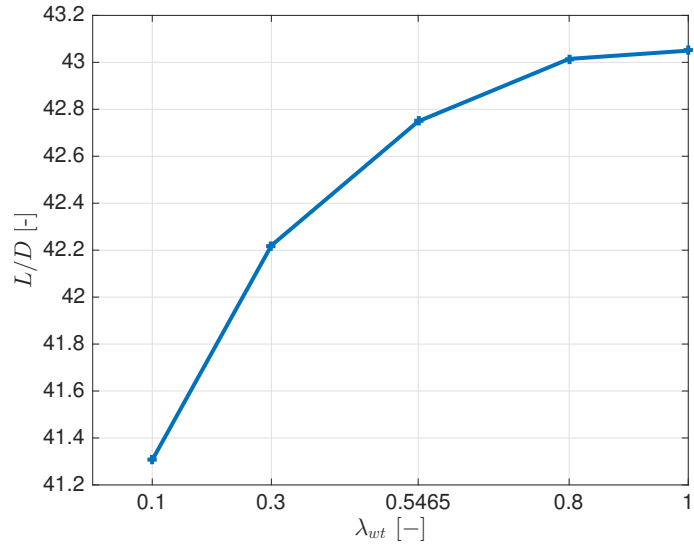


Figure 9.6: Lift to drag ratio  $L/D$  in function of the winglet's taper ratio  $h_{wt}$  (every other parameter is set to default)

two degrees. The free stream velocity will be equal to 18 m/s. The preprocessing script for PanAir implementing the different geometry parameters has been provided in Appendix A. This way, it will be easy to reproduce the results in future works. The Matlab script also outputs a data file that can be interpreted by CAD softwares.



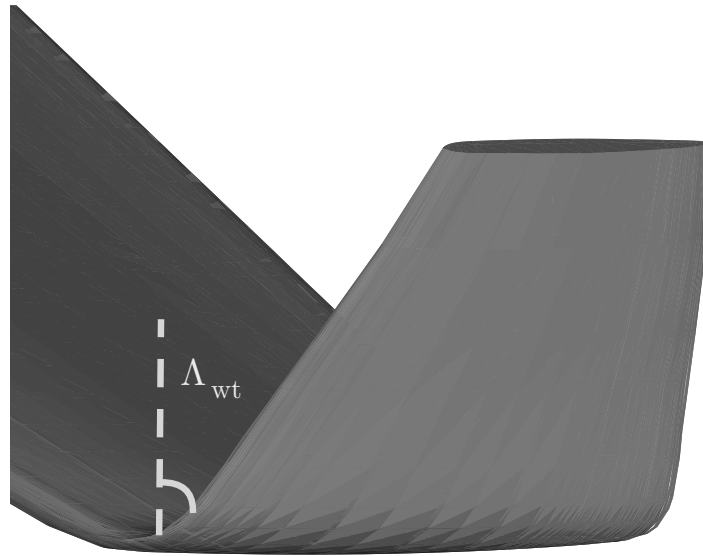


Figure 9.7: Convention for the measure of the winglet's sweep angle  $\Lambda_{wt}$

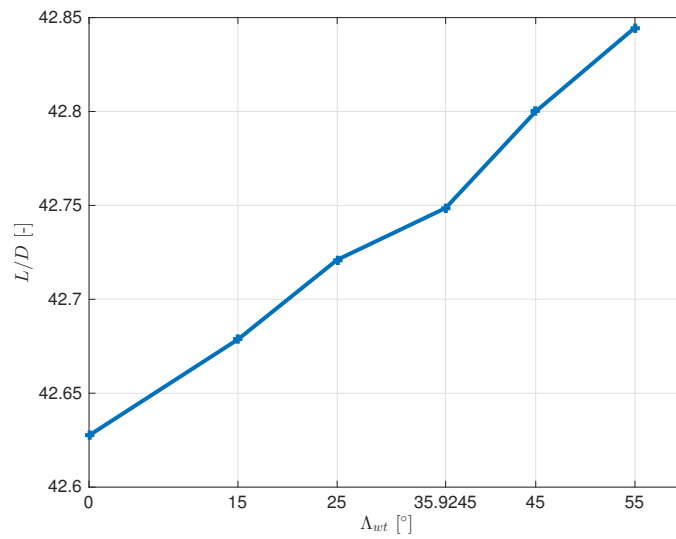


Figure 9.8: Lift to drag ratio  $L/D$  in function of the winglet's sweep angle  $\Lambda_{wt}$  (every other parameter is set to default)

# Chapter 10

## GE<sup>+</sup> geometry

The different parameter combinations were sorted in descending order according to their lift to drag ratios. The first combination of this sorted list that met the minimum lift requirement was then chosen to be the enhanced geometry GE+. This GE+ geometry is the combination of parameters displayed in Table 10.1.

	GE <sup>+</sup>
$\Lambda_w$	35°
$\lambda_w$	0.2
$\Lambda_{wt}$	25°
$\lambda_{wt}$	0.3
$h_{wt}$	0.1 <i>m</i>

Table 10.1: Adapted parameters for the new UAV geometry GE°

To summarize, the sweep angle of the wing has been increased by about 7.5°, the taper ratio of the wing has been reduced by 0.2, the sweep angle of the winglet has been reduced by about 10°, the taper ratio of the winglet has been reduced by 0.24 and finally, the height of the winglet was reduced by 0.1 *m*.

The geometries of the baseline GE1 and the upgraded GE<sup>+</sup> are shown next to each other for schematic comparison in Figures 10.1 and 10.2.

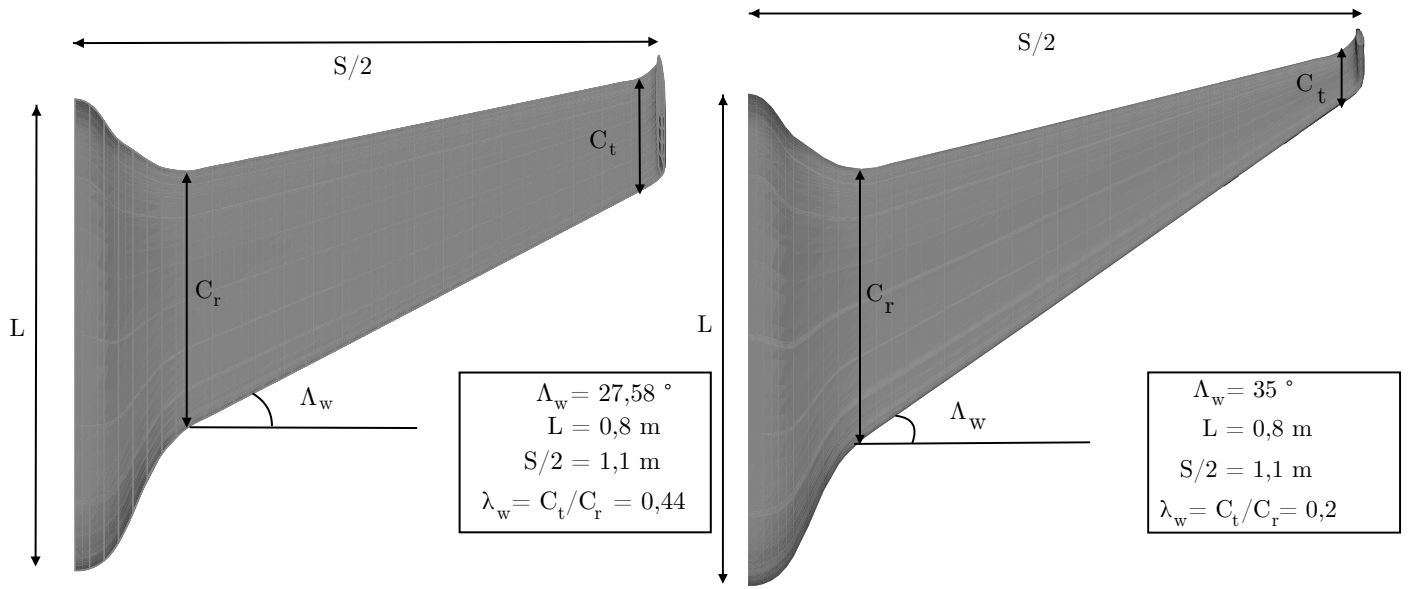


Figure 10.1: Schematic representation of the differences in main parameters for the wing of both the GE1 and GE+

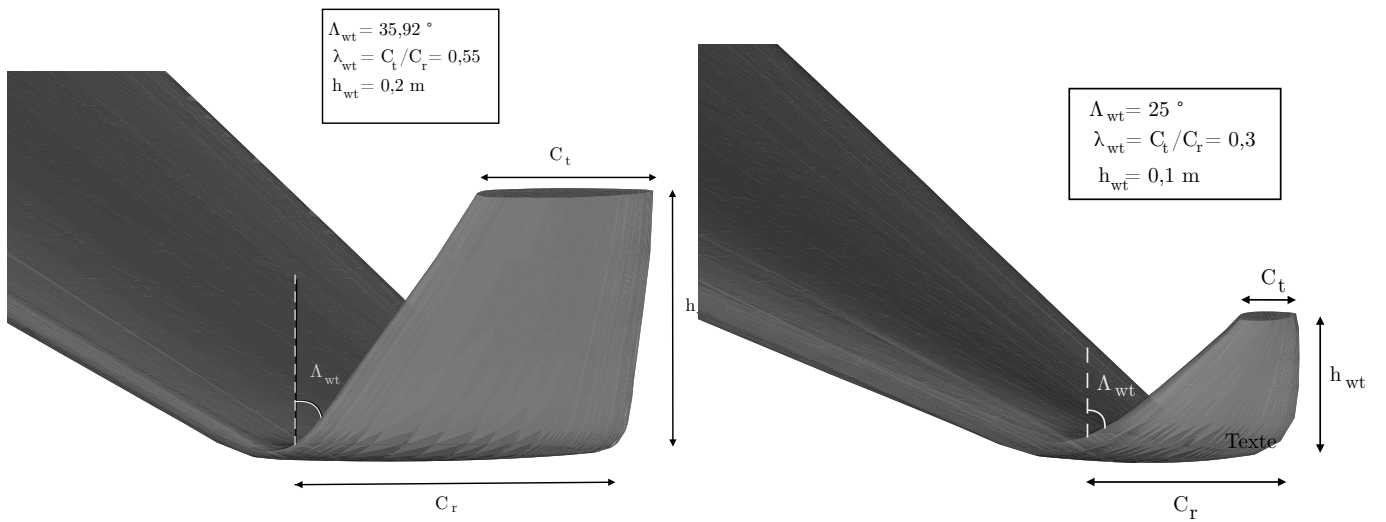


Figure 10.2: Schematic representation of the differences in main parameters for the winglets of both the GE1 and GE+

# Chapter 11

## Detailed analysis of the GE<sup>+</sup>

In this section, a detailed analysis of the aerodynamic behaviour of the GE<sup>+</sup> will be performed similarly to what has been done with the GE1. Results (of the GE<sup>+</sup>) will also be compared to the properties of the GE1.

The objective is to study and validate the new geometry proposal and show that it is indeed superior to the GE1.

### 11.1 Lift coefficient versus angle of attack

In Figure 11.1, the lift coefficient versus the angle of attack has been plotted. Values of lift coefficient appear to be higher for the enhance geometry and hence the lift curve slope too. The lift curve slope for the GE1 is equal to 3.8/rad whereas the GE<sup>+</sup> has a lift curve slope equal to 4.67/rad. The stall seems to appear at the same angle of attack as the GE1.

### 11.2 Drag coefficient versus angle of attack

The drag coefficient for both configurations is represented in function of the angle of attack in Figure 11.2. It is observed that the drag coefficient of the GE<sup>+</sup> is smaller than the one of the GE1. The average absolute difference is equal to 0.004.

### 11.3 Pitching moment versus angle of attack

The pitching moment in function of the angle of attack is represented in Figure 11.3. The pitching moment of the GE<sup>+</sup> is still negative for an angle of attack of 0°. No significant changes with respect to the GE1 are observed besides a little offset of  $-0.02$  on average. During the analysis of the baseline geometry, it was highlighted that the slope of the pitching moment versus the angle of attack had to be negative in order for the aircraft to be stable longitudinally. This was the case for the GE1. For the GE<sup>+</sup>, the pitch curve slope is equal to,

$$\frac{\partial C_m}{\partial \alpha} = -1.79/rad. \quad (11.1)$$

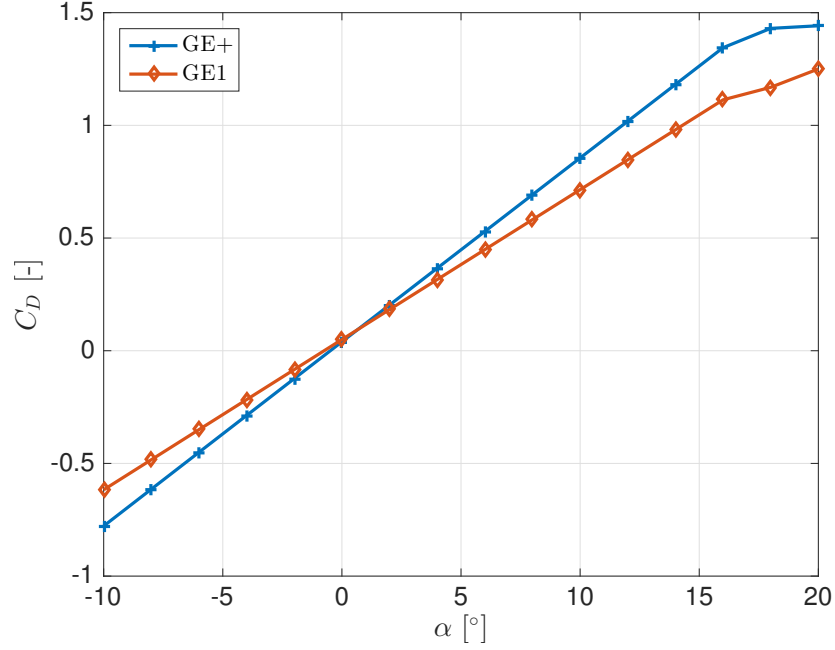


Figure 11.1: Lift coefficient  $C_L$  in function of the angle of attack  $\alpha$  for the GE1 and GE+ geometry

This means that the enhanced design is still stable longitudinally. The increment in pitching moment with a change of angle of attack is nose down.

## 11.4 Lift to drag ratio versus angle of attack

In the introduction on BWB, it was highlighted that an optimised lift to drag ratio was key in optimizing the performance of an aircraft. The lift to drag ratios of both designs are represented and compared in Figure 11.4. In preceding sections, an increase in lift coefficient and a decrease of the drag have been observed for the GE+. The lift to drag ratio of the GE+ is thus expected to be superior to the GE1. The curves intersect each other at an angle of attack of zero degrees. The maximum lift to drag ratio appears at an angle of attack of six degrees but has a different value for the two designs. The GE1 has a maximum  $L/D$  ratio of 12.94, whereas the GE+'s maximum  $L/D$  ratio is equal to 12.1. This increase is equivalent to an increase of 7%.

Optimal conditions for the cruise are the ones that maximise the  $L/D$  ratio. For similar BWB, optimal values of angles of attack between three and six degrees are often found (Wisnoe [29] and Lehmkuehler [14])

To summarize, the GE+ geometry appears to increase the  $L/D$  ratio by an amount of 7% in cruise conditions.

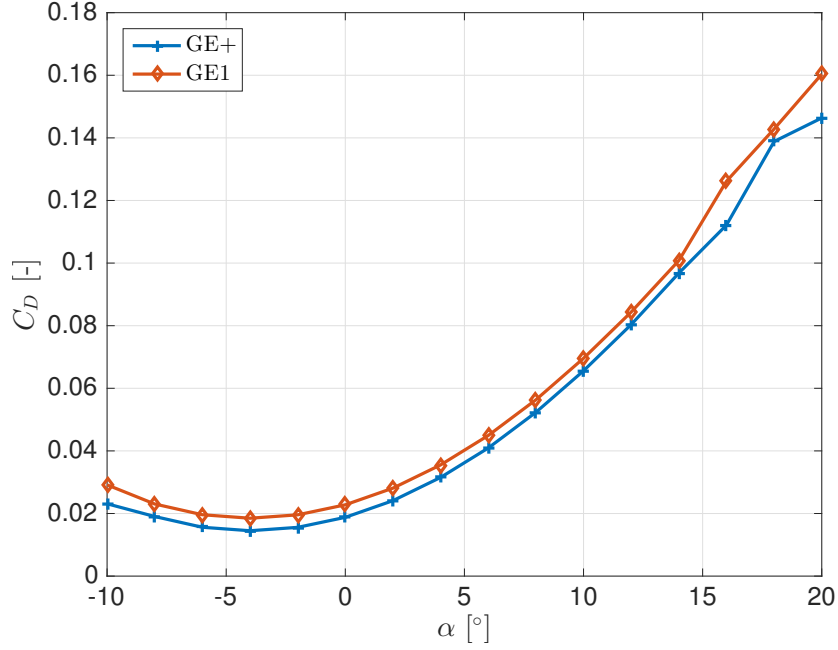


Figure 11.2: Drag coefficient  $C_D$  in function of the angle of attack  $\alpha$  for the GE1 and GE+ geometry

## 11.5 Influence of sideslip

During the analysis of the influence of sideslip angle on the GE1, it has been highlighted that the lift generation dropped passed a certain angle of sideslip. Flying with crosswind can happen on a regular basis and such drop of lift is not wanted. It is interesting to see how the new geometry behaves in the same conditions.

Lift coefficient in function of the sideslip angle for the GE1 and GE+ are compared in Figure 11.5. The same tendency as the GE1 is observed. However, the drop of lift starts at an angle of sideslip of  $10^\circ$  compared to  $8^\circ$  for the GE1.

In fact, this delay in the drop of lift is caused by the new shape of the winglet. Compared to the GE1, the GE+ has a much small winglet. In the presence of crosswind, the big winglet of the GE1 disturbs the flow around the wing because of the wake it creates. The wake created and transported on the tip of the wing also exists for the GE+ but is much smaller because of the reduced size of the winglet.

## 11.6 Influence of control surfaces

Control surfaces have also been implemented in the GE+ geometry. However, results will not be shown here as they are not of particular interest. With the same conditions and deflection angles, the successive increments in lift coefficient have the same proportions as the GE1.

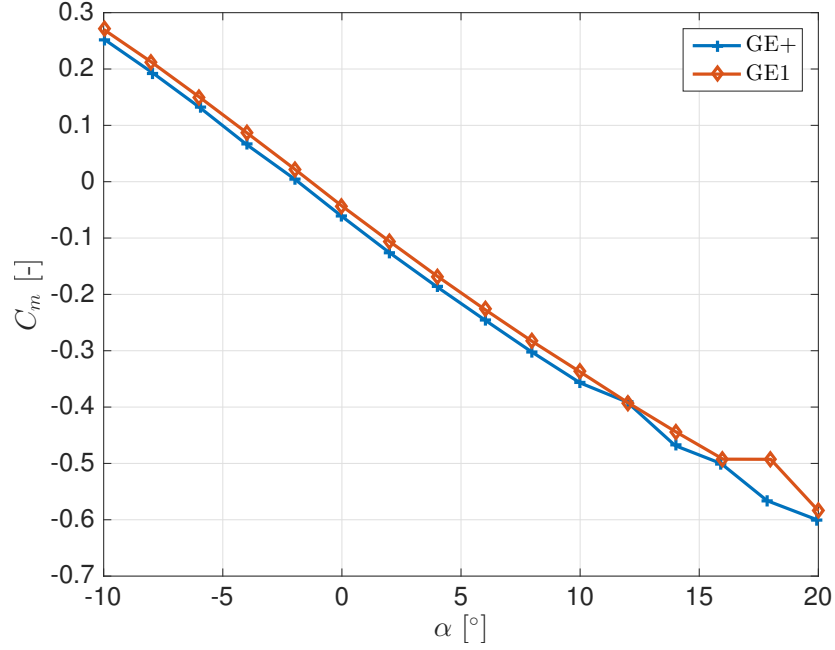


Figure 11.3: Pitching moment  $C_m$  in function of the angle of attack  $\alpha$  for the GE1 and GE+ geometry

## 11.7 Influence of the propulsion

The presence of the propeller is modelled using PanAir like in Section 7.8. The lift coefficient between both engine modes are still not impacted by the presence of the propeller.

It is interesting, however, to look at the drag coefficient's evolution with the angle of attack for both engine modes, see Figure 11.6. Of course, the drag when full power is supplied is still negative. The offset with respect to the case where no thrust is supplied is on average equal to 0.042. This represents a difference of only 0.002 in comparison with what was obtained for the GE1. This very small difference may be explained by the fact that the fuselage of the BWB has not been modified between the GE1 and GE+ models and that the slipstream of the propeller is mainly located around the fuselage.

## 11.8 Summary

To summarize what has been concluded in the preceding sections, it is fair to say that the GE+ shows better performance than the GE1. Indeed, the lift to drag ratio has been shown to increase of 7%. The behaviour of the GE+ was shown to be improved with respect to the GE1. The effects of the propeller, on their hand, were very similar.

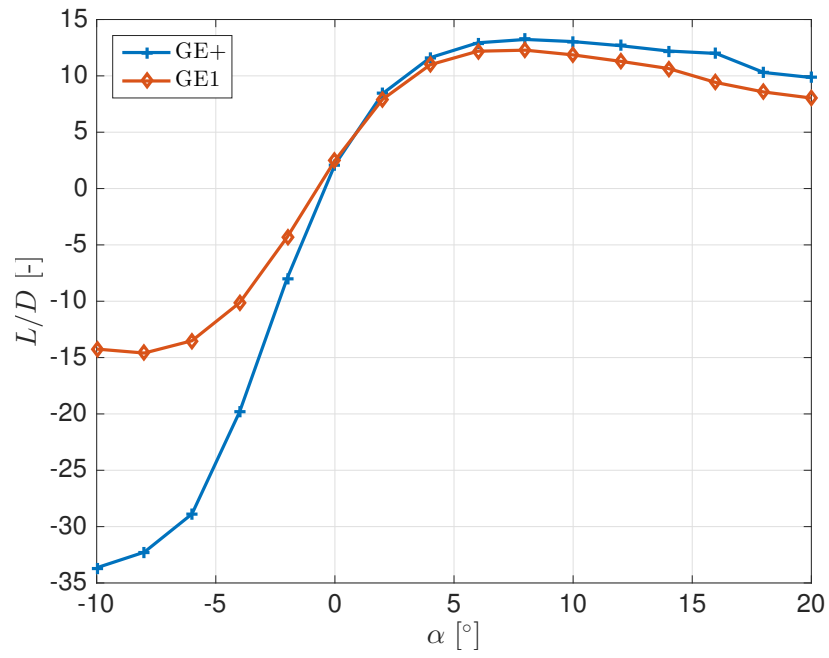


Figure 11.4: Lift to drag ratio  $L/D$  in function of the angle of attack  $\alpha$  for the GE1 and GE+ geometry

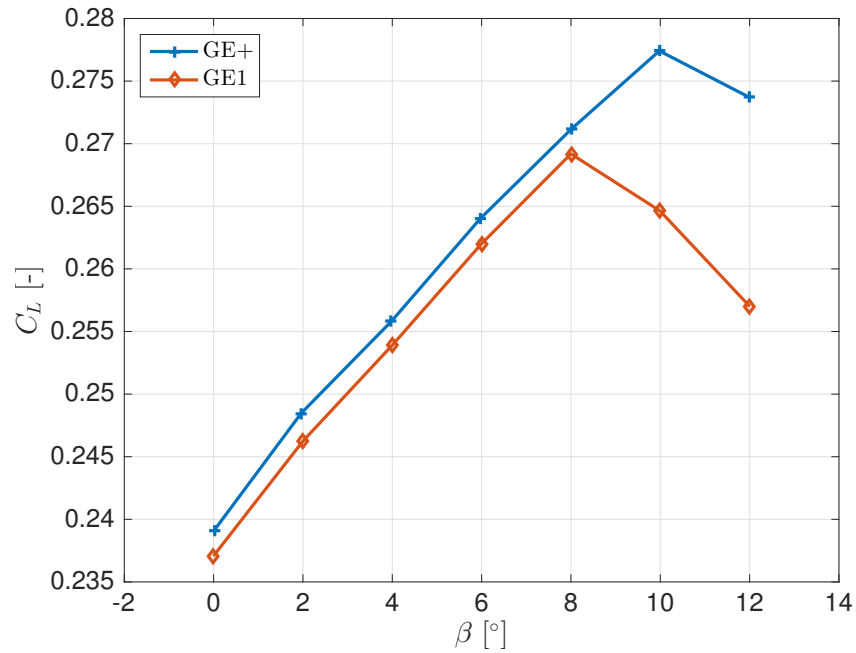


Figure 11.5: Lift coefficient  $C_L$  in function of the sideslip angle  $\beta$  for the GE1 and GE+ when  $U_\infty = 18 \text{ m/s}$  and the  $AOA = 2^\circ$



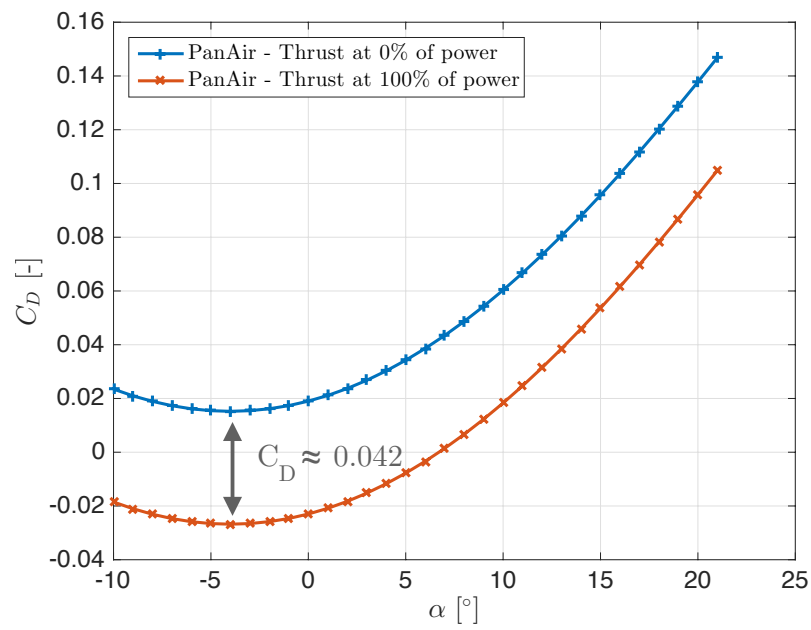


Figure 11.6: Drag coefficient  $C_D$  in function of the angle of attack  $\alpha$  for both engine modes (zero and full thrust) for the GE+

# Chapter 12

## Reynolds effect on GE+

A sensitivity analysis on the Reynolds has been performed to assess if a wind tunnel test could be conducted on a reduced sized model to verify the predicted results for the GE+.

A sensitivity analysis on the Reynolds had already been performed during the wind tunnel tests. It appeared the lift and drag coefficient were almost independent of the Reynolds number when no thrust was supplied. Things were different when thrust was applied. Even if the lift coefficient was still fairly independent of the Reynolds number, the drag coefficient was not.

To verify this tendency, the airspeed has been varied from 6 to 20 m/s for different angles of attack, namely 0°, 4°, 8°, 12° and 16°. Results were computed using PanAir as the propeller had to be modelled.

Results for the lift coefficients when no thrust is applied are shown in Figure 12.1. Here, it can be seen that the lift coefficients remain fairly constant for different airspeeds. Note that the drag coefficient shows the same independency but will not be showed here.

As soon as full thrust is supplied, the drag coefficient shows dependency for the airspeed, especially for low speeds. Results for the drag coefficient are represented in Figure 12.2.

To conclude, it is fair to say that a reduced sized model could be used to confirm the predicted results for the GE+ when the presence of thrust is ignored. A wind tunnel test would, however, have to be performed with great care if the effects of the propeller are not neglected. Indeed, it has been observed that the drag coefficient is dependent of the Reynolds number in such a case.

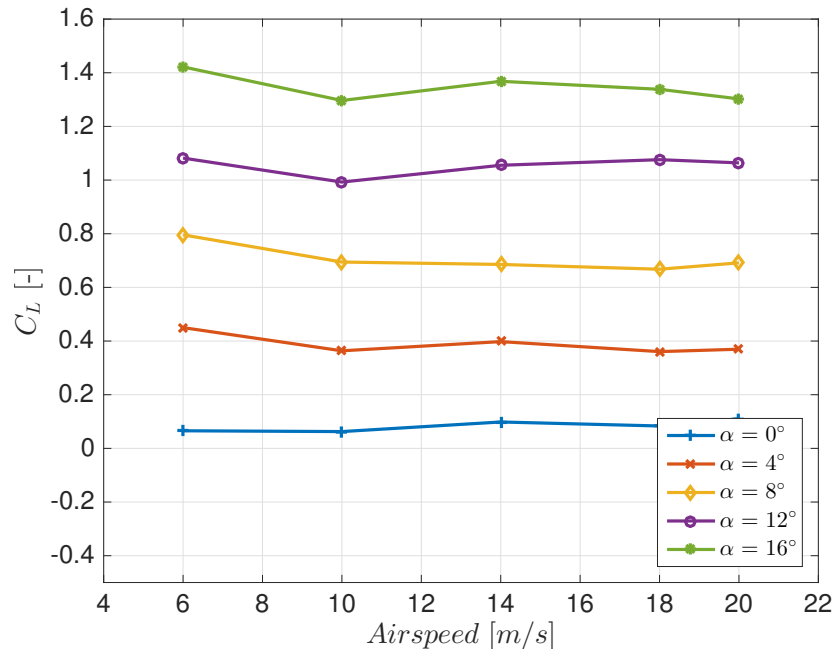


Figure 12.1: Lift coefficient  $C_L$  in function of the free stream airspeed for different angles of attack and when no thrust is supplied

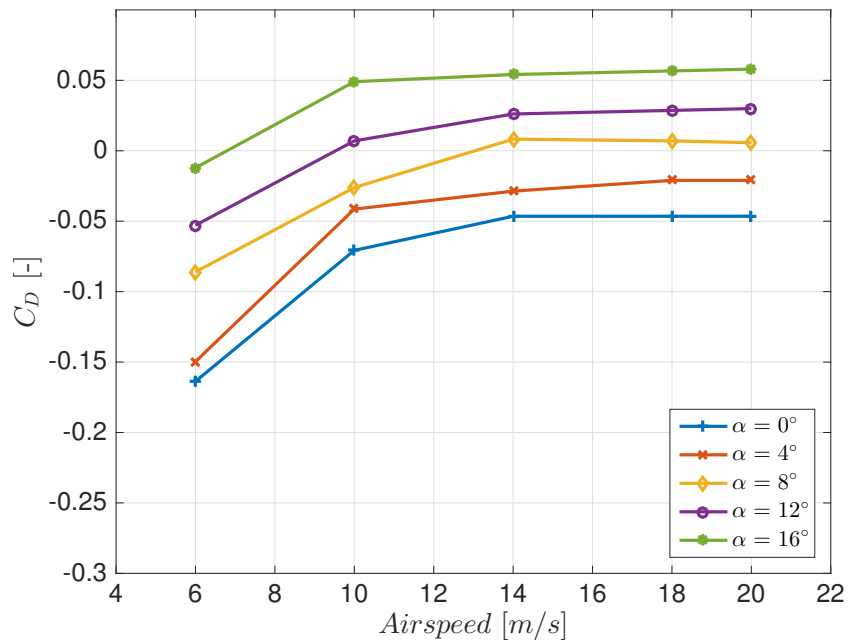


Figure 12.2: Drag coefficient  $C_D$  in function of the free stream airspeed for different angles of attack and when full thrust is supplied

# Conclusions

# Conclusion

In this thesis, a review of the history of blended wing bodies has been done and the various advantages that blended wing bodies offer has been exposed. The increased aerodynamic performance as well as noise reduction assures blended wing bodies a bright future.

The goal of the thesis was to aerodynamically study a blended wing body UAV and propose a new enhance geometry.

To do that, two different methods of analysis were first validated through comparison with experimental results of simple geometries (NACA wings). Those two methods included a low-fidelity one, PanAir and a higher fidelity one, SU<sup>2</sup>. PanAir results turned out to be quite accurate provided that the drag coefficient was corrected. Some limitations of PanAir have, however, been highlighted namely when it was applied to configurations comprising flaps. SU<sup>2</sup> showed better results but its computation time was much more important.

A detailed analysis of the baseline design of the UAV was then performed. Different aerodynamic coefficients were investigated as well as the influence of parameters of the flow. The influence of sideslip angle, control surfaces and propulsion has been studied.

Once the baseline geometry had been analysed, a parametric model of the geometry has been built. The idea was to change the geometry in order to improve the lift to drag ratio. First, the different parameters susceptible of being changed were studied separately to define the final set of varying parameters and their range of values.

A combination of the different parameters led to the study of 1024 different cases that were all compared to one another in order to find the one that maximized the lift to drag ratio while maintaining the required lift. A new geometry has thus been proposed.

The new geometry has been studied and compared to the old one to assess if it improved the aerodynamic performance. It turned out the new geometry induced an increase of 7% of the lift to drag ratio. The behaviour of the UAV when facing crosswind appeared to also be improved.

Finally, a sensitivity analysis on the Reynolds was performed to see if a future wind tunnel test campaign on a reduced size model could be possible. Trends showed that it was safe to analyse the UAV at different Reynolds number when the presence

of thrust was ignored. The introduction of thrust led to some dependencies on the Reynolds pointing to the fact that a wind tunnel test should be performed cautiously.

# Future works

During the completion of this thesis, many hypothesises were made. Hence, a lot of improvement is possible. Improvements or future works can be divided into two categories, the ones that are related to the aerodynamics and the ones that are not.

The elaboration and complexity of the model is a point that can be improved. For instance, the influence of the camera module has been neglected. Surveillance being its primary mission, the deployment of the camera is of great importance and its influence needs to be assessed on the aerodynamic performance of the UAV. Whether it is the increase of drag due to the increased area, or the stability of the aircraft once it is deployed. The introduction into the model of the camera module is thus one potential improvement.

As it has been mentioned in the thesis, the amount of combinations possible when studying the control surfaces is huge. A new study focusing on the control surfaces with the objective to redesign and optimize their positions and shape is another potential work.

The actuator disk theory has not been implemented in SU<sup>2</sup>. A potential improvement for the CFD model would be to introduce this theory into SU<sup>2</sup>.

All analyses were performed for steady conditions. Some dynamic phenomenons such as flutter are, yet, very important when it comes to designing an aircraft. Those were totally neglected in this thesis but would justify another report focussing on those dynamical phenomenons.

Room for future studies regarding other disciplines is also available. For instance, the different geometry parameters were changed without taking manufacturing limitations into account. It has to be investigated whether the construction of the new geometry is feasible. Also, it has to be verified that the new geometry will be able to support the aerodynamical loads structure-wise.

Finally, all the results could be verified during a new wind tunnel test campaign on the reduced size GE+mini. These tests would be performed in the same conditions as the first wind tunnel test campaign. The addition of other variable (such as sideslip angle) would be interesting to study experimentally.

## **Acknowledgements**

I would like to express my appreciation to the people without whom the completion of this thesis would not have been possible.

Thomas Andrianne who guided me through the different possible paths to take. I would like to thank him for the time he took reviewing my report and giving me legitimate and objective comments.

Adrien Crovato who gave me a lot of little tips and often helped me getting started with the different softwares that were used.

And finally, David Thomas for his time and patience while he introduced me to SU<sup>2</sup>.



# Bibliography

- [1] Computational resources have been provided by the Consortium des Équipements de Calcul Intensif (CÉCI), funded by the Fonds de la Recherche Scientifique de Belgique (F.R.S.-FNRS) under Grant No. 2.5020.11No Title.
- [2] Smithsonian National Air and Space Museum. Northrop n1m, 2014. [Online; accessed April 25, 2016].
- [3] Milton B. Jr. Ames. Wind-tunnel investigation of two airfoils with 25-percent-chord Gwinn and plain flaps. Technical report, Washington, 1940.
- [4] Thomas Andrianne. Test report - Drone Vigano. Technical report, University of Liège, 2014.
- [5] A. L. Bolsunovsky, N. P. Buzoverya, B. I. Gurevich, V. E. Denisov, A. I. Dunaevsky, L. M. Shkadov, O. V. Sonin, A. J. Udzhuhu, and J. P. Zhurihin. Flying wing - Problems and decisions. *Aircraft Design*, 4(4):193–219, 2001.
- [6] Douglas Bullard. The ix v-2 is nearly finished, 1997. [Online; accessed April 15, 2016].
- [7] M Carmichael. PanAir, 2010.
- [8] Alexandre J. Chorin. A Numerical Method for Solving Incompressible Viscous Flow Problems. *Journal of Computational Physics*, 135:118–125, 1997.
- [9] Boeing Company. B-737 max, 2016. [Online; accessed April 13, 2016].
- [10] Glen W. Edwards. Usaf archive, flying wing, a heavy bomber prototype, 2005. [Online; accessed April 24, 2016].
- [11] L. Larry Erickson. Panel Methods - An Introduction, 1990.
- [12] Harry J Goett and W Kenneth Bullivant. Tests of NACA 0009, 0012, and 0018 Airfoils in the Full-Scale Tunnel. Technical report, NACA, Langley Field, United States, 1939.
- [13] Ohad Gur, H. Mason Mason, and A. Joseph Schetz. Full-Configuration Drag Estimation. *Journal of Aircraft*, 47(4):1358–1359, 2010.
- [14] K Lehmkuehler, K C Wong, and D Verstraete. Design and test of a UAV blended wing body configuration. *28th Congress of the International Council of the Aeronautical Sciences 2012, ICAS 2012*, 1(April):432–442, 2012.

- [15] R H Liebeck. Design of the Blended Wing Body Subsonic Transport. *Journal of Aircraft*, 41(1), 2004.
- [16] V Mukhopadhyay. Blended-Wing-Body (BWB) Fuselage Structural Design for Weight Reduction. In *46th AIAA/ASME/ASCE/AHS/ASC Structures, Structural Dynamics and Material Conference*, 2005.
- [17] V Mukhopadhyay, J Sobieszczanski-Sobieski NASA Langley, Va I Kosaka, G Quinn, C Charpentier, J Sobieszczanski-Sobieski, and I Kosaka. Analysis Design and Optimization of Non-cylindrical Fuselage for Blended-Wing-Body (BWB) Vehicle. *9th AIAA/ISSMO Symposium on Multidisciplinary Analysis and Optimization*, 2002.
- [18] National Museum of the US Air Force. Northrop b-2 spirit, 2011. [Online; accessed April 24, 2016].
- [19] U.S. Department of Transportation. Unmanned Aircraft System (UAS) Service Demand 2015 -2035 Literature Review & Projections of Future Usage. Technical report, 2013.
- [20] Francisco Palacios, Michael R Colonno, Aniket C Aranake, Alejandro Campos, Sean R Copeland, Thomas D Economon, Amrita K Lonkar, Trent W Lukaczyk, Thomas W R Taylor, and Juan J Alonso. An open-source integrated computational environment for multi-physics simulation and design, 2013.
- [21] J. H Paterson, D. G. MacWilkinson, and W. T. Blackerby. A Survey of Drag Prediction Techniques Applicable to Subsonic and Transonic Aircraft Design. *Aerodynamic Drag*, CP-124, 1973.
- [22] C.M. Poulsen. Tailless trials, tribute to a british pioneer: The dunne biplanes and monoplane, 1943. [Online; accessed April 27, 2016].
- [23] N. Qin, A. Vavalle, A. Le Moigne, M. Laban, K. Hackett, and P. Wienerfelt. Aerodynamic considerations of blended wing body aircraft. *Progress in Aerospace Sciences*, 40(6):321–343, 2004.
- [24] Daniel P Raymer, Richard Hibma, Louis Hecq, Harry Scott, Richard Child, George Owl, Robert Maier, Ed McGachan, Doug Robinson, Steve White, Harvey Hoge, Michael Robinson, George Palmer, Henry Yang, Robert Swaim, C T Sun, Dave Schmidt, Bruce Reese, William Heiser, and Gordon Raymer. *Aircraft Design: A Conceptual Approach*. 2004.
- [25] Gary R. Saaris. A502I User’s Guide-PAN AIR TEchnology Program for Solving Potential Flow about Arbitrary Configurations. *Word Journal Of The International Linguistic Association*, 1992.
- [26] P.R. Spalart and S.R. Allmaras. A One-Equation Turbulence Model for Aerodynamic Flows. *Recherche Aerospatiale*, (1):5,21, 1994.
- [27] Russell H Thomas, Casey L Burley, and Erik D Olson. Hybrid Wing Body Aircraft System Noise Assessment With Propulsion Airframe Aeroacoustic Experiments. In *16th AIAA/CEAS Aeroacoustics Conference*, 2010.

- [28] Daniel J Thompson, Joshuo Feys, Michael D Filewich, Sharif Abdel-magid, Dennis Dalli, and Fumitaka Goto. The Design and Construction of a Blended Wing Body UAV. In *49th AIAA Aerospace Sciences Meeting*, number 4-7 January, pages 1–11, 2011.
- [29] Wirachman Wisnoe, Rizal Effendy, Mohd Nasir, Wahyu Kuntjoro, and Aman Mohd. Wind Tunnel Experiments and CFD Analysis of Blended Wing Body ( BWB ) Unmanned Aerial Vehicle ( UAV ). In *13th Int. Conf. on Aerospace Sciences and Aviation Tech. (ASAT-13)*, 2009.

# Appendices

# Appendix A

```
%% Preprocessing script for PanAir for the BWB UAV
% Martin Masereel

close all;
clear all;

%% Paramètres

elong = 0;
sweepangle = 27.5879; %default is 0.4815 rad or (180/pi)*0.4815 = 27.5879 deg
sweepangle = sweepangle*(pi/180);
taper = 0.4416; %C_tip/C_root default value = 0.1956/0.4429=0.4416
sweepangletip = 35.9245; %default is 0.6270 rad or (180/pi)*0.6270 = 35.9245 deg
sweepangletip = sweepangletip*(pi/180);
tapertip = 0.5465; %C_tip/C_root default value = 0.1069/0.1956 = 0.5465
height_tip = 0.198; %default value is 0.1980

%%
%=====
%=====Import coordinates from CATIA=====
%=====

nb_pts = 41; %Number of interpolation points for airfoil profiles half section (↔
    tot nb pts = nb_pts*2-1)
mesh_GE1 = zeros(nb_pts*2-1,3,49);

typeMeshing = 1; % 0 = Panair meshing / 1 = SU2 meshing
if height_tip ==0
    nb_tips =0;
else
    nb_tips = 10;
end

%/1 Meshing of fuselage
if typeMeshing == 1
    A = xlsread('mesh_fus.xlsx');
    nb_stat = 9; %Number of measurement stations
    indices_stat = [1 438 871 1286 1675 2034 2363 2657 2925 3173]; %delimiter of ↔
        stations
    else
        A = xlsread('mesh_fus_pan.xlsx');
        nb_stat = 9; %Number of measurement stations
        indices_stat = [1 920 1813 2664 3455 4185 4844 5440 5980 6481]; %delimiter of ↔
            stations
    end

%Reorder data as rows of x,y,z
A(1:2:end,1) = A(2:2:end,1);
A(2:2:end,:) = [];
i=1;
j=2;
A(:, [1:i-1,j,i+1:j-1,i,j+1:end]) = [];
i=2;
j=3;
A(:, [1:i-1,j,i+1:j-1,i,j+1:end]) = [];
A = A/1000; %Conversion from mm to m

%Reference wrt nose of the aircraft
```

```

A(:,1) = A(:,1) - 0.744444275748000;
A(:,2) = A(:,2) - 0.563340207575000;
A(:,3) = A(:,3) - 0.712273574574000;

for i=1:nb_stat

[A(indices_stat(i):indices_stat(i+1)-1,1),I] = sort(A(indices_stat(i):↵
    indices_stat(i+1)-1,1));
A(indices_stat(i):indices_stat(i+1)-1,2) = A(indices_stat(i)+I-1,2);
A(indices_stat(i):indices_stat(i+1)-1,3) = A(indices_stat(i)+I-1,3);

[maxCoord, I] = max(A(indices_stat(i):indices_stat(i+1)-1,1));
LE = [maxCoord A(indices_stat(i)+I-1,2) A(indices_stat(i)+I-1,3)];
[minCoord, I] = min(A(indices_stat(i):indices_stat(i+1)-1,1));
TE = [minCoord A(indices_stat(i)+I-1,2) A(indices_stat(i)+I-1,3)];

rico = (LE(2)-TE(2))/(LE(1)-TE(1));
% Initialisation pts
Coord_top = [0 0 0];
Coord_bot = [0 0 0];
tolerance = 0.0009;

for j=1:length(A(indices_stat(i):indices_stat(i+1)-1,1))
    if A(indices_stat(i)+j-1,2) >= (rico*(A(indices_stat(i)+j-1,1)-TE(1))+TE(2))-↵
        tolerance
        Coord_top(end+1,:) = A(indices_stat(i)+j-1,1:3);
    else
        Coord_bot(end+1,:) = A(indices_stat(i)+j-1,1:3);
    end
end
Coord_bot(1,:) = [];
Coord_top(1,:) = [];
Coord_bot = [Coord_top(1,:); Coord_bot; Coord_top(end,:)];

if i<=4
%Elongation of the results
[~,I] = max(Coord_top(:,2));
[~,Y] = min(Coord_bot(:,2));

Coord_top(1:I-1,1) = Coord_top(1:I-1,1) - elong;
Coord_top(I+1:end,1) = Coord_top(I+1:end,1) + elong;
Coord_bot(1:Y-1,1) = Coord_bot(1:Y-1,1) - elong;
Coord_bot(Y+1:end,1) = Coord_bot(Y+1:end,1) + elong;

end

Coord_top(:,1) = Coord_top(:,1)-elong;
Coord_bot(:,1) = Coord_bot(:,1)-elong;

TE(1) = Coord_top(1,1);
LE(1) = Coord_top(end,1);

%Interpolation of results
cosspace = cosspace(TE(1),LE(1),nb_pts);

inter_top = interp1(Coord_top(:,1),Coord_top(:,2),cosspace,'pchip');
inter_bot = interp1(Coord_bot(:,1),Coord_bot(:,2),cosspace,'pchip');

Coord_final = zeros(nb_pts*2,3);
Coord_final(1:2*nb_pts,1) = -[transpose(cosspace);transpose(fliplr(cosspace))↵
    ];
Coord_final(1:2*nb_pts,2) = [transpose(inter_top);transpose(fliplr(inter_bot))];
Coord_final(1:2*nb_pts,3) = Coord_top(1,3);
Coord_final(nb_pts+1,:) = [];
mesh_GE1(:, :, i) = Coord_final;
end

%/2 Meshing of wing
A = xlsread('Airfoils.xlsx');
nb_stat = 40; %Number of measurement stations

```

```

indices_stat = [1 275 542 806 1065 1319 1568 1811 2051 2287 2519 2747 2979 3195 ↵
                3418 3587 3754 3919 4081 4239 4395 4549 4701 4850 4995 5138 5279 5418 5553 ↵
                5686 5817 5946 6071 6194 6315 6434 6550 6663 6774 6883 6990];

%Reorder data as rows of x,y,z
A(1:2:end,1) = A(2:2:end,1);
A(2:2:end,:) = [];
i=1;
j=2;
A = A(:,[1:i-1,j,i+1:j-1,i,j+1:end]);
i=2;
j=3;
A = A(:,[1:i-1,j,i+1:j-1,i,j+1:end]);
A = A/1000; %Conversion from mm to m

%Reference wrt nose of the aircraft
A(:,1) = A(:,1) - 0.744444275748000;
A(:,2) = A(:,2) - 0.563340207575000;
A(:,3) = A(:,3) - 0.712273574574000;

for i=1:nb_stat

[A(indices_stat(i):indices_stat(i+1)-1,1),I] = sort(A(indices_stat(i):↵
indices_stat(i+1)-1,1));
A(indices_stat(i):indices_stat(i+1)-1,2) = A(indices_stat(i)+I-1,2);
A(indices_stat(i):indices_stat(i+1)-1,3) = A(indices_stat(i)+I-1,3);

[maxCoord, I] = max(A(indices_stat(i):indices_stat(i+1)-1,1));
LE = [maxCoord A(indices_stat(i)+I-1,2) A(indices_stat(i)+I-1,3)];
[minCoord, I] = min(A(indices_stat(i):indices_stat(i+1)-1,1));
TE = [minCoord A(indices_stat(i)+I-1,2) A(indices_stat(i)+I-1,3)];

rico = (LE(2)-TE(2))/(LE(1)-TE(1));
% Initialisation pts
Coord_top = [0 0 0];
Coord_bot = [0 0 0];
tolerance = 0.0009;

for j=1:length(A(indices_stat(i):indices_stat(i+1)-1,1))
    if A(indices_stat(i)+j-1,2) >= (rico*(A(indices_stat(i)+j-1,1)-TE(1))+TE(2))-↵
        tolerance
        Coord_top(end+1,:) = A(indices_stat(i)+j-1,1:3);
    else
        Coord_bot(end+1,:) = A(indices_stat(i)+j-1,1:3);
    end
end
Coord_bot(1,:) = [];
Coord_top(1,:) = [];
Coord_bot = [Coord_top(1,:);Coord_bot;Coord_top(end,:)];

Coord_top(:,1) = Coord_top(:,1)-elong;
Coord_bot(:,1) = Coord_bot(:,1)-elong;

TE(1) = Coord_top(1,1);
LE(1) = Coord_top(end,1);

%Interpolation of results
cosspace = cosspace(TE(1),LE(1),nb_pts);

inter_top = interp1(Coord_top(:,1),Coord_top(:,2),cosspace,'pchip');
inter_bot = interp1(Coord_bot(:,1),Coord_bot(:,2),cosspace,'pchip');

Coord_final = zeros(nb_pts*2,3);
Coord_final(1:2*nb_pts,1) = -[transpose(cosspace);transpose(fliplr(cosspace))↵
];
Coord_final(1:2*nb_pts,2) = [transpose(inter_top);transpose(fliplr(inter_bot))];
Coord_final(1:2*nb_pts,3) = Coord_top(1,3);
Coord_final(nb_pts+1,:) = [];
mesh_GE1(:,9+i) = Coord_final;
end

if height_tip ~= 0

```

```

%3 Meshing of the wingtips
A = xlsread('mesh_tip.xlsx');
nb_stat = 11; %Number of measurement stations
indices_stat = [1 193+1 375+1 545+1 702+1 850+1 989+1 1118+1 1238+1 1346+1 ←
1447+1];
%indices_stat = [193+1 375+1 545+1 702+1 850+1 989+1 1118+1 1238+1 1346+1 ←
1447+1];

%Reorder data as rows of x,y,z
A(1:2:end,1) = A(2:2:end,1);
A(2:2:end,:) = [];
i=1;
j=2;
A = A(:, [1:i-1,j,i+1:j-1,i,j+1:end]);
i=2;
j=3;
A = A(:, [1:i-1,j,i+1:j-1,i,j+1:end]);
A = A/1000; %Conversion from mm to m

%Reference wrt nose of the aircraft
A(:,1) = A(:,1) - 0.744444275748000;
A(:,2) = A(:,2) - 0.563340207575000;
A(:,3) = A(:,3) - 0.712273574574000;

for i=1:nb_stat-1

[A(indices_stat(i):indices_stat(i+1)-1,1),I] = sort(A(indices_stat(i):←
indices_stat(i+1)-1,1));
A(indices_stat(i):indices_stat(i+1)-1,2) = A(indices_stat(i)+I-1,2);
A(indices_stat(i):indices_stat(i+1)-1,3) = A(indices_stat(i)+I-1,3);

[maxCoord, I] = max(A(indices_stat(i):indices_stat(i+1)-1,1));
LE = [maxCoord A(indices_stat(i)+I-1,2) A(indices_stat(i)+I-1,3)];
[minCoord, I] = min(A(indices_stat(i):indices_stat(i+1)-1,1));
TE = [minCoord A(indices_stat(i)+I-1,2) A(indices_stat(i)+I-1,3)];

rico = (LE(3)-TE(3))/(LE(1)-TE(1));
% Initialisation pts
Coord_top = [0 0 0];
Coord_bot = [0 0 0];
tolerance = 0.0001;

for j=1:length(A(indices_stat(i):indices_stat(i+1)-1,1))
if A(indices_stat(i)+j-1,3) >= (rico*(A(indices_stat(i)+j-1,1)-TE(1))+TE(3))-←
tolerance
Coord_top(end+1,:) = A(indices_stat(i)+j-1,1:3);
else
Coord_bot(end+1,:) = A(indices_stat(i)+j-1,1:3);
end
end
Coord_bot(1,:) = [];
Coord_top(1,:) = [];
Coord_bot = [Coord_top(1,:);Coord_bot;Coord_top(end,:)];

temp = Coord_top;
Coord_top = Coord_bot;
Coord_bot = temp;

Coord_top(:,1) = Coord_top(:,1)-elong;
Coord_bot(:,1) = Coord_bot(:,1)-elong;

TE(1) = Coord_top(1,1);
LE(1) = Coord_top(end,1);

%Interpolation of results
cosspace = cosspace(TE(1),LE(1),nb_pts);

inter_top = interp1(Coord_top(:,1),Coord_top(:,3),cosspace,'pchip');
inter_bot = interp1(Coord_bot(:,1),Coord_bot(:,3),cosspace,'pchip');

Coord_final = zeros(nb_pts*2,3);

```



```

Coord_final(1:2*nb_pts,1) = -[transpose(coss pacing);transpose(fliplr(coss pacing))↵
];
Coord_final(1:2*nb_pts,2) = Coord_top(1,2);
Coord_final(1:2*nb_pts,3) = [transpose(inter_top);transpose(fliplr(inter_bot))];
Coord_final(nb_pts+1,:) = [];
mesh_GE1(:,:(9+40)+i) = Coord_final;
end
end
%%
% Plotting of the intermediate geometry
figure
for i=1:(9+40+nb_tips)
scatter3(mesh_GE1(:,1,i),mesh_GE1(:,2,i),mesh_GE1(:,3,i),'filled');
hold on
title('Intermediate geometry')
end

%Sweep implementation
mesh_GE1(:,1,10:end) = mesh_GE1(:,1,10:end)-tan(0.4815)*(mesh_GE1(:,3,10:end)↵
-0.2);
mesh_GE1(:,1,10:end) = mesh_GE1(:,1,10:end)+tan(sweepangle)*(mesh_GE1(:,3,10:end)↵
-0.2);

%Taper implementation
C_tip = taper*0.4429;
%factor = C_tip/0.1956;

chord = zeros(40,1);
factor = zeros(40,1);
spacing = linspace(0.4429,C_tip,40);
for i=9+1:9+40
chord(i-9) = mesh_GE1(1,1,i)-mesh_GE1(nb_pts,1,i);
factor(i-9) = spacing(i-9)/chord(i-9);
end
chord = chord.*factor;

for i=9+1:9+40
temp = mesh_GE1(nb_pts,1,i);
mesh_GE1(:,1,i) = mesh_GE1(:,1,i) - mesh_GE1(nb_pts,1,i);
mesh_GE1(:,1,i) = mesh_GE1(:,1,i)/mesh_GE1(1,1,i);
mesh_GE1(:,1,i) = (mesh_GE1(:,1,i))*chord(i-9);
mesh_GE1(:,1,i) = mesh_GE1(:,1,i) + temp;
end

% Correction of the AOA configuration
mesh_GE1(:,2,:) = mesh_GE1(:,2,:) - (-0.0371/0.8195)* mesh_GE1(:,1,:);

if height_tip ~= 0
% Tip

temp = mesh_GE1(nb_pts,1,50);
airfoiltip = mesh_GE1(:,50);
airfoiltip(:,1) = airfoiltip(:,1) - mesh_GE1(nb_pts,1,50);
airfoiltip(:,1) = airfoiltip(:,1)/airfoiltip(1,1);
airfoiltip(:,1) = airfoiltip(:,1)*C_tip;
airfoiltip(:,1) = airfoiltip(:,1) + temp;
mesh_GE1(:,50) = airfoiltip;
mesh_GE1(:,2,50) = mesh_GE1(:,2,50) - 0.02;

%Sweep tip implementation
height_dist = linspace(mesh_GE1(1,2,50),height_tip,10);
for i=1:10
mesh_GE1(:,1,49+i) = mesh_GE1(:,1,50) + (mesh_GE1(nb_pts,1,49+i)-mesh_GE1(nb_pts↵
,1,50))*tan(sweepangletip);
mesh_GE1(:,2,49+i) = height_dist(i);
mesh_GE1(:,3,49+i) = mesh_GE1(:,3,50);
end

%Taper tip implementation

chord = linspace(C_tip,tapertip*C_tip,10);
for i=1:10
temp = mesh_GE1(nb_pts,1,49+i);

```

```

mesh_GE1(:,1,49+i) = mesh_GE1(:,1,49+i) - mesh_GE1(nb_pts,1,49+i);
mesh_GE1(:,1,49+i) = mesh_GE1(:,1,49+i)/mesh_GE1(1,1,49+i);
mesh_GE1(:,1,49+i) = (mesh_GE1(:,1,49+i))*chord(i);
mesh_GE1(:,1,49+i) = mesh_GE1(:,1,49+i) + temp;
end

end

%%
%=====Interpolation between /= stations=====
%

nb_interp_wing = 40;
if height_tip ~= 0
    nb_interp_tip = 5;
else
    nb_interp_tip = 0;
end
nb_interp = nb_interp_wing + nb_interp_tip;

%%
spanwise_spacing = linspace(mesh_GE1(1,3,1),mesh_GE1(1,3,9+40),nb_interp_wing);
mesh_GE1_final = zeros(nb_pts*2-1,3,nb_interp_wing);

for i=1:nb_pts*2-1;

temp = interp1(squeeze(mesh_GE1(i,3,1:49)),transpose(squeeze([mesh_GE1(i,1,1:49)←
,mesh_GE1(i,2,1:49)])),spanwise_spacing,'pchip');

mesh_GE1_final(i,1,:) = temp(:,1);
mesh_GE1_final(i,2,:) = temp(:,2);
end

for i=1:nb_interp_wing
mesh_GE1_final(:,3,i) = spanwise_spacing(i);
end

%%
if height_tip ~= 0

mesh_GE1_final_tip = zeros(nb_pts*2-1,3,nb_interp_tip);

tip_spacing = linspace(mesh_GE1(1,2,50),mesh_GE1(1,2,59),nb_interp_tip);

for i=1:nb_pts*2-1;

temp = interp1(squeeze(mesh_GE1(i,2,50:59)),transpose(squeeze([mesh_GE1(i←
,1,50:59),mesh_GE1(i,3,50:59)])),tip_spacing,'pchip');

mesh_GE1_final_tip(i,1,:) = temp(:,1);
mesh_GE1_final_tip(i,3,:) = temp(:,2);
end

for i=1:nb_interp_tip
mesh_GE1_final_tip(:,2,i) = tip_spacing(i);
end

mesh_GE1_final = cat(3,mesh_GE1_final,mesh_GE1_final_tip);

end

% Correction of the AOA configuration
mesh_GE1_final(:,2,:) = mesh_GE1_final(:,2,:)+(-0.0371/0.8195)* mesh_GE1_final←
(:,1,:);

%% Plotting of interpolated geometry

```

```

%Scatter plot
figure
for i=1:nb_interp
scatter3(mesh_GE1_final(:,1,i),mesh_GE1_final(:,2,i),mesh_GE1_final(:,3,i),'↵
filled');
hold on
title('Interpolated geometry')
end

%Line plot
figure
for i=1:nb_pts*2-1
plot3(squeeze(mesh_GE1_final(i,1,:)),squeeze(mesh_GE1_final(i,3,:)),squeeze(↵
mesh_GE1_final(i,2,:),'color',[0.5 0.5 0.5])
hold on
end
for i=1:nb_interp
plot3(squeeze(mesh_GE1_final(:,1,i)),squeeze(mesh_GE1_final(:,3,i)),squeeze(↵
mesh_GE1_final(:,2,i),'color',[0.5 0.5 0.5])
end
for i=1:nb_pts*2-1
plot3(squeeze(mesh_GE1_final(i,1,:))-squeeze(mesh_GE1_final(i,3,:)),squeeze(↵
mesh_GE1_final(i,2,:),'color',[0.5 0.5 0.5])
hold on
end
for i=1:nb_interp
plot3(squeeze(mesh_GE1_final(:,1,i))-squeeze(mesh_GE1_final(:,3,i)),squeeze(↵
mesh_GE1_final(:,2,i),'color',[0.5 0.5 0.5])
end
xlabel('x','Interpreter','LaTeX','fontsize',20)
ylabel('y','Interpreter','LaTeX','fontsize',20)
zlabel('z','Interpreter','LaTeX','fontsize',20)
axis equal;
axis off;
% az = -90;
% el = 90;
% view(az, el);
print -depsc discretizationGE1

%% Outputting the data
%Output in .dat file for PANAIR

outFname = sprintf('panair5.inp'); %output file name
fid = fopen(outFname,'w');

fprintf(fid,'%title\n');
fprintf(fid,'%GE1config\n');
fprintf(fid,'%Wing\n');
fprintf(fid,'%solution\n');
fprintf(fid,'%symmetry - xz plane of symmetry\n');
fprintf(fid,'%misymm mjsymm\n');
fprintf(fid,'%1. 0.\n');
fprintf(fid,'%mach number\n');
fprintf(fid,'%amach\n');
fprintf(fid,'%0.0529\n');
fprintf(fid,'%cases - no. of solutions\n');
fprintf(fid,'%nacase\n');
fprintf(fid,'%1.\n');
fprintf(fid,'%angles-of-attack\n');
fprintf(fid,'%alpc\n');
fprintf(fid,'%0.\n');
fprintf(fid,'%alpha(1) alpha(2) alpha(3) alpha(4)\n');
fprintf(fid,'%2.\n');
fprintf(fid,'%printout options\n');
fprintf(fid,'%isings igeomp isingp icontp ibconp iedgep\n');
fprintf(fid,'%0. 0. 0. 0. 0.\n');
fprintf(fid,'%ipraic nexdgn ioutpr ifmcpr\n');
fprintf(fid,'%0. 0. 1. 0. 0.\n');
fprintf(fid,'%references for accumulated forces and moments\n');
fprintf(fid,'%xref yref zref nref\n');

```

```

fprintf(fid, '0.          0.          0.          0.\n');
fprintf(fid, '=sref      bref      cref      dref\n');
fprintf(fid, '.84282      .98          .8671      .98\n');
fprintf(fid, '$points - wing with composite panels\n');
fprintf(fid, '=kn\n');
fprintf(fid, '1.\n');
fprintf(fid, '=kt\n');
fprintf(fid, '1.\n');
fprintf(fid, '=nm          nn ←
netname\n');
fprintf(fid, '%i.          %i. ←
wing\n', nb_pts*2-1, ←
nb_interp);
fprintf(fid, '=x(1,1)    y(1,1)    z(1,1)    x(*,*)    y(*,*)    z(*,*)\n');
for i=1:nb_interp
    for j=2:2*(nb_pts)-1
        fprintf(fid, '%9.4f %9.4f %9.4f', mesh_GE1_final(j-1,1,i), mesh_GE1_final(j-1,3,i), mesh_GE1_final(j-1,2,i));
        fprintf(fid, ' %9.4f %9.4f %9.4f \n', mesh_GE1_final(j,1,i), mesh_GE1_final(j,3,i), mesh_GE1_final(j,2,i));
    end
    fprintf(fid, '%9.4f %9.4f %9.4f', mesh_GE1_final(2*(nb_pts)-1,1,i), ←
mesh_GE1_final(2*(nb_pts)-1,3,i), mesh_GE1_final(2*(nb_pts)-1,2,i));
fprintf(fid, '\n');
end

fprintf(fid, '$trailing wakes from wings\n');
fprintf(fid, '=kn\n');
fprintf(fid, '1.\n');
fprintf(fid, '=kt\n');
fprintf(fid, '18.\n');
fprintf(fid, '=inat      insd      xwake      twake ←
netname\n');
fprintf(fid, 'wing      1.          3.          .0 ←
wingwk\n');
fprintf(fid, '$eat - liberalized abutments\n');
fprintf(fid, '=epsgeo  igeois      igeout      nwxref      triint      iabsum\n');
fprintf(fid, '0.000001  0.          0.          0.          0.          1.\n');
fprintf(fid, '$end of a502 inputs\n');
fclose(fid);

%Output in .dat file for ICEM

fid = fopen('FullGeom/GEplus.dat', 'w');
fprintf(fid, '%9.d %9.d\n', nb_pts, nb_interp*2);
for i=1:nb_interp
    for j=flip(1:nb_pts)
        fprintf(fid, '%9.4f %9.4f %9.4f\n', mesh_GE1_final(j,1,i), mesh_GE1_final(j,3,i), ←
mesh_GE1_final(j,2,i));
    end
    for j=nb_pts:nb_pts*2-1
        fprintf(fid, '%9.4f %9.4f %9.4f\n', mesh_GE1_final(j,1,i), mesh_GE1_final(j,3,i), ←
mesh_GE1_final(j,2,i));
    end
end
end

```